CONTROLLER DESIGN OF THE GYROSTABILIZER THAT IS USED IN BOATS

A Thesis Submitted to
the Graduate School of
İzmir Institute of Technology
in Partial Fulfillment of the Requirements
for the Degree of

MASTER OF SCIENCE

in Mechanical Engineering

by

Muhammed Rıza BOZELLİ

July 2024
İZMİR

We approve the thesis of **Muhammed Rıza BOZELLİ**

Examining Committee Members:

_____

Prof. Dr. Mehmet İsmet Can DEDE
Mechanical Engineering, İzmir Institute of Technology

_____

Prof. Dr. Serhan ÖZDEMİR
Mechanical Engineering, İzmir Institute of Technology

_____

Assoc. Prof. Dr. Evren SAMUR
Mechanical Engineering, Boğaziçi University

2 July 2024

_____

Prof. Dr. Mehmet İsmet Can DEDE
Supervisor, Mechanical Engineering
İzmir Institute of Technology

_____

Prof. Dr. Mehmet İsmet Can DEDE
Head of the Department of Mechanical Engineering

_____

Prof. Dr. Mehtap EANES
Dean of the Graduate School

ACKNOWLEDGMENTS

I am immensely grateful to all those who have contributed to the completion of this project. First and foremost, I would like to thank my supervisor, Prof. Dr. Mehmet İsmet Can DEDE, for his continuous support, guidance, and constructive feedback.

I would also like to express my gratitude to my colleague, Berk KURT for their teamwork and dedication, which were crucial to the project's success. I owe a debt of gratitude to Mr. Tolga CANKURT and Assoc. Prof. Evren SAMUR, for their collaboration and resources.

On a personal note, I would like to thank my parents, my siblings Semiha and Fethiye BOZELLİ and friends for their unwavering support and understanding during the demanding periods of this project.

Lastly, I am thankful to the HKTM Organization for providing the necessary funding and resources to make this project possible. This work is supported in part by the Scientific and Technological Research Council of Türkiye via grant number 3220962.

Thank you all for your contributions and support.

ABSTRACT

CONTROLLER DESIGN OF THE GYROSTABILIZER THAT IS USED IN BOATS

This thesis presents the development of control structures for gyrostabilizer systems, which are used to dampen unwanted roll motion in sea vessels. Two distinct types of controllers have been studied and compared: (1) the conventional control method, which utilizes the speed and position information of the vessel, and (2) the full feedback controllers, which yield optimal results.

A scaled-down gyrostabilizer has been designed for the purpose of testing the designed control studies. The prototype system is designed to model the single degree of freedom roll motion of the ship. The electric motor added to the system enables the modelling and application of the sea state as a disturbance effect. This disturbing effect is attempted to be eliminated by using the gyrostabilizer on the ship model.

Prior to the design of the control system, kinematic and dynamic calculations of the system were performed analytically. These analytical solutions were verified by comparing them with the simulation file. In the open forms of analytical solutions, the relationships between the gyroscope and the ship are clearly observed. Since the effect of the nonlinear terms in the analytical solutions was found to be small, the equations were simplified and linear control systems were designed.

After mathematical calculations and 3D design, the production of the prototype system was completed. The designed position-velocity (PV-PI) control system and linear quadratic regulator (LQR) based control systems were tested on this prototype system. The results of the tests indicate that, although there is no clear superiority of the two control systems over each other, the fact that the LQR control system has fewer parameters suggests that it can be more easily applied to other ship-gyro combinations.

ÖZET

DENİZ ARAÇLARINDA KULLANILAN JİROSKOPİK SÖNÜMLEYİCİLER İÇİN KONTROLCÜ TASARIMI

Bu tez, deniz taşıtlarında istenmeyen yalpa hareketini sönümlemek için kullanılan jiroskopik sönümleyici sistemleri için kontrol yapılarının geliştirilmesini sunmaktadır. İki farklı kontrolör tipi incelenmiş ve karşılaştırılmıştır: (1) geminin hız ve konum bilgilerini kullanan geleneksel kontrol yöntemi ve (2) en iyi sonuçları veren tam geri beslemeli kontrolörler.

Tasarlanan kontrol çalışmalarını test etmek amacıyla küçültülmüş bir jiroskopik sönümleyici tasarlanmıştır. Prototip sistem geminin tek serbestlik dereceli yalpa hareketini modelleyecek şekilde tasarlanmıştır. Sisteme eklenen elektrik motoru, deniz durumunun bir bozucu etki olarak modellenmesini ve uygulanmasını sağlamaktadır. Bu bozucu etki gemi modeli üzerinde jiroskopik sönümleyici kullanılarak giderilmeye çalışılmıştır.

Kontrol sisteminin tasarımından önce sistemin kinematik ve dinamik hesaplamaları analitik olarak yapılmıştır. Bu analitik çözümler simülasyon dosyası ile karşılaştırılarak doğrulanmıştır. Analitik çözümlerin açık formlarında jiroskop ve gemi arasındaki ilişkiler net bir şekilde gözlemlenmektedir. Analitik çözümlerde doğrusal olmayan terimlerin etkisi küçük bulunduğundan denklemler basitleştirilerek doğrusal kontrol sistemleri tasarlanmıştır.

Matematiksel hesaplamalar ve 3 boyutlu tasarımın ardından prototip sistemin üretimi tamamlanmıştır. Tasarlanan konum-hız (PV-PI) kontrol sistemi ve doğrusal karesel regülatör (LQR) tabanlı kontrol sistemleri bu prototip sistem üzerinde test edilmiştir. Testlerin sonuçları, iki kontrol sisteminin birbirlerine karşı net bir üstünlüğü olmamasına rağmen, LQR kontrol sisteminin daha az parametreye sahip olması, diğer gemi-jiroskop kombinasyonlarına daha kolay uygulanabileceğini göstermektedir.

I dedicate this thesis to my dear parents, Yüksel and Sinan BOZELLİ

TABLE OF CONTENTS

LIST OF FIGURES

Figure **Page**

Figure **Page**

Figure **Page**

LIST OF TABLES

Table **Page**

CHAPTER 1

INTRODUCTION

Motion sickness is a common occurrence in any kind of transport vehicles especially in marine transport vehicles. The wave or wind-induced disturbance causes the sea vessel to oscillate with a specific period and magnitude range. These disturbing effects to which people are exposed adversely affect their physiology (Cha et all., 2021). A study on motion sickness was carried with using 20 male subjects. The results shows that 0.2 [Hz] vibrations should be avoided while human body can tolerate the vibrations between 0.5-1 [Hz] (O'Hanlon, James, and Michael, 1973). The shock vibration intensity to which the human body can be exposed is internationally limited by standards such as International Organization for Standardization (ISO) 2361. With an adaptation of this document, it has been reorganized by International Maritime Organization (IMO) for maritime applications. Ship stabilization systems are aims to damp the undesired motion of the sea vessels in order to reduce the motion sickness. In addition to that, also they help to improve the fuel efficiency.

1.1. Background on Ship Stabilization Systems

The development of anti-damping technologies starts with William Froude towards the end of the 1800s. William laid the foundations of tank type stabilization technology. In first stages of the anti-roll tanks the natural physics laws are commonly used. In this system there are two reservoirs on both side of the ship as seen in the Figure 1.1 (Kula, 2015). These reservoirs are connected to each other by tubes. The condition where the flow is not controlled called as passive anti-roll systems. The controlled passive anti roll tanks contain a valve that controls the flow rate of the water during the operation. Finally, the active anti-roll tanks contain a water pump that creates forced water movements between tanks (Peres, Tristan, and Mogens, 2012).

The anti-rolling tanks do not impair the integrity of the ship's hull. Therefore, they have no negative impact on hydrodynamic properties of the ship hence they do not affect the fuel efficiency directly. As a positive contribution to the roll damping, the anti-rolling

tanks can operate at zero speed conditions. However, they consume lots of space in the ship and its existence creates additional weight on the ship. Considering these effects, they have indirectly negative effect on the emissions of the ship. However, they can generate high amount anti-rolling torque than the other anti-rolling systems. For that reasons, the anti-rolling tanks are frequently used for larger ships (Kula, 2015).

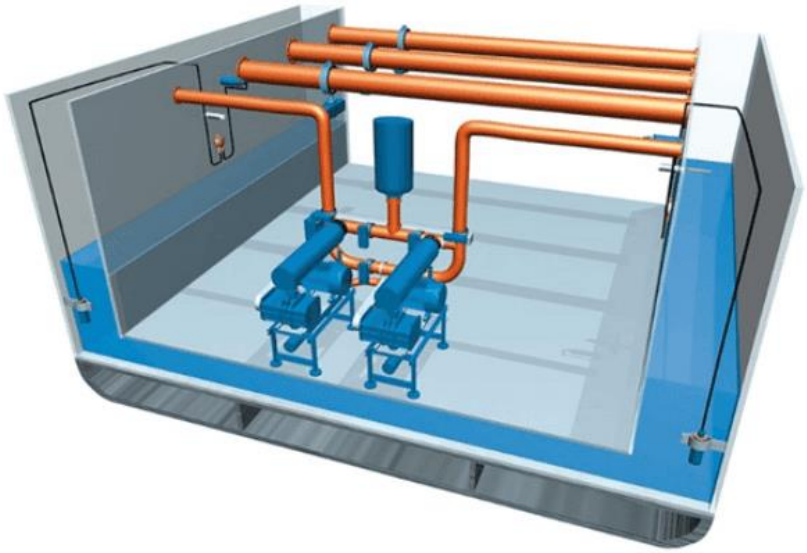

Figure 1.1. 3D CAD design of active anti-rolling tanks (Source: Sinha, 2022)

The most popular member of the ship stabilization system is the fin type stabilization system. They basically use the similar principle of airfoils on aircraft. The flowing fluid creates high- and low-pressure zones around the fin. The pressure difference creates a reaction force perpendicular to the surface of the airfoil. By controlling the angle of attack of the airfoil, the generated force can be controlled (Fan et all., 2019). Therefore, roll damping can be achieved by simply designing a feedback control system that changes the angle of attack in relation to the ship's roll angle.

The fin system stabilization system contains at least two fins that placed the hull section of the ship as seen in the Figure 1.2. They placed symmetrically to each other for high controllability. Fins require the pressure difference between the surfaces to create an anti-rolling moment (DiFrangia, 2016). That can be achieved by the shape of the foil with the help of the fluid flow. Hence, there is not exist a damping at zero speed conditions unlike anti-rolling tanks. This is an unfavorable property for the fin type stabilization systems (Fan et all., 2009). In addition to this disadvantage, fin-type systems damage the integrity of the ship's hull and create friction against the direction of movement. However,

they can generate high amount of anti-rolling moment although they have relatively lower mass and space requirement than the anti-rolling tanks. The properties such as low mass, low volume high anti-rolling moments are desirable feature for the large ship used in international transport (Kula, 2015).

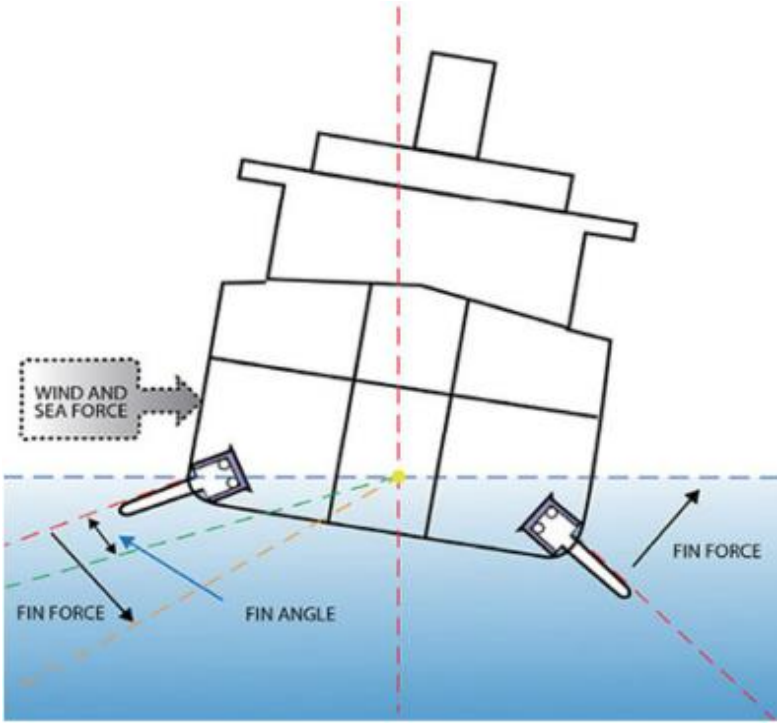

Figure 1.2. 2D Schematic of a fin stabilization system (Source: DiFrangia, 2016)

Another commonly used roll stabilization system is called a bilge keel. At first glance they look very similar to fin stabilizers. This is because they are in a kind of fixed plate on the hull of the ship as seen in the Figure 1.3. The difference between a bilge keel and a fin is that a bilge keel resists the rolling motion by increasing the area in the direction of roll. The increased area creates a drag force that resists the rolling motion. This improves the ship's stability. Their initial cost is relatively lower than the others and they have no moving parts.

However, in the event of a failure, their maintenance costs can be high due to the dry-docking (pulling the ship to the ground) operations. They can operate both zero speed and in motion. They generate a drag resistance on the ship similarly fin type stabilization systems (Sinha, 2022).

Last but not least, there are gyrostabilizers that damps the roll motion of the ships. The gyrostabilizer uses the conservation of the angular momentum in order to generate

an anti-rolling moment. In basically, it contains a large mass of cylindrical object that has high mass moment of inertia about its spin axis as seen in the Figure 1.4. The combination of angular speed and the mass moment of inertia generates angular momentum of the gyrostabilizer system (Peres, Tristan, and Mogens, 2012). Thanks to physics law, the angular momentum tends to protect its orientation. Consider a system in the Cartesian system and let the system have an angular momentum in the z direction. Forcing this system to rotate in the x direction will cause a reaction force in the y direction as a result of the law of conservation of angular momentum. They can operate in zero speed condition. Although they occupy mass and volume in the ship, the counter damping moment mass ratio is higher than that of the tank type (Kula, 2015). They do not impair the integrity of the ship's hull and therefore do not have a bad effect on hydrodynamics. In order to produce a high damping moment, they must rotate at very high speeds or have a very large mass moment of inertia. Since this is not technologically and sustainably feasible, it is mostly preferred for small boats and yachts (Giallanza, Antonio, and Tony, 2019).

Figure 1.3. Bilge Keel on a Ship (Source: Sinha, 2022)

In conclusion, the available technologies for stabilizing sea vessels are presented. These technologies employ diverse physical methodologies to mitigate the motion of the vessel. They exhibit certain advantages and disadvantages relative to one another. The respective advantages and disadvantages are enumerated in Table 1.1.

Figure 1.4. A commercial gyrostabilizer product advertisement that shows the direction of motions and generated forces (Source: Williams, 2023)

Table 1.1. Sea vessel stabilization technologies comparison

Technology	Pros	Cons
Anti Rolling Tanks	• Hull integrity • Zero speed operation • Moderate anti rolling torque	• Take a big space inside of the ship • High investment
Active Fins	• Take a moderately small space • High anti rolling torque	• Poor Hull integrity • Not operate at zero speed • High maintenance cost
Bilge Keel	• No space inside the ship • No moving parts	• Not operate at zero speed • Low anti rolling torque • High maintenance cost
Gyrostabilizer	• Hull integrity • Zero speed operation • Low maintenance cost	• Take a big space inside of the ship • Moderate anti rolling torque

1.2. Thesis Objective and Motivation

The aim of this thesis is to develop a control system strategy for a gyrostabilizer. The design of the control system and the gyrostabilizer should compensate for the undesired rolling motion of the vessel. Marine vessels can vary in size and shape. Some of the variables that characterize the vehicle can be determined, while others cannot. Designed control system should easily use for combination of ship and gyrostabilizer. Also, it should provide high performance. The performance of the gyrostabilizer in this

thesis is defined as the total power of the damped roll motion divided by total power of the undamped roll motion. This ratio should be below the 0.15 for a successful gyrostabilizer control system. Power of the roll motion can be calculated by finding the area under the Fourier transform of the rolling motion signal of the ship.

1.3. Main Contributions

This thesis contributes to the existing literature by conducting dynamic studies on gyrostabilizer and ship systems, as well as by comparing various control algorithms. These analyses offer valuable insights into system performance and aid in identifying optimal control strategies for enhancing stability and efficiency.

1.4. Thesis Outline

This thesis consists of seven chapters. In this chapter the purpose, aim and motivation of the thesis are stated. In the second chapter the literature review on ship dynamics, sea states, gyrostabilizer types and gyrostabilizer control strategies are carried out. In the third chapter, the kinematic and dynamic analyses of the thesis are discussed by introducing the scaled down gyrostabilizer. In the fourth chapter, the control system of the gyrostabilizer is given by explaining the sensory feedback system. Then, in chapter five, system identification tests are carried out to compare the parameters of the design and real prototypes. Next, the experimental results of the gyrostabilizer test system are presented in chapter six. Finally, the overall study is concluded in chapter seven.

CHAPTER 2

LITERATURE SURVEY

This section presents a review of the equations of motion and physical parameters in the literature for modelling the motion of ships. It is important to understand ship motions in order to determine the structure of the test rig to be installed. Then, sea state models are analyzed to obtain the disturbance effects on the ships. The outputs obtained from these models will be used to simulate the wave disturbing effects on the test rig. Finally, the types, control systems and dynamic models of gyrostabilizers available in the literature are examined.

2.1.Brief Introduction about Sea Vessels

Ships are one of mankind's oldest means of transport. Although the ships used or produced today are different from their ancestors, they are basically vehicles that use the buoyancy of water. As the field of marine engineering has improved, so has the technology of ships, and a certain culture and terminology has developed. It is important to understand the terminology of maritime engineering before delving into the dynamics of ships.

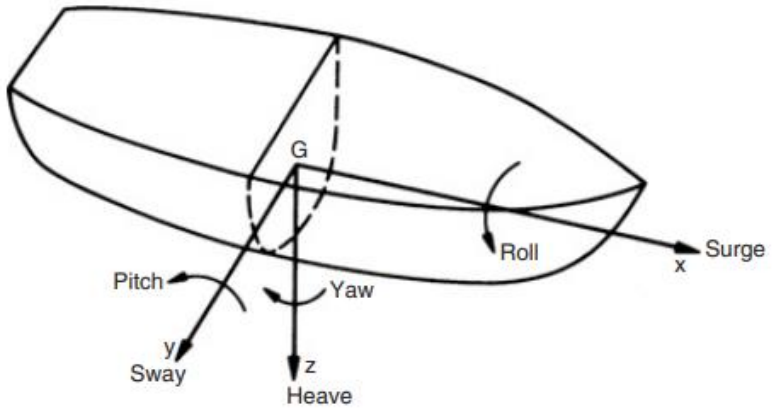

Figure 2.1. Ship coordinate system (Source: Molland, 2009)

In general, marine vessels have 6 degrees of freedom (DoF) in water as seen in the Figure 2.1. In all of those axes a ship can translate and rotate. The translation motions

about x, y and z axes are ca lled as Surge, Sway and Heave motions respectively. Similarly, the rotational motions about x, y and z axes are called as Roll, Pitch and Yaw motions respectively. It is possible to describe a 6-DoF equation of model for a ship as described in Equation 2.1. (Berghal, 2009)

$$\widehat{M}_s\ddot{\bar{\eta}} = \bar{F} \tag{2.1}$$

In given Equation 2.1 M_s is 6 by 6 mass matrix, $\bar{\eta}$ is a vector of position in the 6-DoF as $\bar{\eta} = (\eta_1, \eta_2, \eta_3, \eta_4, \eta_5, \eta_6)^T$ and finally $\bar{F}$ represents the vector of forces and moments acting on the body as $\bar{F} = (F_1, F_2, F_3, M_1, M_2, M_3)^T$. The subscript on both vector of position, force and moments represent the one the motion direction of the ship. The position (η_i) represents the respective motion in direction of $i = 1,2,3,4,5,6$; surge, sway, heave, roll, pitch and yaw respectively. The force (F_i) and moment (M_i) represent the acting axis for $i = 1,2,3$; surge, sway, heave. By differentiation of the position vector two times the acceleration vector $(\ddot{\bar{\eta}})$ is obtained.

The mass matrix (M_s) usually have a structure as in Equation 2.2.

$$\widehat{M}_s = \begin{bmatrix} m & 0 & 0 & 0 & mz_G & 0 \\ 0 & m & 0 & -mz_G & 0 & 0 \\ 0 & 0 & m & 0 & 0 & 0 \\ 0 & -mz_G & 0 & I_{44} & 0 & -D_{46} \\ mz_G & 0 & 0 & 0 & I_{55} & 0 \\ 0 & 0 & 0 & -D_{46} & 0 & I_{66} \end{bmatrix} \tag{2.2}$$

In the mass matrix representation m is the mass of the ship, z_g is the vertical component of the ship mass center. The moment of inertia terms about x, y and z axes are represented as I_{44}, I_{55} and I_{66} respectively. Finally, D_{46} and D_{64} shows the off-diagonal elements of the mass moment of inertia. These parameters are significantly small with respect to symmetric mass distribution of the vessel.

The force vector $\bar{F}$ are consist of three parameters as (1) wave-exited forces (τ_ω), (2) hydrodynamic reaction forces (τ_r) and (3) reaction forces from the mooring system (τ_{rs}). If the ship is not tied to the shore at any point, this term becomes zero $(\tau_{rs} = 0)$. The wave-exited forces depend on the sea conditions. The remaining hydrodynamic reaction forces can be written as a function of the position vector of the ship.

$$\overline{\mathrm{T_r}} = -\hat{A}_s\ddot{\bar{\eta}} - \hat{B}_s\dot{\bar{\eta}} - \hat{C}_s\bar{\eta} \tag{2.3}$$

In the Equation 2.3, A_s is the added mass (hydrodynamic mass), B_s is the hydrodynamic damping and finally C_s is the hydrostatic stiffness (hydrodynamic restoring). In these A_s, B_s and C_s matrices represent the characteristics of the sea vessel with 6x6 matrices as described in Equation 2.4, 2.5 and 2.6.

$$\hat{A}_s = \begin{bmatrix} A_{11} & 0 & 0 & 0 & A_{15} & 0 \\ 0 & A_{22} & 0 & A_{24} & 0 & 0 \\ 0 & 0 & A_{33} & 0 & 0 & 0 \\ 0 & A_{42} & 0 & A_{44} & 0 & 0 \\ A_{51} & 0 & 0 & 0 & A_{55} & 0 \\ 0 & 0 & 0 & 0 & 0 & A_{66} \end{bmatrix} \tag{2.4}$$

$$\hat{B}_s = \begin{bmatrix} B_{11} & 0 & 0 & 0 & B_{15} & 0 \\ 0 & B_{22} & 0 & B_{24} & 0 & 0 \\ 0 & 0 & B_{33} & 0 & 0 & 0 \\ 0 & B_{42} & 0 & B_{44} & 0 & 0 \\ B_{51} & 0 & 0 & 0 & B_{55} & 0 \\ 0 & 0 & 0 & 0 & 0 & B_{66} \end{bmatrix} \tag{2.5}$$

$$\hat{C}_s = \begin{bmatrix} 0 & 0 & 0 & 0 & 0 & 0 \\ 0 & 0 & 0 & 0 & 0 & 0 \\ 0 & 0 & C_{33} & 0 & C_{53} & 0 \\ 0 & 0 & 0 & C_{44} & 0 & 0 \\ 0 & 0 & C_{53} & 0 & C_{55} & 0 \\ 0 & 0 & 0 & 0 & 0 & 0 \end{bmatrix} \tag{2.6}$$

In given mathematical expressions for A_{ij}, B_{ij} and C_{ij} have form of hydrodynamic reactions i that caused by motion in direction j. Finally, the 6-DoF linear Equation of motion of the ship can be described as given in Equation 2.7.

$$\overline{\tau_\omega} = \left(\hat{M}_s + \hat{A}_s\right)\ddot{\bar{\eta}} + \hat{B}_s\dot{\bar{\eta}} + \hat{C}_s\bar{\eta} \tag{2.7}$$

Although the 6-DoF model of a ship may be useful for different kind of applications it may too complex for roll stabilization systems. Marine vessels have a narrow structure along the direction of travel to reduce the hydraulic friction at the keel part of the vessel. Although this structure effectively increases the performance of the

vessel, it makes it more sensitive to rolling motion. The rolling motion is a crucial problem in the design of a ship because it determines the stability characteristics of a ship (Kornev, 2012). For those reasons some policy makers such as International Maritime Organization (IMO), defines for Intact Stability for the different kind of ships.

The acting forces on a ship should be well addressed in order to establish a mathematical model for rolling motion of a ship. Two types of forces act on the ship in static equilibrium position: (1) inertial forces and (2) buoyancy forces. For static equilibrium these two forces have to be equal to each other. The ship as a mass by the structure itself. The gravitational acceleration causes a force that acts on center of gravity (G) on downward direction. In turn, the submerged volume of the vessel generates an upward buoyancy force that acts on buoyancy center (B).

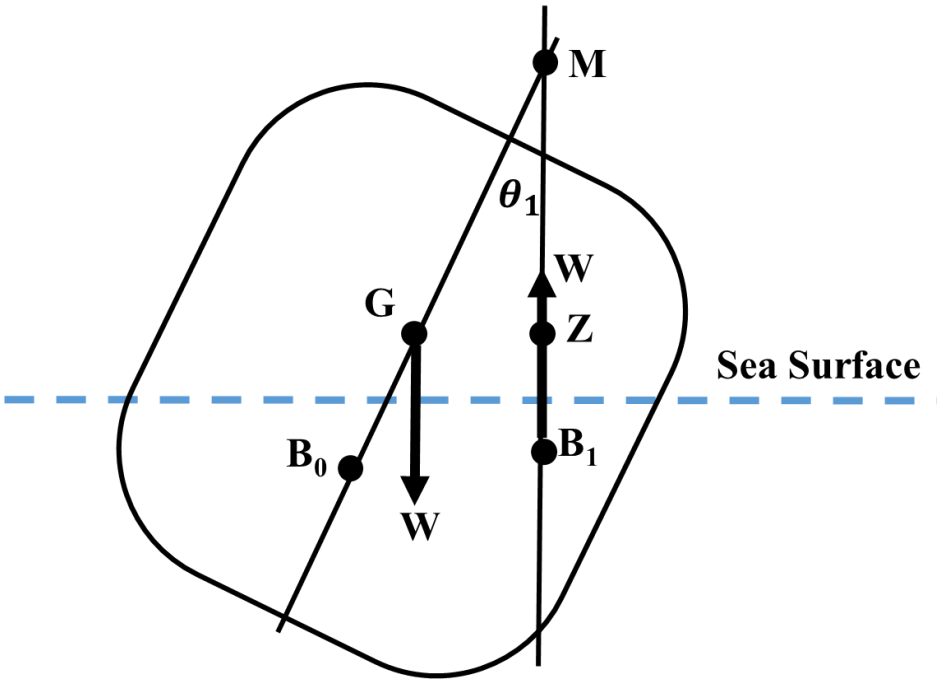

Figure 2.2. Free body diagram of ship rolling motion

Figure 2.2 shows this free body diagram of the ship's rolling motion. In the figure the ship is represented by a black box. The center of gravity (G) and the center of buoyancy (B_0, B_1) are shown in the figure. The center of buoyancy varies with the roll angle (θ_1) of the ship, while the center of mass changes by adding or removing weight. The other two parameters, metacenter and z-point, are shown in Figure 2.3. Metacenter is an imaginary point used to describe the stability of the ship. The metacenter is the intersection of two lines passing through the center of gravity and the center of buoyancy.

The line passing through the center of gravity is drawn parallel to the symmetry axes of the boat, while the other line passing through the center of buoyancy is drawn parallel to the gravity vector. Finally, Z is an imaginary point located on the MB_1 line. The distance between GZ (righting arm) and the buoyancy force generates the righting moment about the center of gravity.

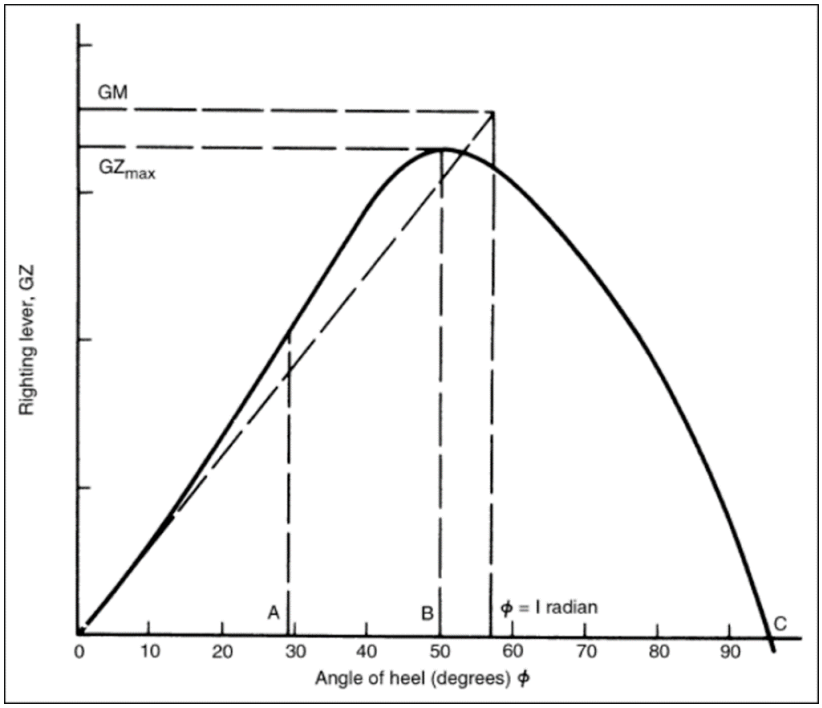

Figure 2.3. Static stability curve / GZ curve of a ship (Chakraborty, 2022)

Figure 2.3 shows the static stability curve of a vessel. The x-axis indicates the roll angle (heel angle $\phi = \theta_1$) while the y-axis indicates the righting lever or the distance between the GZ points. The righting lever is a non-linear property of the ship. However, there are some areas where the righting lever shows linear characteristics up to 10 degrees. It increases up to 50 degrees and then suddenly decreases as the roll angle increases. This is significant when considering the capsizing of vessels. After some roll angles, the system cannot generate enough righting moment to recover the ship and the ship overturns. The metacentric height (GM) is the distance between metacenter and center of gravity of the ship. It is a powerful tool for describing the stability of the ship. By investigating the geometry generated by G-Z-M point as seen in Figure 2.2, the Equation 2.8 can be written (Ibrahim and Grace, 2010).

$$GMsin(\theta_1) = GZ \tag{2.8}$$

By considering the small angle approximations $\sin(\theta_1) \approx \theta_1$ is the righting arm can be expressed as a function of roll angle. By considering the buoyancy force is equal to the weight of the ship the righting moment (heeling moment) can be expressed as a function of roll angle (Ibrahim and Grace, 2010):

$$M_R = g\rho\nabla GM\theta_1 \tag{2.9}$$

In the given Equation 2.9 g is the gravity constant $[m/s^2]$, ρ is the density of water $[kg/m^3]$, ∇ is the displacement of the ship $[m^3]$ and M_R is the righting moment of the ship $[Nm]$. However, given simple Equation 2.9 is valid for small angles such as lower than 10 degrees. For more comprehensive mathematical models, the GZ curve must be defined using various functions.

The dynamic relationship of the ship roll motion depends on the mass moment of inertia, damping and restoring terms as described in 6-DoF model. The equation of motion for only rolling motion of a vessel can be expressed as functions of roll angle and roll rate of vessel as given Equation 2.10 (Taylan, 2000).

$$(I_{44} + A_{44})\ddot{\theta_1} + B_{444}(\dot{\theta_1}) + gmGZ(\theta_1) = \tau_\omega \tag{2.10}$$

In given Equation 2.10, the acceleration of the roll angle depends on the mass moment of inertia about roll motion (I_{44}) and the added mass (A_{44}), the damping effect is given by a function defined by th the roll rate, finally the righting moment is defined as a function of the roll angle. The damping function can be defined as a combination of linear (B_L) and nonlinear terms (B_N).

$$B_{44}(\dot{\theta_1}) = B_L\dot{\theta_1} + B_N\dot{\theta_1}^3 \tag{2.11}$$

The righting arm curve $GZ(\theta_1)$ can be expressed by as formulating the static stability curve as a quintic function.

$$GZ(\theta_1) = C_1\theta_1 + C_3\theta_1^3 + C_5\theta_1^5 \tag{2.12}$$

The constants of righting arm can be determined from static stability curve with using the angle of vanishing stability (θ_v) and the area under the curve $\left(A_{\theta_v}\right)$. Obviously the polynomial fitting tools can be used for determination of constants C_1, C_3 and C_5.

$$C_1 = \frac{d(GZ)}{d\theta_1} = GM \tag{2.13}$$

$$C_3 = \frac{4}{\theta_v^4}(3A_{\theta v} - GM\theta_v^2) \tag{2.14}$$

$$C_5 = -\frac{3}{\theta_v^6}(4A_{\theta v} - GM\theta_v^2) \tag{2.15}$$

The Equation 2.10 can be further simplified for the simulation purposes for small roll motions of the vessel as described in Equation 2.16 (Towndsend and Ajit, 2014).

$$\tau_\omega = (I_{44} + A_{44})\ddot{\theta} + B_{44}\dot{\theta} + C_{44}\theta \tag{2.16}$$

In cases where the ship parameters are not known exactly, the parameters used in the equation can be estimated by using the size and weight information of the ship. According to Towndsend and Ajit (2014), mass moment of inertia about the roll axis (I_{44}) can be calculated by using the beam of the vessel (L_{BM}). Beam of a vessel is distance between the port side to the starboard side. In simpler terms, it's the width of the ship.

$$I_{44} = m(0.4\ L_{BM})^2 \tag{2.17}$$

The added mass (A_{44}) assumed as 30% of the mass moment of inertia (Towndsend and Ajit, 2014).

$$A_{44} = 0.3\ I_{44} \tag{2.18}$$

If the undamped natural roll frequency (ω_{44}) is known, the restoring coefficient (C_{44}) can be written with using the terms for added mass and mass moment of inertia

terms. Otherwise as described above, the restoring coefficient is equal to the weight multiplied by the metacentric height of the vessel.

$$C_{44} = \omega_{44}^2 (I_{44} + A_{44}) \tag{2.19}$$

$$C_{44} = mgGM \tag{2.20}$$

Finally, the roll damping term (B_{44}) can be defined by using a damping ratio (β_d) which is generally around 0.1.

$$B_{44} = 2\beta_d \sqrt{C_{44}(I_{44} + A_{44})} \tag{2.21}$$

Other methodologies, such as computational fluid dynamics analyses, are also available to describe ship motions. However, within the scope of this thesis, the studies in this section are not included and the studies are continued using the mathematical models obtained. In order to determine the ship disturbance effect mentioned in this chapter, the sea and waves are investigated in the next chapter.

2.2.The Sea State Models

The marine environment provides harsh condition for marine vessels and structures. It is too complicated to fully understand and model of the waves. Tidal waves, earthquakes, winds, currents are main responsible of creating waves. However, the occurrence probability and effect of these wave types are different form each other. For instance, the earthquakes can be generated over 10-meter height waves but its frequency of occurrence it too low. On the other hand, tidal is can be seen in two times in a day (Molland, 2011).

In the following Figure 2.4 shows graphically wave types, their arbitrary energy scale and their frequencies. As seen in the figure, the frequency of the wind-generated waves is higher than the other types of waves. Also, Wind Sea Waves has the highest energy scale than the others. For that reason, several wave models are designed such as SWAN wave model that used for short-crested wind-generated waves in coastal regions.

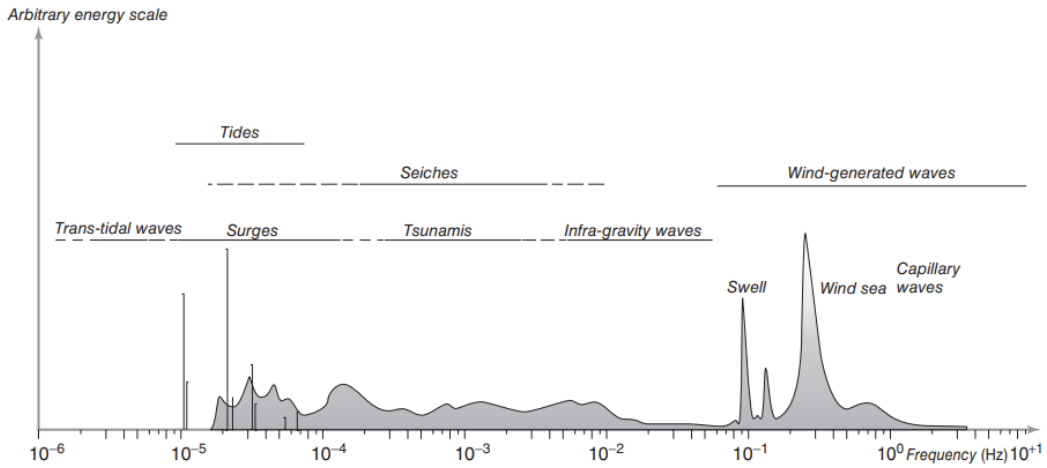

Figure 2.4. Frequency of ocean waves (Source: Toffoli, Alessandro, and Elzbieta, 2017)

Although the waves composed of different types, it is possible to describe it with using simple terms such as significant height (H_s) and mean period of all sine components (T_1). The significant wave height is the average height of the largest waves while the mean period of all sine components is an average value of the sine waves. These parameters define the sea states as seen in the following Table 2.1.

Table 2.1. Sea states and wave properties (Liu et all., 2018)

Sea States	$T\ [s]$	$H_s[m]$
1	2.0	0.09
2	4.8	0.67
3	6.5	1.40
4	8.1	2.44
5	9.7	3.66
6	11.3	5.49
7	13.6	9.14
8	17.0	15.24

The ocean pattern has been thoroughly researched by oceanographers. In essence, they entered measurements into general equations. The most commonly used wave spectrums in marine field are (1) The Pierson Moskowitz (PM) wave spectra and (2) the Joint North Sea Wave Program (JONSWAP) wave spectra (Molland, 2011). PM was introduced at 1963 for fully developed sea above the 19.5-meter height above the sea

surface. The PM wave spectra is also called as Bretschneider spectrum. The JONSWAP is an international study that focuses on coastal waters of limited fetch.

Generalized PM $(S(f))$, spectrum in terms of frequency is written as following Equation 2.21 (ITTC, 2002).

$$S(f) = \frac{A}{f^2}\exp\left(-\frac{B}{f^4}\right) \tag{2.21}$$

In given PM spectrum A and B are important constants that defines the characteristics of the wave spectrum. That can be calculated with using different approaches. If one of the sea or wind parameters are exist one-parameter Pierson-Moskowitz spectrum can be derived. That spectrum requires one of the following parameters, (1) velocity of the wind (U), (2) the significant wave height (H_s) or (3) the spectral peak frequency (f_p). If one of them is known using the Equations 2.22 and 2.23, the A and B constants can be determined. The coefficients are defined as $\alpha = 0.0081$ and $\beta = 0.74$ (ITTC, 2002).

$$A = \alpha g^2 (2\pi)^{-4} \tag{2.22}$$

$$B = \beta\left(\frac{2\pi U}{g}\right)^{-4} \quad \text{or} \quad B = \frac{5}{4}f_p^4 \quad \text{or} \quad B = \frac{4\alpha g^2}{(2\pi)^4 H_s^2} \tag{2.23}$$

Two-parameter Pierson-Moskowitz spectrum can be used if the significant wave height and the spectral peak frequency is known. A and B can be calculated as given in Equation 2.24 and 2.25 (ITTC, 2002).

$$A = \frac{5H_s^2 f_p^4}{16} \tag{2.24}$$

$$B = \frac{5}{4}f_p^4 \tag{2.25}$$

ISSC spectrum is also requires two input parameter as significant wave height and mean frequency $(\bar{f})$. In most basic way, ISSC spectrum modifies the Two-parameter

Pierson-Moskowitz spectrum by using the correlation between mean and spectral peak frequencies $f_p = 0.722\bar{f}$. A and B can be found for ISSC spectrum as given in Equation 2.26 and 2.27 (ITTC, 2002).

$$A = 0.1107\, H_s^2 \bar{f}^4 \tag{2.26}$$

$$B = 0.4427\, \bar{f}^4 \tag{2.27}$$

ITTC spectrum can be determined by using mean wave period ($\bar{T}$) and significant wave height in order to determine the A and B variables (ITTC, 2002).

$$K = \frac{\bar{T}}{1.924}\sqrt{\frac{g}{H_s}} \tag{2.28}$$

$$A = \frac{0.0081}{K^4} g^2 \tag{2.29}$$

$$B = \frac{0.0081}{K^4} \frac{4g^2}{H_s^2} \tag{2.30}$$

The JONSWAP spectrum is a little complex then the PM spectrum. In simpler ways, the JONSWAP spectrum uses the PM spectrum by combining them with vessels heading direction (μ) and its speed (U). The JSONSWAP wave spectrum can be found by defining the PM spectrum with $S_{PM}(\omega)$ where $\omega = 2\pi f$ (Towndsend and Shenoi, 2014).

$$S_J(\omega) = 0.658\,(3.3)^J\, S_{PM}(\omega) \frac{g}{(g - 2\omega U\cos(\mu))} \tag{2.31}$$

In Equation 2.32, unknown parameter J can be found as followings. The correction factor is defined as $\gamma = 0.07$ for $\omega < 2\pi/\bar{T}$ or $\gamma = 0.09$ for $\omega > 2\pi/\bar{T}$.

$$J = \exp\left(\left(-\frac{1}{2\gamma^2}\right)\left(\frac{\omega\bar{T}}{2\pi - 1}\right)^2\right) \tag{2.32}$$

After defining the wave spectrum models, finally the roll excitation moment caused by the sea can be determined by combining the wave spectrum and vessels characteristics. The second order roll motion is defined in Equation 2.16. However, given equation have to be converted to frequency domain by simply inserting $\phi(t) = |\phi|e^{i\omega t+\beta}$. The roll velocity and acceleration related term can be found by taking the derivative of the roll angle response. For the condition where (ω) goes to zero the velocity and acceleration related terms becomes relatively small with respect to restoring coefficient term. For that reason, Equation 2.16 can simply be written as in Equation 2.33 (Olmez and Cakici, 2022).

$$C_{44}|\phi|e^{i\omega t+\beta} = |\tau_\omega|e^{i\omega t+\beta} \tag{2.33}$$

In order to find a relationship between wave and excitation moment it is assumed that ship roll motion follows the wave amplitude. Therefore, there is a direct relationship between the roll motion and the slope of the wave. Using any kind of wave spectral energy distribution function $\left(S_{\beta\zeta}(\omega)\right)$ the wave roll excitation distribution spectrum $\left(S_{F_{40}}(\omega)\right)$ can be obtained as in Equation 2.34.

$$S_{F_{40}}(\omega) = |F_{ext}(\omega)|^2 S_{\beta\zeta}(\omega) \tag{2.34}$$

The excitation moment spectrum in the Equation 2.34 can further simplified by using the Equation 2.33 with using the characteristic properties of the vessel.

$$S_{F_{40}}(\omega) = (gmGM_t\omega^2)^2 S_{\beta\zeta}(\omega) \tag{2.35}$$

The wave excitation moment spectrum can be used for initial investigation however it is not useful for simulation purposes. Therefore, following equation can be used for generating time domain signal by superposing the randomly selected frequency ω_n and the phase angle ψ_n for each selected frequency.

$$F_{ext}(t) = F_{40}(t) = \sum_{n=1}^{N\,freq} \sqrt{2\, S_{F_{40}}(\omega_n)\delta\omega}\, \cos(\omega_n t + \psi_n) \qquad (2.36)$$

2.3. Gyrostabilizer Control Strategies

The history of gyroscopic systems dates back to 1743. At that time, an artificial horizon system based on gyroscopes was proposed. However, the maturation of these ideas and the acquisition of patent rights coincide with the end of 1800. At the beginning of the 1900s, gyroscopic systems were used as measuring instruments, and in 1908 they were used as gyrostabilizers. With the acceleration of the space race in the 1960s, they gained another field of study to provide directional control in spacecraft. With the rise of sustainability studies in the 2000s, studies have been carried out in areas such as wave energy power generation (Townsend and Ramanand, 2011).

The gyrostabilizers consist of two main parts: (1) flywheel and (2) gimbal (enclosure). The flywheel has a high moment of inertia about its axis of rotation. This high rotational speed and mass moment of inertia generate an angular momentum about its axis of rotation. Angular momentum of the system can be shown as $L = I \cdot \omega$. The gimbal is a part that can change the direction of the flywheel's angular momentum.

In a more general sense, gyrostabilizers are a type of spinning wheel device. The spinning wheels can generate a force or torque to, for example, change the direction of a satellite or to display the direction (gyrocompass). Gyrostabilizers are a subset of spinning wheel devices. Their purpose is to dampen the unwanted oscillatory motion of anybody. According to Townsend and Ramanand (2011), the spinning wheel have 4 different types in terms of their gimbal actuation strategy and number of gimbal parts. They can have a single or double gimbal. Also, the gimbal can be free to move (passive type) or there can be an actuator that forces the gimbal to move (active type). Assume that these spinning wheels are mounted on a body. Active type spinning wheels can generate force or torques on this body while passive type spinning wheel resists the motion of the body.

The body can have one or more spinning wheels. The multi-wheel type spinning wheel arrangement has advantages such as cancelling the unwanted effect of each other. It is also possible to generate multi-axis control torque with respect to their initial directions. However, they have challenges in terms of control strategies and mechanical perspective.

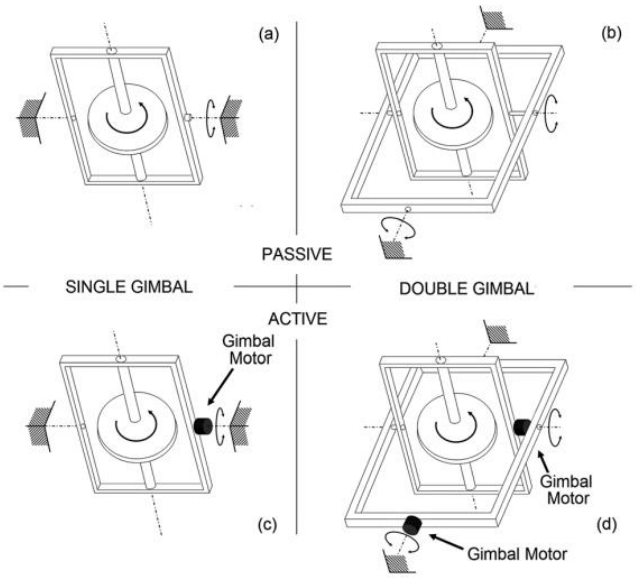

Figure 2.5. Motion types of spinning wheel (Source: Townsend and Ramanand, 2011)

This study focuses on the single-wheel, single-gimbal active spinning wheel gyrostabilizer system for boats. That type of system can be both horizontal and vertical spin axis as seen in the Figure 2.6. As seen in the figures, the part indicated by the blue arrow shows the roll motion of the ship. As the name suggests, the horizontal type gyrostabilizer spinning wheel direction is positioned along the sway direction of the ship. To generate damping torque, the system is rotated along the yaw to the ship axis as shown by the orange arrow.

In the vertical type gyrostabilizer, it is positioned perpendicular to the ship's deck along the direction of heave. Again, as shown in the Figure 2.6. with the orange arrow, the damping torque is generated by rotating the spinning wheel along the pitch axis. These orange-colored arrow motion are called precession motion.

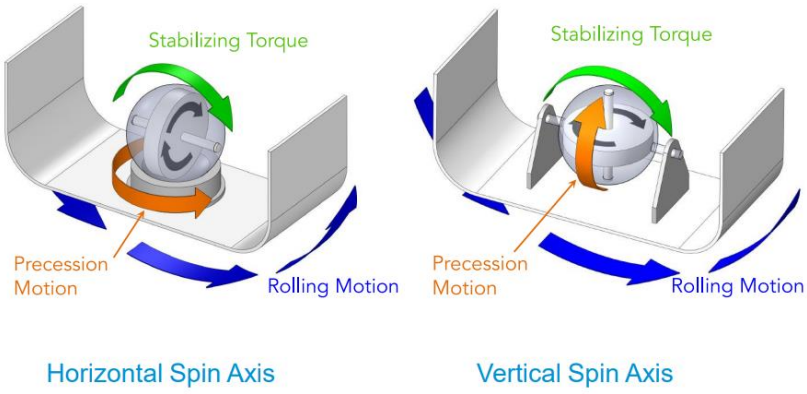

Figure 2.6. Horizontal and Vertical spin axis types of gyrostabilizers (Source: How gyrostabilizers work | Veem Marine, 2015)

Both of the horizontal and vertical spin axis types of the gyrostabilizer can generate stabilizing forces on the ship as seen in the Figure 2.6. However, they have particular differences between each other. The inertial force of the spinning wheel forces two bearings in a radial direction in the horizontal spin axis. On the other hand, it forces one bearing in an axial direction in the vertical spin axis. For this reason, the bearing selection is crucial point in the vertical spin axis type of gyroscopes.

On the other hand, horizontal spin axis type of gyrostabilizers cannot take advantage of the passive (natural) type control (How gyrostabilizers work | Veem Marine, 2015). It has to be driven by some kind of actuator to generate a stabilizing torque. Unlikely, the vertical spin axis type of gyrostabilizer can take advantage of passive control. And also have an equilibrium point for the precession motion, simply by placing the center of mass of the casing below the spin axis. As a result, the spin direction always tends to align with the initial state (How gyrostabilizers work | Veem Marine, 2015). The largest gyrostabilizer manufacturers such as Seakeeper and VEEM Marine use the vertical spin axis type of gyrostabilizer because of these advantages.

Previously, it is mentioned that the vertical spin axis type of has an equilibrium point with respect to position of the center of mass. The importance of that equilibrium point can be expressed as follows. A gyrostabilizer can produce a stabilizing torque unless the direction of spinning wheel and rolling direction is different than each other. In another word, the ship rolls around surge direction, the spinning wheel initially turns around the heave direction and the precession motion occur around the sway direction. The ship rolls direction and the precession motion direction does not change during the operation. However, the spin direction of the gyrostabilizer changes. When enough amount of precession motion occurs the spin direction of gyrostabilizer and rolling direction of ship collapse on each other. This condition is called as “Gimbal Lock”. Also, it is a singularity point for the system. It is a big problem for passive type gyrostabilizer system because the spin direction should be rearranged with using external forces. Perez and Steinman (2009) give the equation of motion of ship and gyrostabilizer as given in Equation 2.37 and 2.38. The singularity problem can be seen by driving these equations.

$$I_{44}\ddot{\theta}_1 + B_{44}\dot{\theta}_1 + C_{44}\theta_1 = \tau_\omega - nK_g\dot{\theta}_2\cos(\theta_2) \tag{2.37}$$

$$I_g\ddot{\theta}_2 + B_g\dot{\theta}_2 + C_g\sin(\theta_2) = K_g\dot{\theta}_1\cos(\theta_2) + \tau_p \tag{2.38}$$

The Equation 2.37 represents the 1-DoF ship dynamics around roll axis and the Equation 2.38 represents the gyrostabilizer dynamics about the precession axis. I_{44} is the mass moment of inertia of the ship about rolling direction by including the added inertia terms. B_{44} is the damping coefficient of the ship while C_{44} is the restoring coefficient the ship. I_g is the mass moment of inertia of the gyrostabilizer around precession axis, B_g is the damping coefficient and C_g is the restoring coefficient of the gyrostabilizer. θ_i indicates the angular motion of roll and precession motion for $i = 1,2$ respectively. τ_ω indicates the wave disturbance on the rolling direction and τ_p is the gyrostabilizer control torque. τ_p can actively controlled or it may be a restrictive type control. K_g is the angular momentum of the gyrostabilizers and finally n is the amount of the gyrostabilizer that used in the system.

Examining the Equations 2.37 and 2.38, it can be seen that both equations of motion contain a cosine term for the precession motion. The initial condition of the axis of rotation is, by definition, along the heave direction of the ship. For $\theta_2 = \pm 90°$ the spinning axis of the gyrostabilizer and ship's rolling axis are coincidence. That causes, cosine terms go to zero. If the gyrostabilizer is not actively controlled, there is no excitation terms in gyrostabilizer dynamics. Hence, there is no precession motion remains. Using similar analogy, the advantage of the vertical spin axis gyrostabilizer can be explained. As mentioned, the vertical spin axis gyrostabilizer has an equilibrium point for the enclosure system. The equilibrium point is simply around ($\theta_2 = 0°$) for the Equations 2.37 and 2.38. When these equations are investigated it is seen that cosine term gets the possible highest value. Other than that, their value gets lower. For that reason, gyrostabilizer system has higher performance around the initial enclosure condition.

The types of gyrostabilizers, their characteristics and related important issues are discussed. Basic information on gyrostabilizer control methods is provided. As mentioned above, gyrostabilizer control strategies are divided into two main groups as passive and active type of control (Towndsend and Ramandand, 2011). The passive type control system includes two sub-groups as (1) fixed restrictive load and (2) variably controlled restrictive load. In both groups there is a defined gyrostabilizer control torque ($\tau_g = X$) (where X is an arbitrary number). It is called a fixed restrictive load if the gyrostabilizer control torque is constant, otherwise it is called a variable controlled restrictive load. Although these control systems are easy to implement, they are the most inefficient method of control.

Active control is the control type where the precession rate is controlled by an actuator. It also has two sub-groups as (1) restricted precession and (2) unrestricted precession. As the name suggests, it is about the precession motion of the gyrostabilizer. In restricted precession, a certain amount of space is allowed in order to prevent the singularity. On the other hand, unrestricted precession uses all the working space of the precession motion. It uses the acceleration and deceleration of the spinning wheel at the singularity points to continue working.

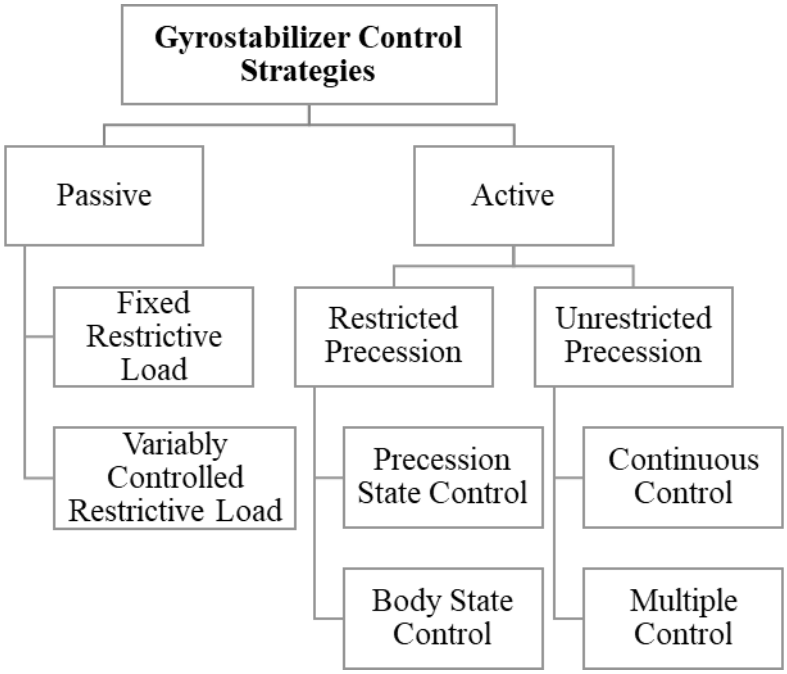

Figure 2.7. Gyrostabilizer control strategies (Source: Townsend and Ramanand, 2011)

The restricted precession type of control also has two sub groups as (1) precession state control and (2) body state control. In body state control as name suggest the body (i.e. ship) defines the precession rate. In the following a basic proportional type of control strategy is given as in Equation 2.39.

$$\dot{\theta}_2 = K_2 \dot{\theta}_1 \tag{2.39}$$

In given Equation 2.39, K_2 represents the proportional gain of the control strategy. By simply inserting the Equation 2.39 into the Equation 2.37 and using the small angle approximations the Equation 2.40 is obtained.

$$I_{44}\ddot{\theta}_1 + \left(B_{44} + nK_gK_2\right)\dot{\theta}_1 + C_{44}\theta_1 = \tau_\omega \tag{2.40}$$

Simply comparing the Equations 2.37 and 2.40, the damping coefficient of the ship motion increased from (B_{44}) to $\left(B_{44} + nK_gK_2\right)$. On the other hand, in precession state control, the generated gyrostabilizer control torque is generated with respect to precession motion as in Equation 2.41.

$$\tau_g = -K_b\dot{\theta}_2 - K_c\theta_2 \tag{2.41}$$

By simply inserting the Equation 2.39 into 2.38 and using small angle approximations the Equation 2.42 is obtained.

$$I_g\ddot{\theta}_2 + \left(B_g + K_b\right)\dot{\theta}_2 + \left(C_g + K_c\right) = K_g\dot{\theta}_1\cos(\theta_2) \tag{2.42}$$

Perez and Steinmann (2009) proved that the given precession state control is equivalent to the gain of body state control as in Equation 2.43.

$$K_2 = \frac{1}{\left(B_g + K_b\right) + \sqrt{\left(B_g + K_b\right)^2 - \left(I_g\left(C_g + K_c\right)\right)^2}} \tag{2.43}$$

The remaining unrestricted control strategies have different kind of approaches such as continues control strategies, extended Jacobian methods, singularity robust methods, reaction wheel control and multiple control strategies. Most of these control strategies are commonly used in control moment gyroscopes (Towndsend and Ramandand, 2011). The main focus of them is about avoiding the singularity points. The multiple control strategies can avoid the singularity by using any kind of control strategies. The reaction wheel control also uses the spinning wheel acceleration in order to generate a control torque (Townsend and Shenoi, 2014). This control method is not practically applicable in real systems because of the flywheel's size. The remaining control methods are based on Jacobian matrixes to find a solution to avoid the singularities.

2.4. Conclusion on Literature Survey

The background to ship dynamics, wave models, types of gyrostabilizers and their control strategies are reviewed in this chapter. The ship dynamics can be modelled using its moment of inertia, added mass, damping coefficients and restoring coefficients. However, for simplicity it is possible to model only the roll motion of the ship.

The moments acting on the ship can be modelled using different types of sea state models. Modelling the wave disturbance using the sea sates is important point for this study because it is main cause of the vessel roll motion.

Gyrostabilizers can be used in different arrangements and numbers. Each configuration has different advantages and disadvantages. Their types affect the control strategy. The control of the systems for gyrostabilizers is divided into two main group as active and passive. The mathematical proofs of the control systems are introduced. In this thesis, it is proposed to use vertical spin type gyrostabilizer with using active body state control strategies. The control algorithms and mathematical models are discussed in the following sections.

CHAPTER 3

THE MODEL OF A SCALE DOWN GYROSTABILIZER

In this section, the theoretical background of test rig for vessel and gyrostabilizer system is given. The test rig is designed in terms of the necessary components for a vessel and a gyrostabilizer. The 2D sketch of the system is given by defining the important parameters such as link lengths, rotation axis, etc. After that, using the 2D sketch of the test rig the dynamic analyses performed. These dynamic analyses show the relationships between vessel and gyrostabilizer. Finally, the model is transferred to Simulink to compare the error between analytical solutions and simulation results. The outputs of this section are employed in the prototyping of the test rig and the analysis of the control systems.

3.1. The Road Map for the Design of a Scaled-Down Gyrostabilizer

The section of the literature study on ships provides information about the ship roll motion and the metacenter point. A pendulum system was employed to simulate the ship's motion around the metacenter point. This will enable the establishment of a test system for the purpose of defining the ship's equation of motion.

Once the conceptual design has been determined, a free body diagram (FBD) of the system is created as a two-dimensional schematic. The FBD is populated with information such as the axes of motion, distances between joint points, and the center of mass, which are processed parametrically. A comprehensive kinematic and dynamic analysis of the system has been conducted, utilizing the aforementioned parameters.

In the third step, the 3D design of the system was created and transferred to the Simulink simulation environment. The accuracy of dynamic calculations is verified by comparing the results with the simulation data, using the physical properties extracted from the computer-aided design (CAD) software. Following the completion of the dynamic analyses, the DC motors to be utilized in the test rig have been selected, thereby initiating the prototype production phase.

3.2. The Gyrostabilizer System

This thesis considers the ship and the gyrostabilizer as three basic moving parts: (1) Ship, (2) Enclosure and (3) Flywheel. The ship part is responsible for the roll motion of the ship. It is connected to a pivot point with a revolute joint and can perform single axis rotational movement. The enclosure part is a connection part that allows the gyrostabilizer to make precession movement. This part connects the flywheel and the ship, and its angular velocity directly affects the counter damping moment produced. Finally, the flywheel is connected to the enclosure with a rotary joint. The rotational speed of this part and the mass moment of inertia on the axis of rotation form the angular momentum of the system. This generated angular momentum value, together with the precession rate, forms the anti-rolling torque of the system.

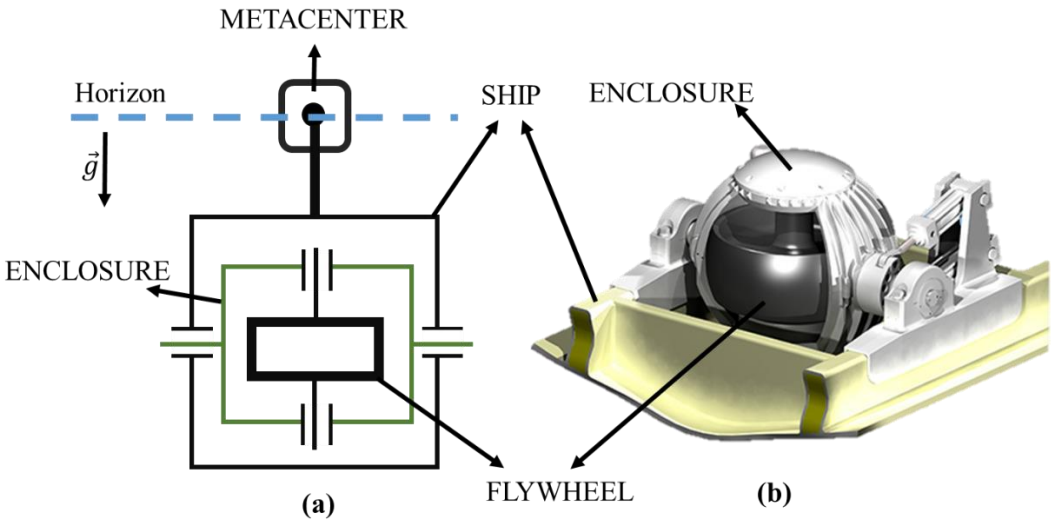

Figure 3.1.(a) The conceptual design of the gyrostabilizer system (b) CAD of a gyrostabilizer system that placed on a ship hull (Source: Allied Motion, 2021)

The conceptual design of the gyrostabilizer and ship system is carried out in accordance with the specifications set out in Figure 3.1. The relevant parts of the conceptual design are then matched with a real system. The ship, enclosure and flywheel are placed one after another using revolute joints. The system dynamic analysis is carried out as a serial manipulator, but the design is completed as a parallel system to achieve a higher level of stiffness.

3.3. The Gyrostabilizer Dynamics

Once the conceptual design of the gyrostabilizer and ship system has been completed, the dynamic analyses are carried out. The first step in the dynamic analysis is to draw a free body diagram of each part of the system as seen in Figure 3.2, 3.3 and 3.4. In the drawing, the center of mass of each part is defined as G_i where $i = 1,2,3$. The subscript (i) is used to define which part it belongs to, namely the ship, enclosure and flywheel, respectively. Additionally, the linear acceleration, angular acceleration and angular velocity are defined as $\vec{a}_i$, $\vec{\alpha}_i$ and $\vec{\omega}_i$ respectively. The revolute joint's location is defined as O_i. The body axes are defined as $\vec{u}_1^{(i)}$, $\vec{u}_2^{(i)}$ and $\vec{u}_3^{(i)}$. Subsequently, the rotation of the components is defined by θ_i. The position of the pivot points and mass centers are defined as r_{ij} and g_{ij} where $i = 1,2,3$ and $j = 1,2,3$ respectively. Finally, the acting forces and torques are defined as $\vec{F}_{ij}$ and $\vec{M}_{ij}$.

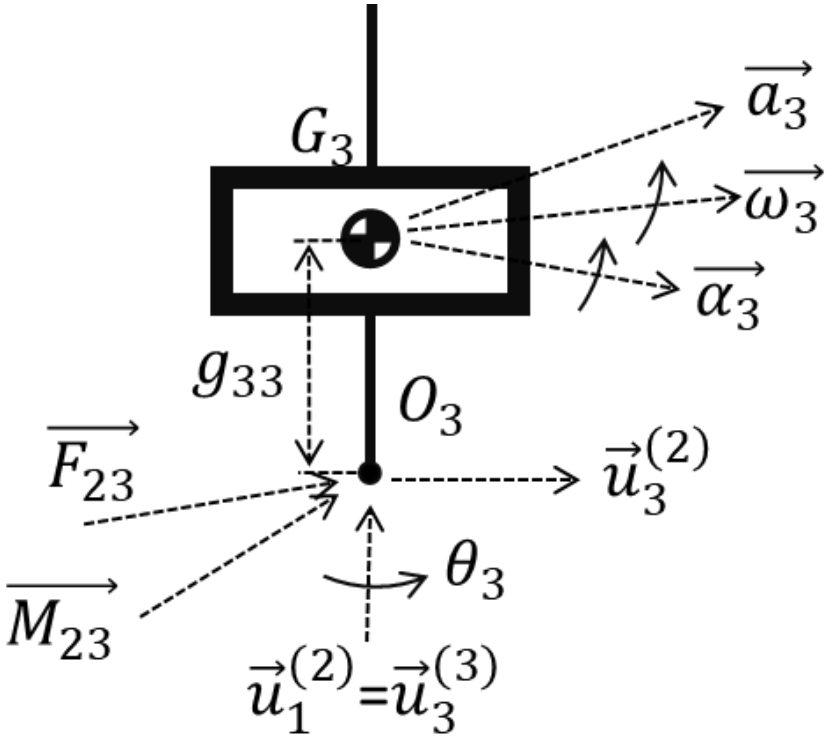

Figure 3.2. The free body diagram of flywheel

Once the parameters of the free body diagrams have been defined, the kinematic analyses are performed in order to determine the linear acceleration, angular acceleration and angular velocity of each mass center.

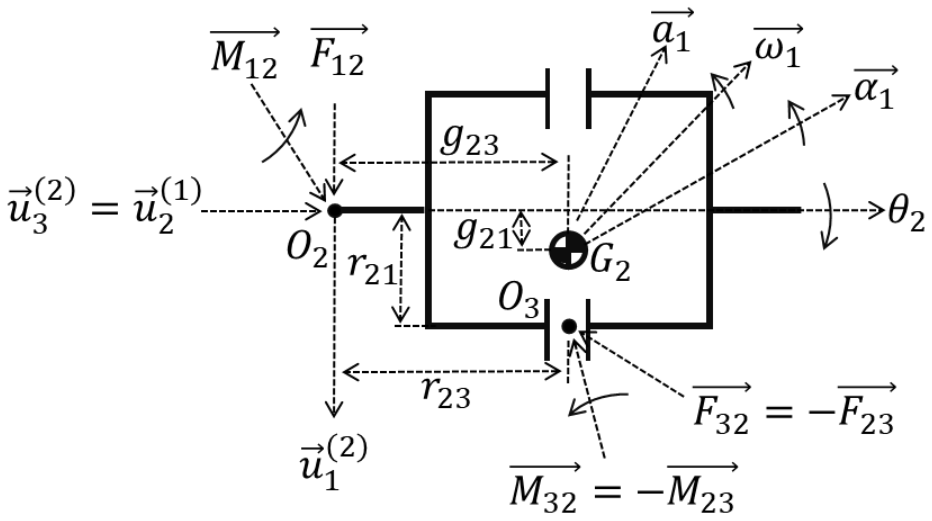

Figure 3.3. The free body diagram of enclosure

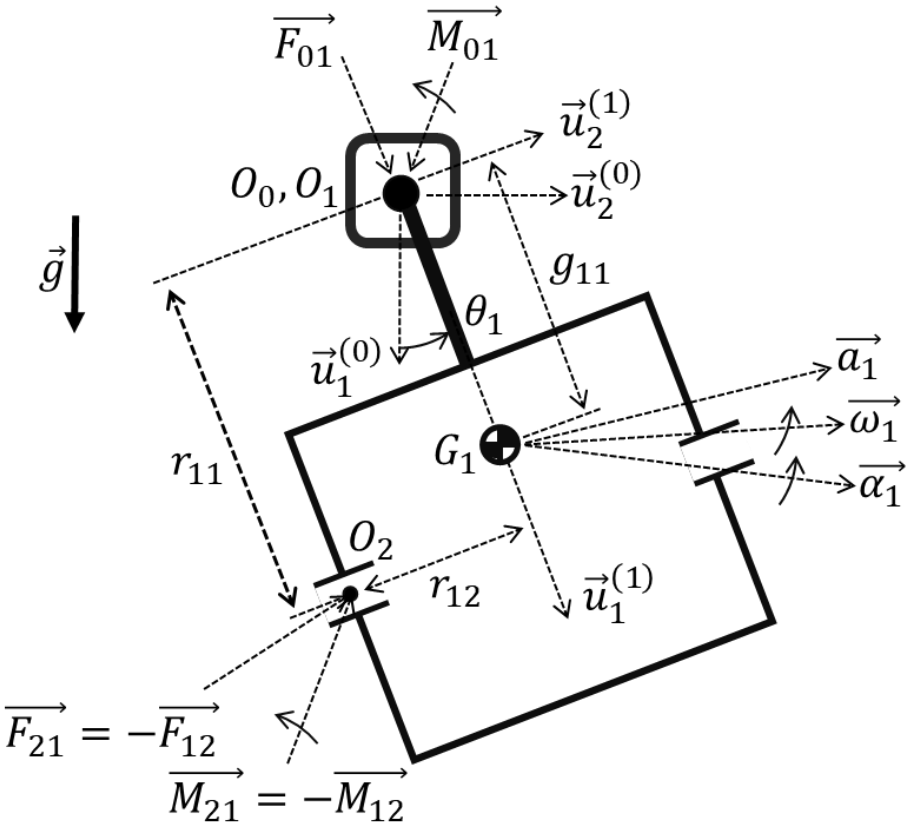

Figure 3.4. The free body diagram of ship

3.3.1. The Gyrostabilizer Kinematic Analyses

In the context of performing kinematic analyses of any system, it is first necessary to define the rotation matrices for each individual component. Subsequently, the

kinematic analyses are conducted at the level of individual positions for each component of the system. Subsequently, the angular velocity and angular acceleration of each component is calculated using the rotation matrices. Once the angular velocity and angular acceleration analyses have been completed, the linear velocity and linear acceleration of each mass center is determined.

For each axes the rotation matrixes are written one by one. For the rotation about $\vec{u}_1$ (or x axes) is defined as in Equation 3.1.

$$\hat{R}_1(\theta) = \begin{bmatrix} 1 & 0 & 0 \\ 0 & \cos(\theta) & -\sin(\theta) \\ 0 & \sin(\theta) & \cos(\theta) \end{bmatrix} \tag{3.1}$$

The rotation about $\vec{u}_2$ (or y axes) is defined as in Equation 3.2.

$$\hat{R}_2(\theta) = \begin{bmatrix} \cos(\theta) & 0 & \sin(\theta) \\ 0 & 1 & 0 \\ -\sin(\theta) & 0 & \cos(\theta) \end{bmatrix} \tag{3.2}$$

The rotation about $\vec{u}_3$ (or z axes) is defined as in Equation 3.3.

$$\hat{R}_3(\theta) = \begin{bmatrix} \cos(\theta) & -\sin(\theta) & 0 \\ \sin(\theta) & \cos(\theta) & 0 \\ 0 & 0 & 1 \end{bmatrix} \tag{3.3}$$

After defining each rotation matrix, the gyrostabilizer and ship system transformation matrices is written as given Equation 3.4.

$$\begin{aligned} \hat{C}^{(0,1)} &= \hat{R}_3(\theta_1) \\ \hat{C}^{(1,2)} &= \hat{R}_1\left(-\frac{pi}{2}\right)\hat{R}_3(\theta_2) \\ \hat{C}^{(2,3)} &= \hat{R}_1\left(-\frac{pi}{2}\right)\hat{R}_3(\theta_3) \end{aligned} \tag{3.4}$$

In given Equation 3.4 the $\hat{C}^{(i,j)}$ represents the transformation between part (j) and (i) with respect to part (i). Using these rotation matrices each rotation is defined with respect to base frame by using matrix multiplications. After defining the transformation

matrices, the position level kinematic analyses of each part are defined as using Equation 3.5

$$\vec{r}_{O_0G_i} = \vec{r}_{O_0O_i} + \hat{C}^{(0,i)}\vec{r}_{O_iG_i} \tag{3.5}$$

Once the position-level analyses have been completed, the angular velocity of each component should be analyzed. This should be done by defining a joint space angular velocity for each component, which is denoted by $\dot{\theta}_i$ where $i = 1,2,3$ for the ship, enclosure and flywheel, respectively. The angular velocity of the parts, measured from the base, is designated as $\vec{\omega}_{i/0}$. Furthermore, the representation of $\vec{\omega}_{i/i-1} = \dot{\theta}_i\vec{u}_3^{(i)}$ is valid for given free body diagrams. Consequently, the angular velocity of each system component is determined by employing the following Equation 3.6.

$$\vec{\omega}_{i/0} = \vec{\omega}_{i/i-1} + \vec{\omega}_{i-1/i-2} \dots \vec{\omega}_{1/0} \tag{3.6}$$

Once the angular velocity of each component has been determined, the angular accelerations is calculated for $\vec{\alpha}_{i/i-1} = \ddot{\theta}_i\vec{u}_3^{(i)}$, where $i = 1,2,3$ for the ship, enclosure and flywheel, respectively. $\ddot{\theta}_i$ represents the joint space angular acceleration for each component.

$$\vec{\alpha}_{i/0} = \vec{\alpha}_{i-1/0} + \vec{\alpha}_{i/i-1} + \vec{\omega}_{i/0} \times \vec{\omega}_{i/i-1} \tag{3.7}$$

The velocity level kinematic analyses are performed with using the following Equation 3.8.

$$\vec{V}_{P/0}^{(d0)} = \vec{V}_{P/A}^{(di)} + \vec{\omega}_{A/0} \times \vec{r}_{P/A} + \vec{V}_{A/0}^{(do)} \tag{3.8}$$

In Equation 3.8 $\vec{V}_{P/0}^{(d0)}$ shows the P point linear velocity with respect to metacenter location (O_0) and (d0) shows the derivation frame. Similarly, $\vec{V}_{P/A}^{(di)}$ shows the P point linear velocity with respect to A point and shows the derivation frame. In the given system there is no linear joint so these terms come zero for all parts. Finally, after defining the

linear velocities, the linear acceleration is determined with using the following Equation 3.9.

$$\vec{a}_{P/0}^{(d0)} = \vec{a}_{P/A}^{(di)} + 2\vec{\omega}_{i/0} \times \vec{V}_{P/A}^{(di)} + \vec{\alpha}_{i/0} \times \vec{r}_{P/A} + \vec{\omega}_{i/0} \times \left(\vec{\omega}_{i/0} \times \vec{r}_{P/A}\right) + \vec{a}_{A/0}^{(d0)} \quad (3.9)$$

In Equation 3.9 the linear acceleration of P point with respect to the metacenter location (O_0) and derived in 0th frame as $\vec{a}_{P/0}^{(d0)}$. Similarly, velocity analyses because of lack of the linear joint the $\vec{a}_{P/A}^{(di)}$ term becomes 0 for all equations.

The kinematic analyses of the proposed system are carried out using the provided Equations (3.1 to 3.9). The kinematic analyses were conducted by sequentially examining the kinematic properties of each body in the system, beginning with the first body (ship) and concluding with the last body (flywheel). This involved examining the kinematic properties of each pivot and mass center location.

3.3.2. The Gyrostabilizer Dynamic Analyses

Once the kinematic analyses of the proposed system have been completed, the dynamic analyses are carried out using calculated acceleration and velocity terms and incorporating the mass properties of each part. The calculations are carried out in order to define the reaction torques and forces on the connection points. In contrast to kinematic analyses, dynamic analyses start with the last part and proceed in a step-by-step manner to the first part. In dynamic analyses, the forces acting at each connection point must be calculated using the following Equation 3.10.

$$m_i \vec{a}_i = \vec{F}_{(i-1)i} + \vec{F}_{(i+1)i} + m_i \vec{g} \quad (3.10)$$

In Equation 3.10, the mass of the component is designated as m_i. The forces acting on the system are designated as $\vec{F}_{(i-1)i}$ and $\vec{F}_{(i+1)i}$. The subscript in the forces indicates the direction of the force. In response, the magnitude of the force is equal for each body, but its direction changes. The force acting on body i is equal to the force acting on body i+1, but in opposite directions $\vec{F}_{(i+1)i} = -\vec{F}_{i(i+1)}$.

Once the forces acting at the connection points have been defined, the reaction and actuation torques are calculated using Equation 3.11. Furthermore, the mass moment of inertia properties of each point must be defined as a two-dimensional tensor, $\check{J}_i$ where $i = 1,2,3$ for the ship, enclosure and flywheel.

$$\check{J}_i \cdot \vec{\alpha}_i + \vec{\omega}_i \times \check{J}_i \cdot \vec{\omega}_i = \vec{M}_{i(i+1)} - \vec{r}_{i(i+1)} \times \vec{F}_{i(i+1)} \tag{3.11}$$

Once the dynamic analyses have been completed, the resulting equations are written in Simulink in order to verify the accuracy of the analytical solutions. In order to achieve this, it is necessary to perform a computer-aided design (CAD) of the scaled-down gyrostabilizer system.

3.4. CAD of the Gyrostabilizer Test System

Once the conceptual design has been finalized, the computer-aided design (CAD) of the ship and the gyrostabilizer system is carried out. The most crucial aspect of the system is to mimic the ship's capacity to roll around the metacentric axis. Figure 3.5 illustrates the conceptual design and CAD of the system. Figure 3.6 illustrates the motion capability of the gyrostabilizer system. In this instance, the joint space motions of the ship and enclosure are designated as θ_1 and θ_2, respectively.

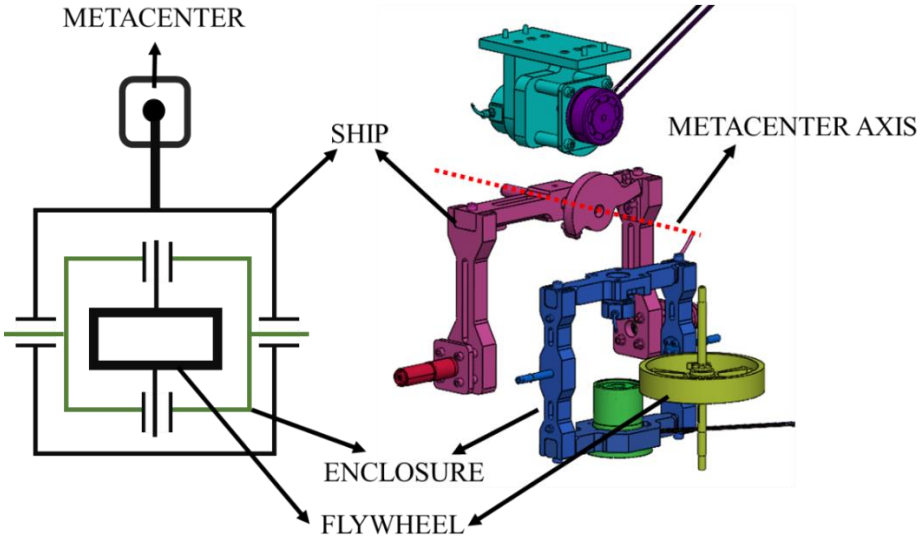

Figure 3.5. The exploded view of proposed gyrostabilizer and ship system

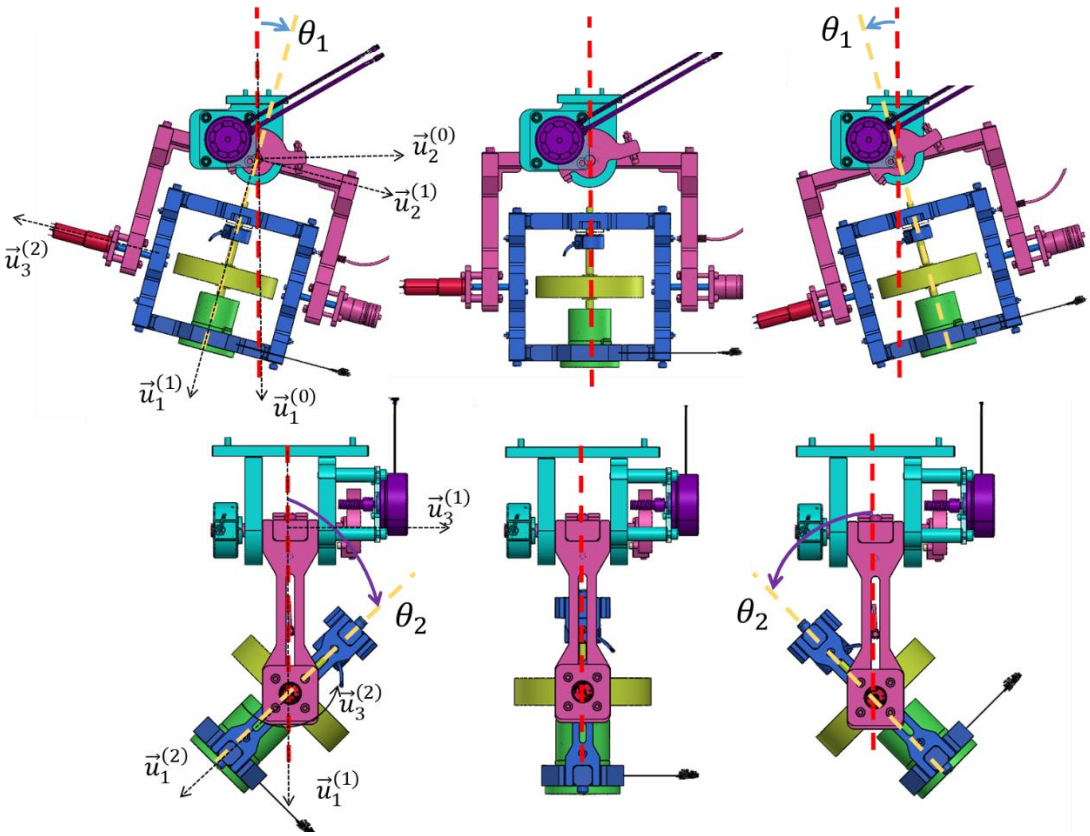

Figure 3.6. The motion capability of the proposed system

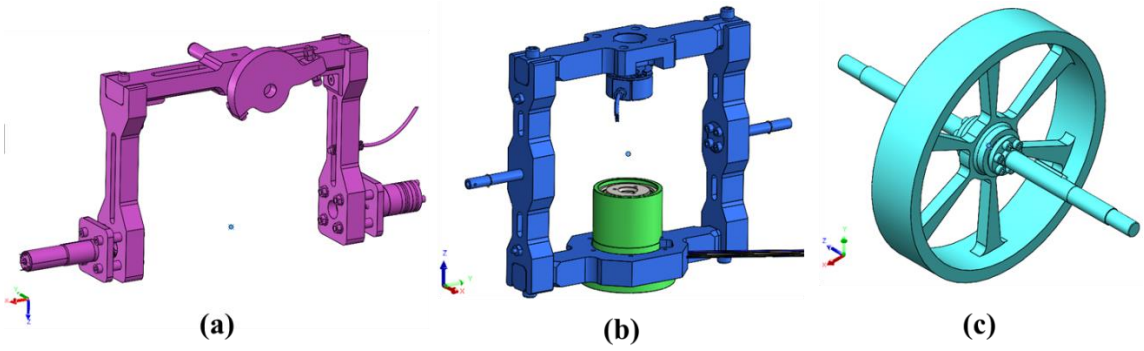

Figure 3.7. CAD of (a) Ship (b) Enclosure and (c) Flywheel

Figure 3.7 illustrates the CAD parts of the proposed system, which include (a) the ship, (b) the enclosure, and (c) the flywheel. The material of the ship part is defined as 6061, the housing is composed of 6061 and 4140, and finally the flywheel part is composed of ST52 and 4140 steel. The design of the system has been completed in SolidWorks. The mass and moment of inertia values were obtained from the SolidWorks Mass Properties function. The design mass properties of the proposed system are presented in Table 3.1. The design parameters of the system are tabulated in Table 3.2.

Table 3.1. The physical properties of each part of proposed system

	Mass [kg]	Mass Moment of Inertia [kgm^2]
Ship	$m_1 = 6.931$	$J_1 = \begin{bmatrix} 0.09285 & -0.00021 & -0.00592 \\ -0.00021 & 0.32194 & 0.00477 \\ -0.00592 & 0.00477 & 0.2440 \end{bmatrix}$
Enclosure	$m_2 = 7.016$	$J_2 = \begin{bmatrix} 0.10932 & 0.00042 & 0.00001 \\ 0.00042 & 0.06548 & -0.00001 \\ 0.00001 & -0.00001 & 0.050930 \end{bmatrix}$
Flywheel	$m_3 = 3.43$	$J_3 = \begin{bmatrix} 0.01177 & 0.00000 & 0.00000 \\ 0.00000 & 0.01177 & 0.00000 \\ 0.00000 & 0.00000 & 0.01834 \end{bmatrix}$

Table 3.2. The design parameters of the proposed system

$g_{11} = 101.23\ [mm]$	$r_{11} = 235[mm]$	$r_{12} = 184.5[mm]$
$g_{23} = 184.5[mm]$	$g_{21} = 0\ [mm]$	$r_{21} = 163.24[mm]$
$r_{23} = 184.5[mm]$	$g_{33} = 163.24[mm]$	

Once the design of the proposed gyrostabilizer and ship system has been completed, it is transferred into the Simulink environment in order to compare the dynamic analyses.

3.5. Simulink Model of the Gyrostabilizer System

Figure 3.8 illustrates the Simulink model of the proposed gyrostabilizer and ship system. In the Simulink model, the parts are connected using revolute joints. These joints are designated as the Wave Imitating Motor, Precession Motor and Flywheel Motor, respectively. The joint blocks are initially defined as Motion Input. The reason for setting the motion input is to facilitate comparison between the simulation results and the analytical solutions.

In order to facilitate a comparison between the simulation results and the analytical solutions, the kinematic and dynamic equations mentioned in section 3.3 are coded using MATLAB function blocks. A sine wave with an amplitude of 180˚ and a frequency of 10 [rad/s] is generated. Subsequently, the aforementioned motion input is applied to each joint. After wards, the requisite data, including position, velocity, acceleration, reaction forces and total torque, are acquired through the utilization of Simulink blocks. The initial step is to investigate the error associated with the kinetic

analysis. Figure 3.9 illustrates the discrepancy between the analytically calculated and measured signals. Subsequently, the results of the dynamic analyses are compared with one another, as illustrated in Figure 3.10.

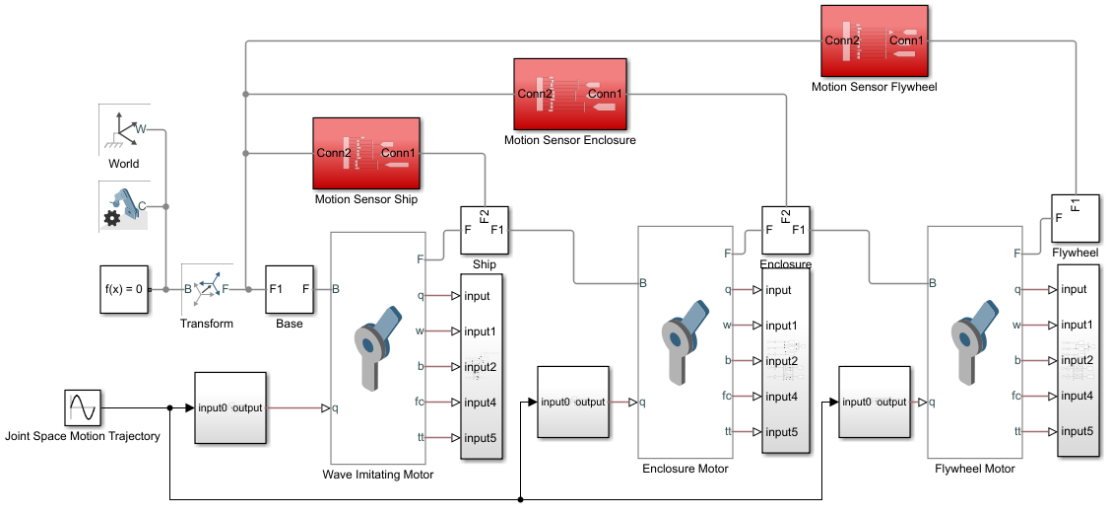

Figure 3.8. Fundamental structure of Simulink Model of the proposed system

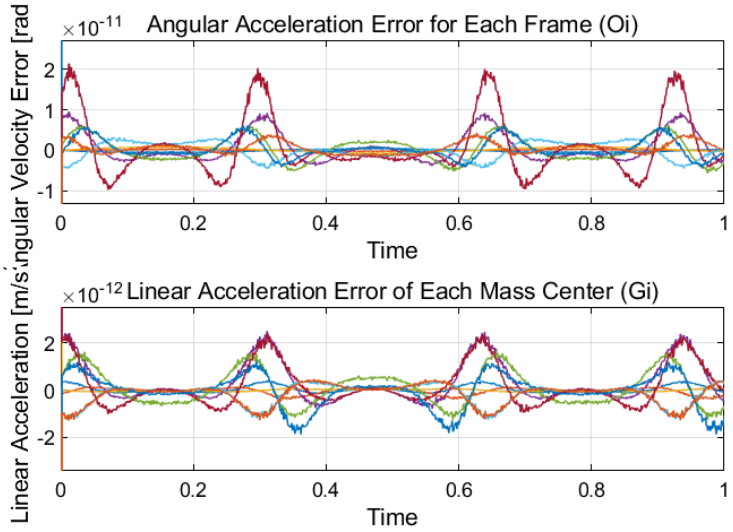

Figure 3.9. Kinematic analyses error chart for each mass center (Gi) and pivot point (Oi)

Figure 3.9 illustrates the discrepancy between the measured and calculated signals in kinematic analyses. Upon examination of the error level, it is observed that the greatest error is observed in the linear acceleration terms, with a value of 10^{-11} $[m/s^2]$. This value is close to the numerical error level. Consequently, the kinematic analyses are accepted as accurate.

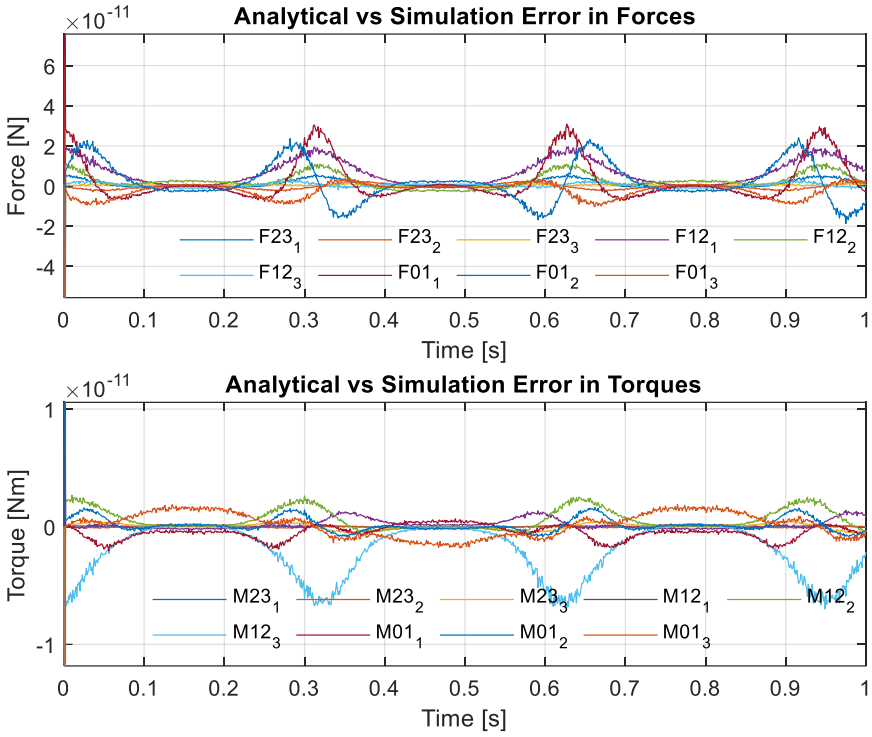

Figure 3.10. Dynamic analyses error comparison for each pivot point (O_i)

Figure 3.10 illustrates the discrepancy between the calculated and measured dynamic properties for each direction. Upon examination of the error levels, it becomes evident that the error associated with the force analysis falls within the range of $10^{-10}[N]$, while that of the torque level analysis is approximately $10^{-11}[N \cdot m]$. This value is close to the numerical error level. Consequently, the dynamic analyses are accepted as accurate.

The results of the kinematic and dynamic analyses have enabled the determination of an equation of motion for the scaled-down gyrostabilizer system, which is used for control system analyses. Furthermore, the Simulink file created should be utilized to calculate the reaction force and torques. Subsequently, these values must be compared to the strength of the materials prior to the system being prototyped.

Once the dynamic analyses have been completed, the aforementioned motion blocks on the metacenter are removed from the Simulink model. Subsequently, the input of the Wave Imitating Motor block is set to Torque Input/Motion Calculated. The rationale behind this configuration is to create a back-drivable joint. In this manner, the generated disturbance torques are attenuated by means of the gyrostabilizer dynamics. Following the aforementioned modifications to the Wave Imitating Motor block, the resulting Simulink model is as depicted below.

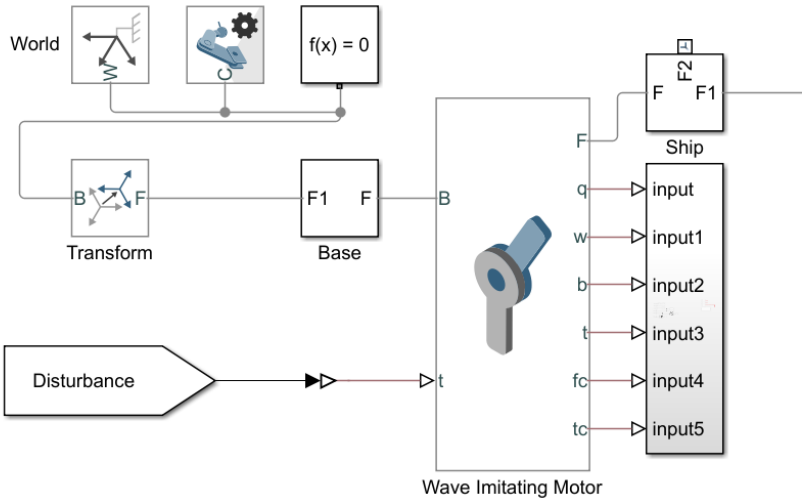

Figure 3.11. Wave imitating motor block on Simulink model

In the proposed test system, it is planned to utilize a DC motor to generate precession motion. Consequently, the precession motor block is integrated with a DC motor model generated using the Rotational Multibody Interface. The proposed DC motor model incorporates a number of components, including dampers, inertia, resistors and inductors, in order to create a simulation model of a DC motor. Additionally, a gearbox is employed to enhance the system torque. The proposed precession motor model is depicted in Figure 3.12. The subsequent sections will discuss the mathematical representation of a given model.

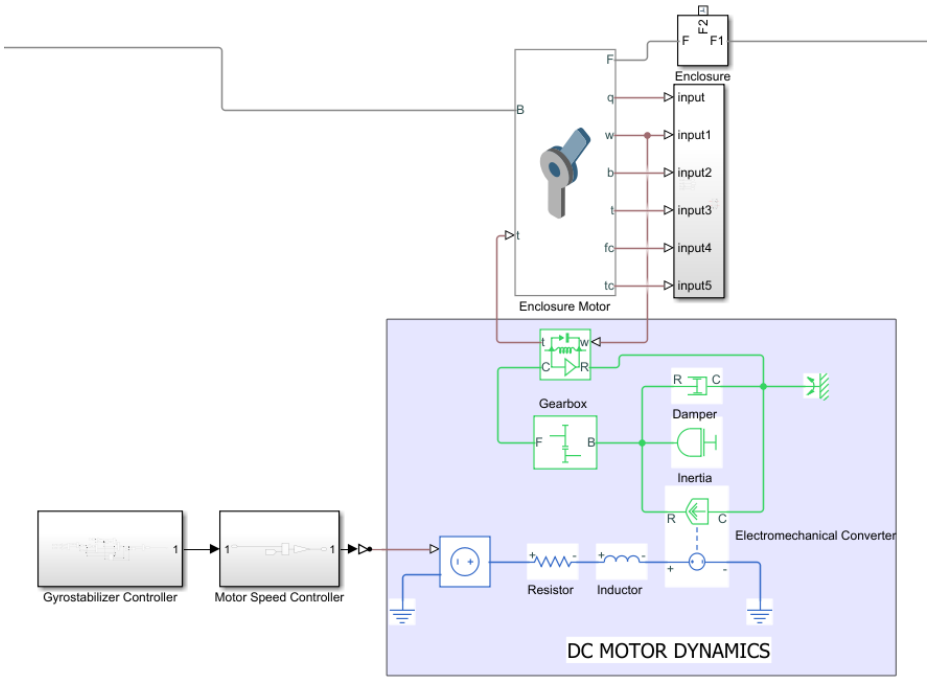

Figure 3.12. Updated precession motor joint on Simulink model

The revised Precession Motor Joint comprises two controllers. The initial controller is the primary gyrostabilizer controller. The controller then takes the inputs and generates the desired precession motion. The second controller is the Motor Speed Controller, which takes the desired speed and actual speed as input. Subsequently, a voltage output is generated to rotate the motor utilizing a voltage source. Consequently, the desired motion will be generated via the electromechanical converter. Subsequently, the precession motion occurs within the enclosure system, taking into account the dynamics of the motor.

Finally, no specific alteration was made to the last joint (flywheel). This is defined as the Motion Input/Torque Calculated. The input to the system is a velocity level ramp that reaches the targeted value.

3.6. Summary of the Modelling a Scaled-Down Gyrostabilizer

This section presents a kinematic and dynamic analysis of the scaled-down gyrostabilizer system. Firstly, a conceptual design of the test rig is performed using the existing ship and gyrostabilizer model. Subsequently, the FBDs of the test rig are drawn individually. The FBDs include the definition of the axes, connection points, mass centers and body axes. Subsequently, rotation and transformation matrices are defined. After that, the position, velocity and acceleration level kinematic analyses are conducted. Then, the aforementioned kinematic analyses are employed for the purpose of dynamic analyses. Ultimately, the results of the analytic calculations are compared to those of the simulations for the purpose of verification. Once the verification process has been completed, the Simulink file is revised for the purpose of conducting control system studies.

CHAPTER 4

DESIGN OF THE GYROSTABILIZER CONTROL SYSTEM

This section provides an overview of the fundamental concepts of classical control systems, including feedback, actuators, plants and controllers. A portion of Chapter 4 presents the derivation of sensory feedback of the roll angle from the roll rate and linear accelerations. This is followed by a discussion of DC motors, with particular attention paid to the system actuators. Subsequently, the plant and the proportional-integral (PI) control system are subjected to examination. Finally, the concepts of full state feedback control and linear quadratic regulator (LQR) are introduced. Finally, the differences between the designed controllers are presented.

4.1. Sensory Feedback

A basic feedback control system comprises four main components: a body, an actuator, a sensor and a controller. The primary objective of a control system is to modify the state of the body through the use of the actuator. In open-loop systems, the controller is capable of generating command signals without the necessity for feedback. However, for a closed-loop control system, it is necessary to determine the state of the body using the sensors. Although the system is equipped with high-quality actuators and fast controllers, its performance is negatively affected when the sensor is of low quality. Consequently, the feedback system represents one of the most crucial components of a closed-loop control system.

As mentioned before, the aim of this work is to minimize the roll motion of the ship around its initial state ($\theta_1=0$). Therefore, the state of the hull needs to be measured. It is easy to measure the ship's roll rate using gyroscopic sensors. They can measure angular velocity. However, the ship's roll angle is also a required feedback signal for the control system.

It is theoretically possible to determine the roll angle from the roll rate by integration. However, the imperfections of the sensor and the noise on the cables result

in integration drift. Furthermore, in order to define the roll angle by integrating the roll rate, it is of the utmost importance to be aware of the initial state of the roll angle. It is not possible to ascertain the initial state of the roll angle for a ship at sea.

An alternative approach to defining the roll angle (or pitch) is to utilize an accelerometer (Euston et al., 2008). The fundamental premise of this methodology is the utilization of the direction of gravity acceleration. Accelerometers are instruments that measure the acceleration of a body. For the purposes of illustration, consider the accelerometer as depicted in Figure 4.1. The accelerometer has two axes of measurement, designated as the x and y axes. The acceleration due to gravity is perpendicular to the horizon.

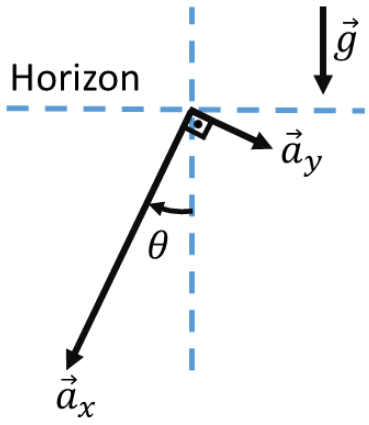

Figure 4.1. Free body diagram of an accelerometer for measuring tilt angle

It is established that the x and y directions of the provided example are perpendicular to each other. Consequently, if the magnitude of the acceleration for each axis is known, the given angle θ is determined by means of inverse tangent functions. In the context of programming languages, the most appropriate function to employ in this instance is the "atan2" function, which takes into account the sign of the inputs. The following Equation 4.1 allows the given angle to be determined (Euston et al., 2008).

$$\theta = atan2\left(|\vec{a}_y|, |\vec{a}_x|\right) \tag{4.1}$$

Although the use of an accelerometer is suitable for low-speed applications, it is not a suitable choice for high-speed applications. In high-speed applications, the acceleration of the body or vibration on the system may become more dominant than the acceleration of gravity. Consequently, it is unable to generate accurate angle data.

In summary, the use of a gyroscope sensor has advantages in handling dynamic systems, but over time, there is an integral drift problem. Furthermore, it is essential to ascertain the initial state of the system. Conversely, the use of an accelerometer does not necessitate the calculation of the initial state, but it is highly susceptible to vibrations. The optimal approach to measuring the roll angle of a system is to combine these two approaches with the use of a sensor fusion algorithm. As previously stated, long-term data is unsuitable for gyroscope measurements, while short-term data is similarly inadmissible for accelerometer measurements. The complementary filter handles the gyroscope and accelerometer data in accordance with the illustration in Figure 4.2.

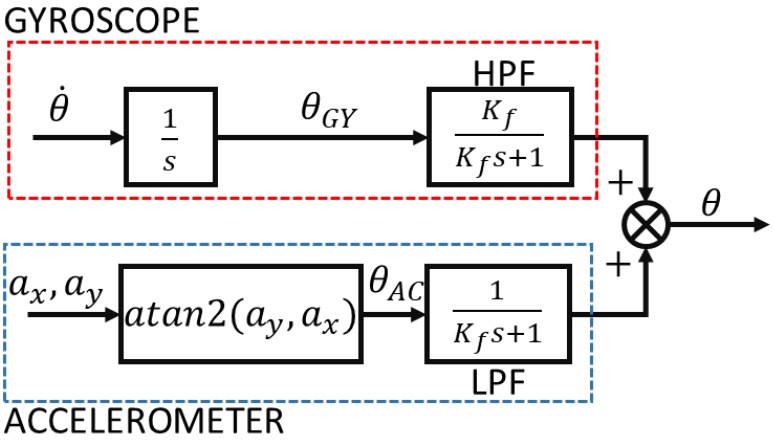

Figure 4.2. Complementary filter block diagram

Figure 4.2 illustrates the fundamental operational principle of the complementary filter system. In order to minimize the effect of integral drift, a high-pass filter is employed on the gyroscope side of the system. Additionally, a low-pass filter is employed on the accelerometer side to mitigate the impact of vibration. In this manner, the advantageous aspects of the accelerometer and gyroscope are employed, while the disadvantages of the system are mitigated.

It is necessary for the complementary filter block diagram to run on a discrete controller. Accordingly, the following mathematical equations are implemented on the STM32 Discovery Board in this thesis.

$$\theta_i = K_{comp}\left(\theta_{i-1} + \dot{\theta}_i(t_i - t_{i-1})\right) + (1-K)atan2(a_y, a_x) \tag{4.2}$$

In Equation 4.2, θ_i represents the roll angle of the system, θ_{i-1} is the roll angle calculated in the previous cycle, $\dot{\theta}_i$ is the roll rate, t_i is the cycle time, t_{i-1} is the previous cycle time, a_y is the acceleration in the y direction, a_x is the acceleration in the x direction, and finally K_{comp} is the gain of the complementary filter. In this thesis, a series of experiments were conducted to identify the optimal value for the K_{comp} parameter. The results indicated that a value of 0.98 was the most effective.

4.2. DC Motor Dynamics

The actuator is a key component within a control system. If the actuator is unable to accommodate the inputs, the system will not function as intended. It is therefore essential to understand the dynamics of the motor. A DC motor can be modelled using basic electrical and rotational elements, including resistance, inductance, inertia and damping. It is well known that a DC motor consists of a number of coils. It is possible for these coils to create inductance due to the properties of magnetism. Conversely, the wires of the coils impede the flow of current through the system. Once the electrical energy has been converted into mechanical energy, the mechanical energy is dissipated from the system via a shaft. The shaft also has a mass moment of inertia. Finally, the friction on the bearings of the motor is represented by the damping coefficient. A basic schematic and block diagram of a DC motor system is shown in Figure 4.3.

Figure 4.3 (a) presents a physical representation of a DC motor system. As seen, a closed electrical circuit is established, which generates a rotational motion. The applied voltage (v) is distributed among the resistor (R_m), the inductance (L_m) and the back-emf (e) component of the system. It is known that the back-emf voltage is expressed as $\left(e = K_b\dot{\theta}\right)$ where "K_b" is the back-emf constant. The application of Kirchhoff's law allows the derivation of the following Equation 4.3.

$$v = R_m i + L_m \frac{di}{dt} + K_b\dot{\theta} \tag{4.3}$$

It is also known that, there is a direct relationship between the shaft torque and current as ($T = K_m i$) where "K_m" is the torque constant. Finally, Equation 4.4 is written as in Equation 4.4.

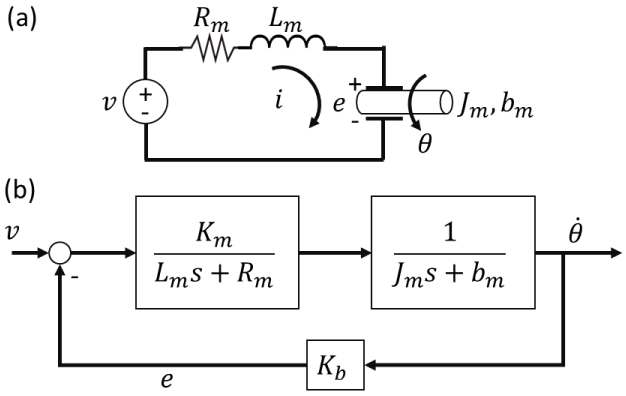

Figure 4.3. (a) Physical representation of a DC motor system (b) Block diagram representation of a DC motor system

$$J\ddot{\theta} + b\dot{\theta} = K_m i \tag{4.4}$$

Using the Laplace transform, the Equation 4.3 and 4.4 is written as in Equation 4.5.

$$s(J_m s + b_m)\theta(s) = K_m I(s) \tag{4.5}$$

$$(L_m s + R_m)I(s) = V(s) - K_b s\theta(s) \tag{4.6}$$

Following simplification is written by combining the Equation 4.5 and 4.6.

$$\frac{s\theta(s)}{V(s)} = \frac{\dot{\theta}(s)}{V(s)} \frac{K_m}{(J_m s + b_m)(L_m s + R_m) + K_m K_b} \tag{4.7}$$

Upon examination of the resulting transfer function as depicted in Figure 4.3b, it becomes evident that the same closed-loop transfer function is obtained. Equation 4.7 represents a second-order system. However, it may be further simplified by neglecting the inductance parameter. In this study, a Maxon RE 30 motor is employed in conjunction with a gearbox exhibiting a reduction ratio of 159:1. The catalogue parameters of the DC motor are tabulated in Table 4.1. By applying the specified parameters to Equation 4.7 (DC motor transfer function), the second-order transfer function is derived as given in (4.8). It is also essential to construct a Bode diagram of the DC motor system in order to demonstrate its performance at different frequencies.

Table 4.1. DC Motor and Gearbox parameters

Motor Parameter	**Value**	**Unit**
Terminal Resistance	0.196	Ohm
Terminal Inductance	0.0000344	H
Rotor Inertia	33.9 (10^{-7})	kgm^2
Back-emf constant	0.0135	V/[rad/s]
Torque Constant	0.0103	Nm/A
Mechanical Time Constant	3.64	ms
Gearbox Inertia	0.7 (10^{-7})	kgm^2
Gearbox Ratio	159:1	#

$$\frac{0.0103}{1.19(10^{-9})s^2 + 6.782(10^{-7})s + 0.000139} \tag{4.8}$$

Upon examination of Figure 4.4, it becomes evident that the system corner frequency is approximately 200 [rad/s], corresponding to 31.83 [Hz]. It is known that the harmful oscillation for humans is around 0.2 [Hz] to 0.5 [Hz]. Hence, the motor dynamics exhibit a higher level of performance than that of the sea states. It can therefore be concluded that DC motor choice of application is optimal.

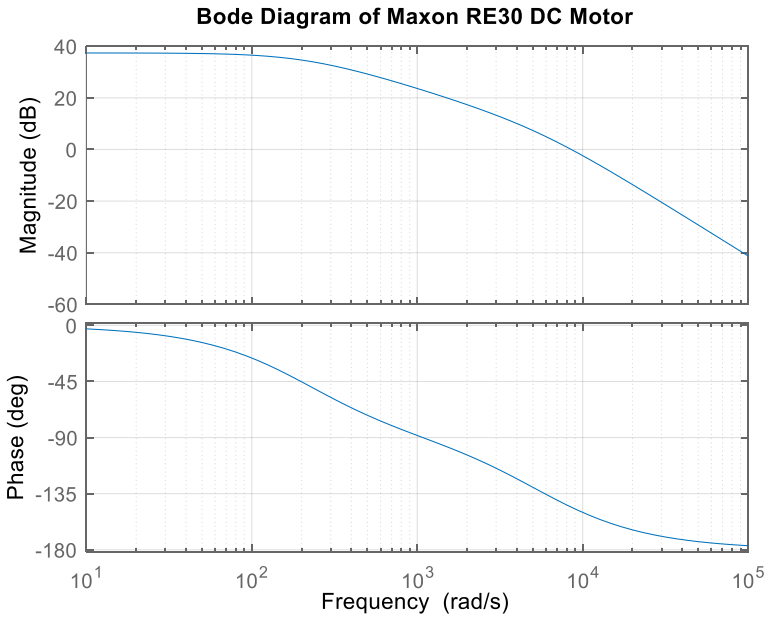

Figure 4.4. Bode diagram of DC Motor

4.3. Design of the PV-PI Control System

The most important aspect of a control system design is the definition of the dynamics of the system. Consequently, the dynamic analysis of the vessel system should take precedence over the design of the control system. The dynamic analyses of the test rig are presented in Chapter 3.3, "The Dynamics of the Gyrostabilizer". The equation of motion for the axes of the system and actuator are obtained using the derived equation. The equation of motion about the metacenter axis for the test stand was derived as following Equation 4.9.

$$\begin{aligned} M_{011}^{r} = g[&m_3(\sin\theta_1\cos\theta_2\,(r_{21}-g_{33})+\cos\theta_1\,(r_{12}-g_{23})+r_{11}\sin\theta_1) \\ &+ m_2(\cos\theta_1\,(r_{12}-g_{23})+r_{11}\sin\theta_1)+m_1 g_{11}\sin\theta_1] \\ &+ \ddot{\theta}_1\big[m_3(r_{12}-g_{23})(\cos\theta_2\,(r_{21}-g_{33})+r_{11})+m_2 r_{11}^2+m_1 g_{11}^2 \\ &+ \cos^2\theta_2\left(J_{3_{11}}+J_{2_{11}}\right)+\sin^2\theta_2\left(J_{3_{33}}+J_{2_{33}}\right)+J_{1_{11}}\big]+\ddot{\theta}_3 J_{3_{33}}\sin\theta_2 \\ &+ 2\dot{\theta}_1\dot{\theta}_2\sin\theta_2\cos\theta_2\left(J_{3_{33}}-J_{3_{11}}+J_{2_{33}}\right) \\ &+ \dot{\theta}_2\dot{\theta}_3\cos\theta_2\left(J_{3_{11}}-J_{3_{22}}+J_{3_{33}}\right) \\ &+ \dot{\theta}_1^2(m_2+m_3)(r_{12}-g_{23})(r_{12}-g_{23}) \end{aligned} \tag{4.9}$$

The given equation of motion about metacenter can be simplified to get a linear 2nd order transfer function. It is possible to eliminate the non-linear terms and accept the enclosure angle (precession angle $\theta_2 = 0$) as zero. Also using the small angle approximation for the ship angle ($\theta_1 \approx 0, \sin\theta_1 \cong \theta_1, \cos\theta_1 \cong 0$) enables the system can be linearized. Furthermore, the required values are given in Table 3.2 such as $r_{21} = g_{33}$, $r_{12} = g_{23}$ and $J_{3_{11}} = J_{3_{22}}$. The linearized system is expressed as in Equation 4.10.

$$\begin{aligned} M_{011}^{r} = \tau_\omega = &\left[(m_3+m_2)r_{11}^2+m_1 g_{11}^2+J_{1_{11}}+J_{3_{11}}+J_{2_{11}}\right]\ddot{\theta}_1 \\ &+ g[(m_2+m_3)r_{11}+m_1 g_{11}]\theta+\dot{\theta}_2\dot{\theta}_3 J_{3_{11}} \end{aligned} \tag{4.10}$$

Upon examination of the linear model, it is observed that it nearly aligns with the predictions of the linear model, as indicated by Equation 2.16. However, in the designed test rig, the effects of damping are not considered. Conversely, when the Equation 4.10 is investigated, the gyrostabilizer damping torque is stated as $\tau_G = \dot{\theta}_2\dot{\theta}_3 J_{3_{11}}$, while the

sea disturbance is stated as $\tau_\omega = M_{011}^r$. For the time being, it is sufficient to eliminate the gyroscopic effect and obtain the ship dynamics by simplifying the terms as following Equation 4.11, 4.12, 4.13 and 4.14.

$$I_{44} = (m_3 + m_2)r_{11}^2 + m_1 g_{11}^2 \ + J_{1_{11}} + J_{3_{11}} + J_{2_{11}} \tag{4.11}$$

$$B_{44} = 0 \tag{4.12}$$

$$C_{44} = g[(m_2 + m_3)r_{11} + m_1 g_{11}] \tag{4.13}$$

$$L = \dot{\theta}_3 J_{3_{11}} \tag{4.14}$$

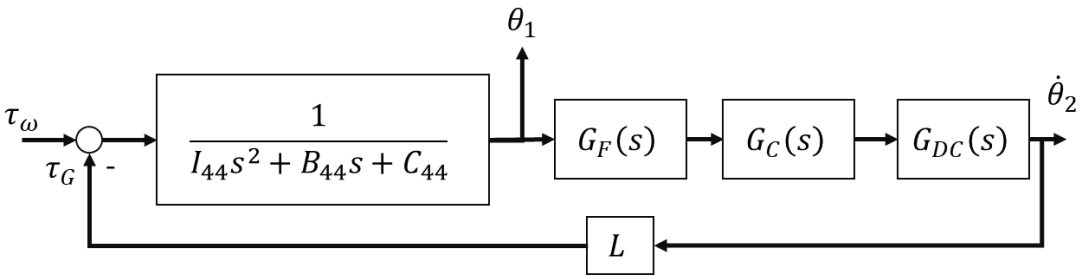

Figure 4.5 Ship and gyrostabilizer system block diagram

Figure 4.5 shows the block diagram of the control system of the ship and gyrostabilizer. The functions $G_F(s)$, $G_C(s)$ and $G_{DC}(s)$ indicate the dynamics of the sensor feedback, control system and dynamics of the actuator system respectively. The closed loop transfer function of the system between sea disturbance and ship roll motion is expressed as given Equation 4.15.

$$\frac{\theta_1(s)}{\tau_\omega} = \frac{1}{I_{44}s^2 + B_{44}s + C_{44} + G_F(s)G_C(s)G_{DC}(s)L} \tag{4.15}$$

In order to design a control system, several assumptions can be made. One such assumption is that the dynamics of the filter and actuator system are equal to one. The control system can then be designed. The objective of the control system is to minimize the ship's roll motion and precession angle. For this reason, it is necessary to combine two types of controllers.

As mentioned in the sensor feedback section, the roll rate can be quantified and the roll angle can be calculated by using a complementary filter. In addition, the precession angle can be measured directly from the system's encoder. Consequently, these three parameters need to be fed into the control system.

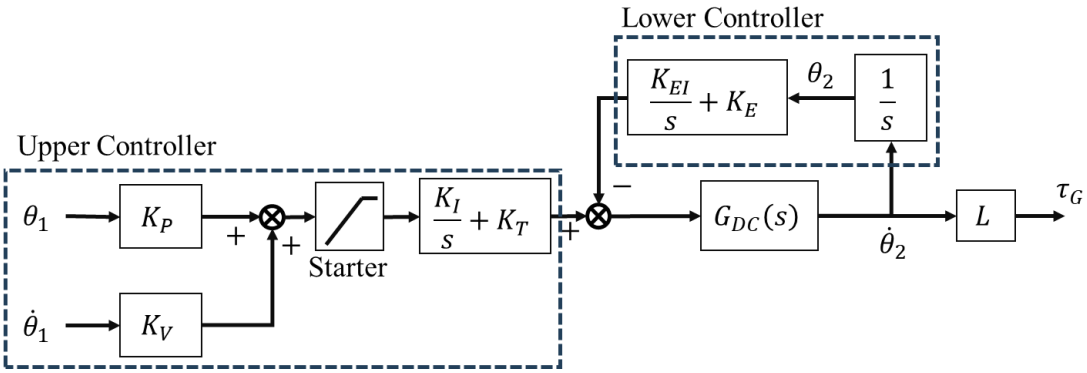

Figure 4.6. PV-PI control system block diagram

Figure 4.6 illustrates the block diagram of the PV-PI control system. The control system is divided into two groups, designated as the upper and lower controllers. The principal objective of the upper controller is to minimize the roll angle and roll rate of the ship. Conversely, the principal objective of the lower controller is to regulate the precession motion range by preventing the drift of the enclosure. The PI section $\left(\frac{K_I}{s} + K_T\right)$of the upper controller is designed for filtering the generated control signal in order to minimise the effect of vibrations on the system. Conversely, the integral and proportional terms in the lower controller are similarly tasked. Additionally, the integral action (K_{EI}/s) is designed to adjust the average precession motion over time.

The most crucial aspect of the PV-PI controller is the starter section. As previously stated, there is a restricted range for precession motion. The initiation of the controller with a step input violates the enclosure motion range. Consequently, a ramp signal is employed to adjust the PV control signal over time. The initial value is lower than the final value, which is reached at the end of the specified time. In this thesis, the ramp time is defined as 30 seconds. Consequently, the actual signal is reached 30 seconds after the start command. The transfer function of the controller is expressed in Equation 4.16.

$$\frac{\dot{\theta}_2(s)}{\theta_1(s)} = \frac{K_T K_V s^2 + (K_T K_P + K_I K_V)s + K_I K_P}{s^2} \frac{s^2 G_{DC}(s)}{s^2 + K_E G_{DC}(s)s + K_{EI} G_{DC}(s)} \quad (4.16)$$

When the controller transfer function and the ship system combined by neglecting the DC motor and feedback systems, the transfer function between wave disturbance and ship motion is written as in Equation 4.17.

$$\frac{\theta_1(s)}{\tau_\omega} = \frac{s^2 + K_E s + K_{EI}}{a_4 s^4 + a_3 s^3 + a_2 s^2 + a_1 s + a_0} \tag{4.17}$$

Where the parameters a_4,a_3,a_2,$a_1$and a_0 are given below.

$$a_4 = I_{44} \tag{4.18}$$

$$a_3 = I_{44} K_E + B_{44} \tag{4.19}$$

$$a_2 = I_{44} K_{EI} + B_{44} K_E + C_{44} + L K_T K_V \tag{4.20}$$

$$a_1 = B_{44} K_{EI} + C K_E + L K_T K_P + L K_V K_I \tag{4.21}$$

$$a_0 = C K_{EI} + L K_P K_I \tag{4.22}$$

In summary, the PV-PI control system has 2 different control targets and 7 parameters. Although it provides high performance in damping roll motion, its adaptability to different gyrostabilizer systems can be problematic. For this reason, a much simpler control system design is presented in the following section.

4.4. Design of the LQR Control System

Full-state feedback control stands as a resilient methodology prominently employed within control systems to attain the desired level of performance and stability. This method revolves around crafting a controller that is endowed with the ability to access and utilize all the states of the system for feedback purposes. Numerous scholarly investigations have underscored the advantages and diverse applications that stem from the employment of full-state feedback control. This approach is revered for its capacity to offer heightened robustness and efficiency in regulating complex systems across various domains, ranging from aerospace and automotive engineering to industrial

automation and beyond. By leveraging a comprehensive understanding of the system's internal dynamics, full-state feedback control empowers engineers to fine-tune and optimize system behavior with precision, ensuring superior performance and resilience against disturbances (Dorf and Bishop,2018).

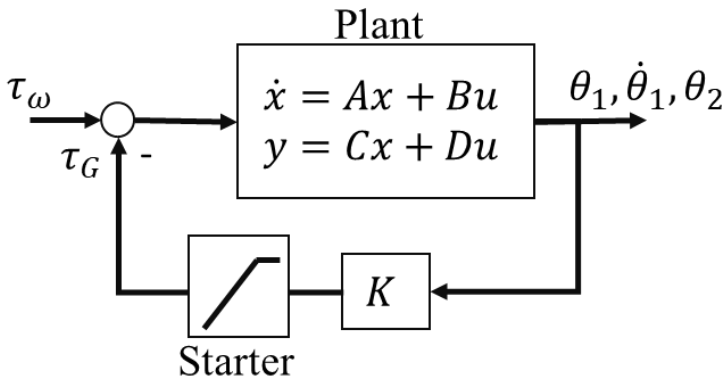

Figure 4.7. Full state feedback block diagram

The full-state feedback control system represents a straightforward methodology for the design of a control system. Firstly, the state-space parameters must be defined. In the context of a gyrostabilizer and ship system, the state parameters are defined as roll angle, roll rate and precession angle. The state space equation is written using the simplified version of Equation 4.10.

$$\ddot{\theta}_1 = \frac{\tau_\omega}{I_{44}} - \frac{B_{44}}{I_{44}}\dot{\theta}_1 - \frac{C_{44}}{I_{44}}\theta_1 - \frac{L}{I_{44}}\dot{\theta}_2 \tag{4.23}$$

The simplified equation of motion is expressed in state space form is written as Equation 4.24.

$$\dot{x} = \hat{A}x + \hat{B}u + \hat{B}'u' \tag{4.24}$$

The Equation 4.24 represents the state space representation of the system. The state matrix, $\hat{A}$, represents the state of the system, while the control matrix, $\hat{B}$, represents the control inputs. The state vector, x, represents the state of the system, and the control vector, u, represents the control inputs. The additional $\hat{B}'u'$ term indicates the wave disturbance term.

$$\begin{bmatrix} \dot{\theta}_1 \\ \ddot{\theta}_2 \\ \dot{\theta}_2 \end{bmatrix} = \begin{bmatrix} 0 & 1 & 0 \\ -\frac{C_{44}}{I_{44}} & -\frac{B_{44}}{I_{44}} & 0 \\ 0 & 0 & 0 \end{bmatrix} \begin{bmatrix} \theta_1 \\ \dot{\theta}_1 \\ \theta_2 \end{bmatrix} + \begin{bmatrix} 0 \\ -\frac{L}{I_{44}} \\ 1 \end{bmatrix} \dot{\theta}_2 + \begin{bmatrix} 0 \\ \frac{1}{I_{44}} \\ 0 \end{bmatrix} \tau_\omega \tag{4.25}$$

Once the state space representation of the system has been defined, it is necessary to investigate the controllability of the system. Upon completion of the aforementioned analyses, it was determined that the system in question, with the specified parameters, is uncontrollable. This is because the damping term, B_{44}, is assumed to be zero in analytical calculations. However, following the system identification tests in Chapter 5, it is accepted that $B_{44} = 1.41$. From this point onwards, the system is deemed to be controllable. It is now necessary to identify the control matrix, K.

The control matrix K is determined by employing the Linear Quadratic Regulator (LQR) approach. The LQR control strategy facilitates the determination of the control matrix through the use of penalty and effort matrices, namely Q and R.

The penalty matrix is a diagonal matrix, with each element corresponding to a state. By assigning a numerical value to each element, the system's sensitivity to that parameter is quantified. A high value indicates that the corresponding state control is of greater importance than the others. Conversely, the effort matrix modifies the responses of the actuators. It is possible that a high number of actuated systems may be crucial. Nevertheless, the present thesis concerns a single actuator. Consequently, the effort matrix is a constant number.

Equation 4.26 is solved once the penalty, effort and state matrices have been defined using the Algebraic Riccati Equation (ARE) (Dorf and Bishop,2018). The objective of solving the ARE is to determine the value of P, which defines the gains of the K matrix. After determination of the P, the control matrix parameters are found as in Equation 4.27.

$$\hat{A}^T\hat{P} + \hat{P}\hat{A} + \hat{Q} - \hat{P}B\hat{R}^{-1}\hat{B}^T\hat{P} = 0 \tag{4.26}$$

$$\hat{K} = \hat{R}^{-1}\hat{B}^T\hat{P} \tag{4.27}$$

Finally, the control gain can be implemented in the controller. The LQR control system has 4 parameters to tune. For this reason, it is easier to implement than the PV-PI

control system. It is also easier to adapt to different gyrostabilizer-ship combinations because of the parametric equations.

4.5. Conclusion of the Control System Design

This section introduces the basic principles of gyrostabilizer control system design. This section discusses the feedback, actuator, plant and controller parts of a control system. Two controller designs are presented: LQR and PV-PI. At first glance, the PV-PI system appears to have an excessive number of adjustable parameters. This may be a disadvantage in the tuning process of the gyrostabilizer. Conversely, the design and implementation of the LQR system is a relatively straightforward procedure.

Figure 4.8 shows a comparative study of the controllers in question. The initial state of the ship is adjusted by 20˚. The states of the system (roll angle and precession angle) are then examined when the ship is suddenly dropped. The figure shows that the LQR controller performs better in terms of roll damping. Nevertheless, the precession angle reaches zero faster with the PV-PI control than with the LQR control. This is also an important point for the control system. The controller parameters used in Figure 4.8 are taken from the best controller parameters obtained in Section 6.

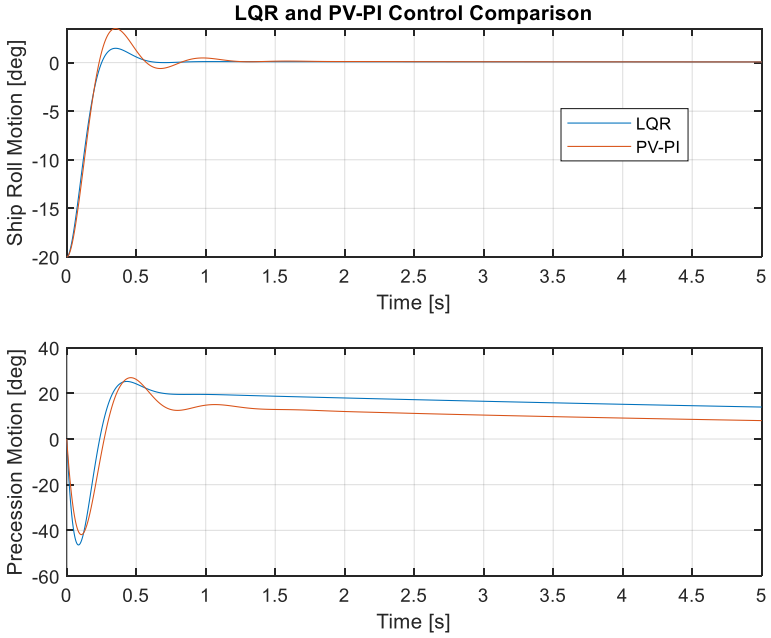

Figure 4.8. Free decay comparison of the LQR and PV-PI control systems $K = [64.38 \quad 8.89 \quad 0.4082]$, $K_P = 9$, $K_V = 1$, $K_T = 5$, $K_I = 15$, $K_E = 0.1$, $K_{EI} = 1$

CHAPTER 5

PROTOTYPING THE SCALED-DOWN GYROSTABILIZER

This section introduces the experimental test system, including the specifications of the DC motors, data acquisition system and sensory feedback system. The test procedure starts with the system identification test to define the differences between the designed and manufactured system. The responses of the actuation and feedback systems are also examined to determine their performance. Finally, this section concludes with a comparison of the experimental and theoretical control systems.

5.1. Introduction of Test Rig Components

The gyrostabilizer test system consists of 3 main parts; (1) the flywheel, (2) the enclosure and (3) the ship. The flywheel has a large mass moment of inertia about its axis of rotation. Rotation is provided by the Maxon EC45. This is a frameless BLDC motor capable of delivering high torque at high speeds. The motor driver used in this BLDC motor is the Escon 50/5, which has built-in closed-loop control. Therefore, the target speed can be achieved by the motor driver. An incremental encoder (Fenac FNC50H) is used for the feedback system.

The second important part of the test system is the enclosure. It provides the precession motion for the flywheel to generate the control torque. A DC motor (Maxon RE30) is used to move the enclosure. This system requires more torque than the flywheel system. For this reason, a gearbox is used in this system. The Maxon GP32-C was chosen, which has a reduction ratio of 159:1. Similar to the previous system, the motor controller is an Escon 50/5 and there is an incremental encoder called Maxon HEDL 5540. This motor subsystem also has integrated speed control.

The third system is called the ship system. It mimics the 1-DoF rolling motion of sea vessels. This system has a BLDC motor to generate the disturbance torque to imitate the sea state. This BLDC motor is called the wave imitation motor. The motor used is Maxon 90EC. This system requires a high amount of torque similar to the enclosure

system. However, this system uses a capstan drive instead of a traditional gear. The main reason for this choice is to minimize the inertia effect of the gearbox and to improve the backdrivability the ship around its axis of rotation. Backdrivability is a crucial feature because system will damp its motion. The capstan drive system designed has a reduction ratio of 8:1.

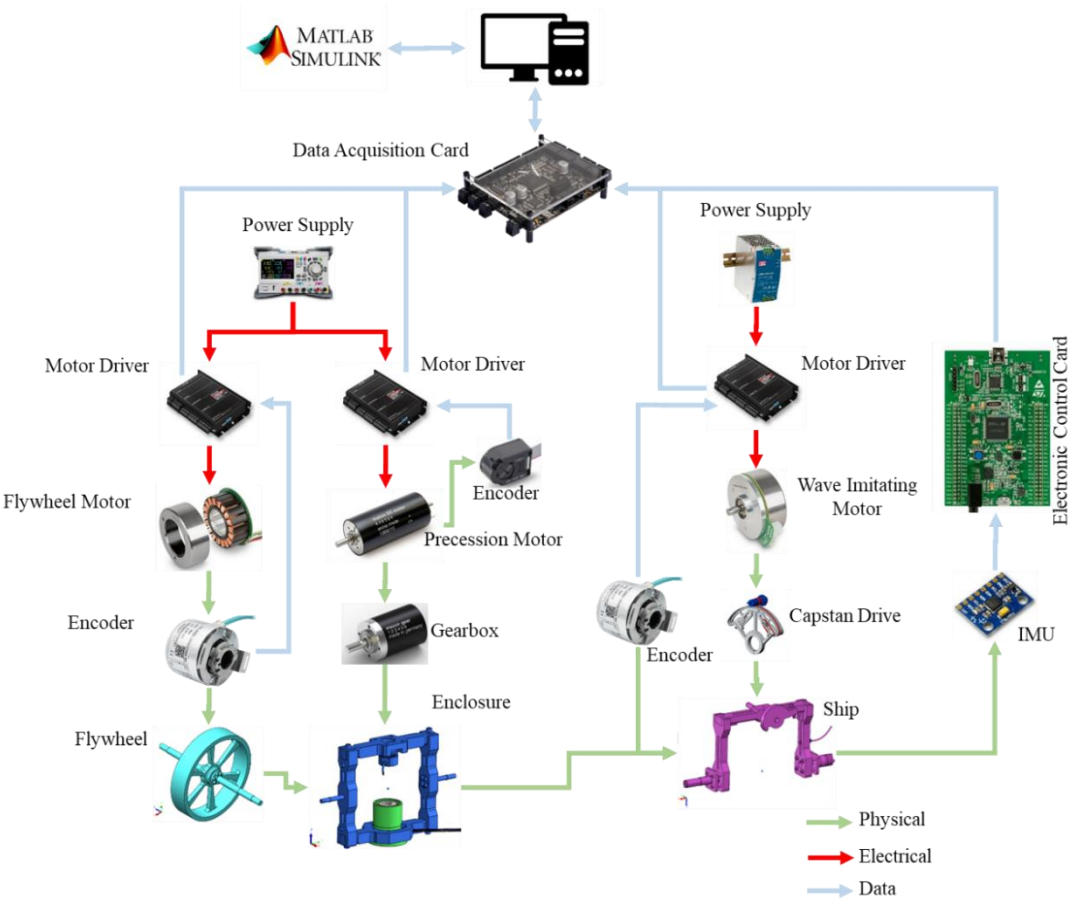

Figure 5.1. The general connection table of the gyrostabilizer test system

The aim for the wave imitating motor controller is to generate the torques acting on the ship due to the wave disturbance by supplying currents that are calculated with respect to the sea state condition to the motor. The motor driver Escon 70/10 is capable of current drive mode. Since this wave imitating motor control system is designed to be an open-loop controller, there is no need for sensory feedback. However, for the wave imitating motor control of the body-state control and for monitoring the motion of the ship, a motion sensor is required. In a sea vessel, there is no way to measure the ship's motion using an encoder since the sea vessel is not mounted on Earth. Therefore, in this test system, an MPU6050 IMU is used for providing motion feedback. Nevertheless, an

incremental encoder (Fenac FNC50H) is included in the test system to measure the ship's motion. The reason for using an encoder is to measure the ship's motion to verify the data that would have been received from an inertial measurement unit (IMU) in an actual ship. The obtained ship motion data is converted into an analogue signal using the STM32F407VG Discovery Board. Then the corresponding data is fed into the data acquisition card called V-Daq.

The flow of information through the test system is shown in Figure 5.1. The green arrows show the physical connection, the red arrows show the electrical connection and the blue arrows show the information flow through the test system. SIMULINK 2020A is used for control and data monitoring via HP Pavilion.

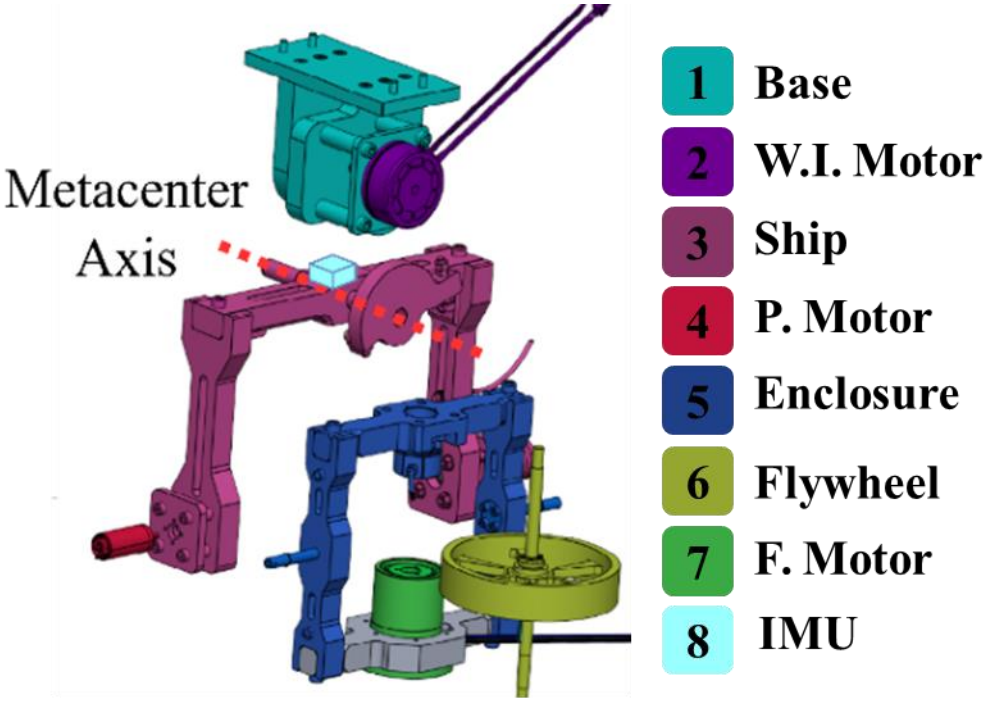

Figure 5.2. (a) Colored CAD Design and (b) Manufactured gyrostabilizer test stand

Figure 5.2 shows the colored CAD design of the gyrostabilizer. The metacenter axis is also shown in the colored section with a red dashed line and the position of the IMU is also shown. The IMU is placed as close as possible to the metacentric axis (ship's axis of rotation) to minimize the effect of acceleration due to the rotational motion of the ship.

Figure 5.3 shows the manufactured gyrostabilizer with indicator arrows. Arrows shows the respective gyrostabilizer components such as wave imitating motor (W.I. Motor), precession motor (P. Motor), flywheel motor (F. Motor) and etc. Also, blue

arrows indicate the size of the gyrostabilizer 400 [mm] wide and 387.5 [mm] height. The flywheel has 200 [mm] diameter and 40 [mm] thickness. The other dimensions are given in the Appendix C.

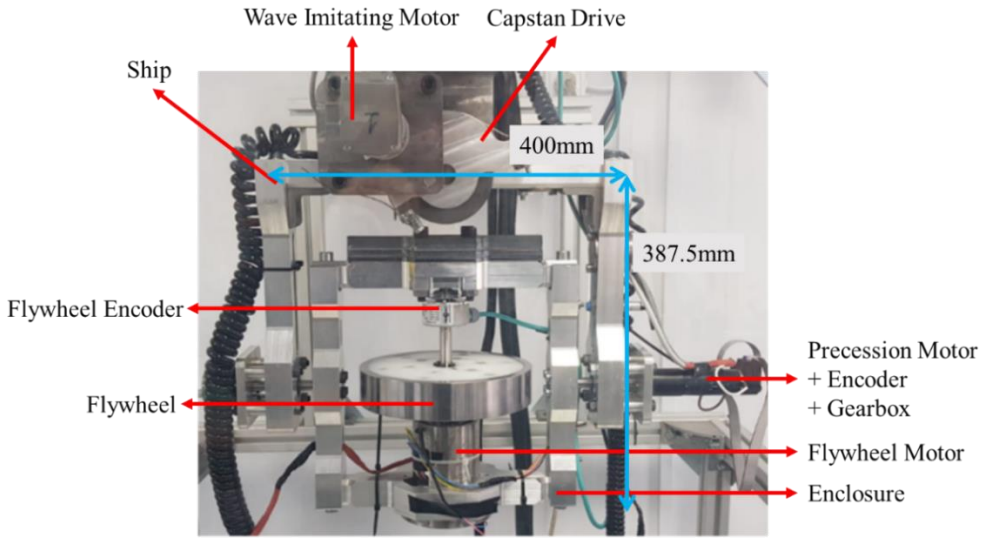

Figure 5.3. Manufactured gyrostabilizer with component names

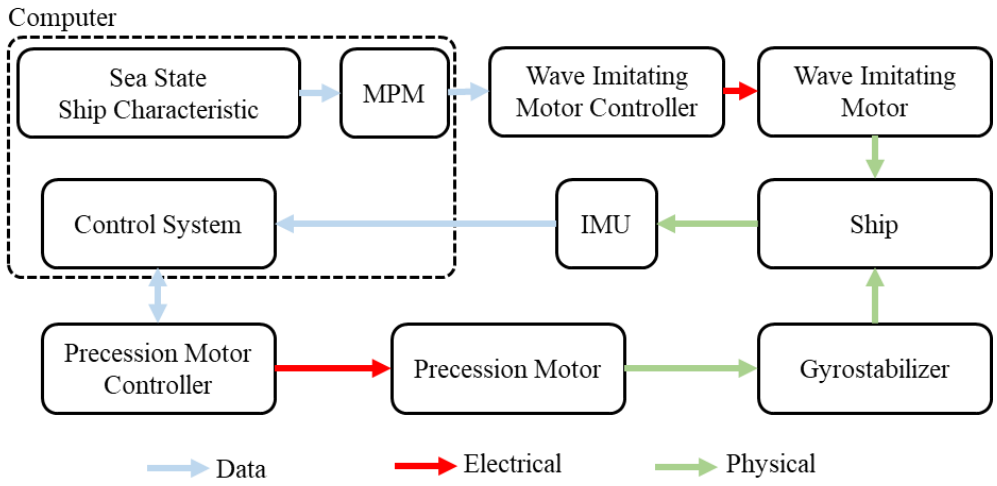

Figure 5.4. The test procedure information flow chart

The test system information flow chart is shown in Figure 5.4. Firstly, the ship characteristics and sea state must be determined for the irregular sea tests. Then an MPM algorithm uses the given data to generate a torque profile for the wave imitating motor. Using the data acquisition card, the profile is fed into the wave imitating motor driver so that the motor generates the disturbance torque on the ship system. Finally, the ship system begins to perform the roll motion. The linear acceleration and roll rate are

measured by the IMU and, using a complementary filter, it generates a roll angle for feedback purposes. The resulting value is fed into the control system to generate a control signal to minimize the roll motion. The output of the control system is fed into the precession motor controller, so that the precession motor generates a precession motion. The result is a control torque to dampen the roll motion of the vessel.

There are always differences and small errors between designed and manufactured systems. These errors may be caused by manufacturing errors or by some variables not included in the design. For example, this test system does not include the weight and inertia of the cables. For this reason, the system identification test is carried out before starting the gyrostabilizer performance tests.

5.2. System Identification Studies

The designed parameters of the system and the actual parameters may differ due to simplifications in the design or manufacturing errors. This type of error can directly affect the control system parameters. For a proper test procedure, these uncertainties should be determined using experimental approaches.

In order to make a comparison between the designed and the real system parameters, three different system identification tests have been carried out. The first test is to generate a transfer function to the ship's roll motion. The second test is to understand the dynamics of the actuation system (enclosure). Finally, the third test is to define a transfer function to the sensory feedback system.

5.2.1. Determination of the Transfer Function of the Simple Pendulum Model

To determine the transfer function of the simple pendulum model, several chirp signals are applied to the vessel using a wave imitating motor. The chirp signal is a commonly used type of signal for system identification testing. It is a simple sinusoidal signal whose frequency increases with time. An example of a 1Nm chirp signal applied is shown in Figure 5.5.

Figure 5.5 shows the generated 1 [N·m] disturbance signal. It is generated with a 1 [N·m] amplitude chirp signal starting at 0.5 [Hz] and increasing linearly to 2 [Hz]. In

order to obtain a correct experimental result, the 8 different experiments are performed. 4 of the experiments are performed for 0˚ enclosure angle and the other 4 are performed for 60˚ enclosure angle. Each of the 4 experiments is performed for different amplitudes such as 1 [N·m], 0.75 [N·m], 0.5 [N·m] and 0.3 [N·m].

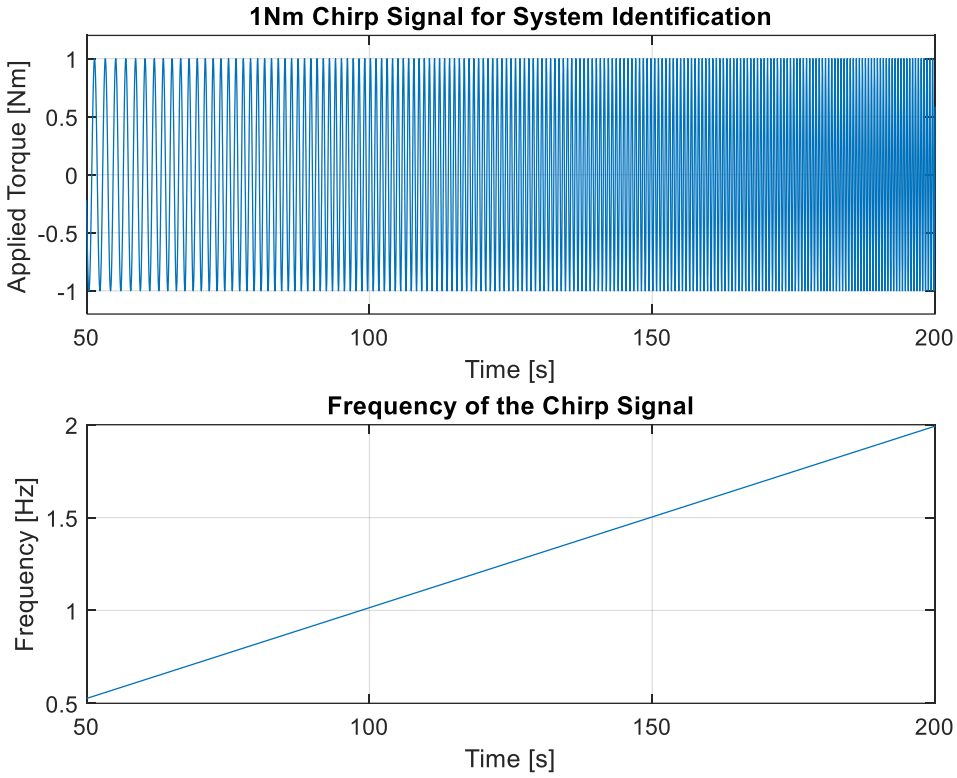

Figure 5.5. Generated chirp signal for pendulum model parameter identification

Figure 5.6 shows the results of the chirp signals. The most striking result is that the system resonates around 87 seconds, which corresponds to 0.8 [Hz]. Furthermore, for lower excitation torques such as 0.3 [N·m], this frequency is pushed a little further from 0.8 [Hz]. Using this input-output relationship, the transfer functions is obtained using the MATLAB System Identification Toolbox.

Table 5.1 shows the estimated transfer functions for the given signal. The experimental results are tabulated as a function of the enclosure angle and the magnitude of the chirp signal applied. The transfer functions are listed as a second order system. The natural frequency of the system is also given in radians per second. Finally, the Fit to Data section shows the error between the actual signal and the signal generated by the transfer functions. A large percentage in the fit to data indicates that the particular transfer function is a good choice for representing the system.

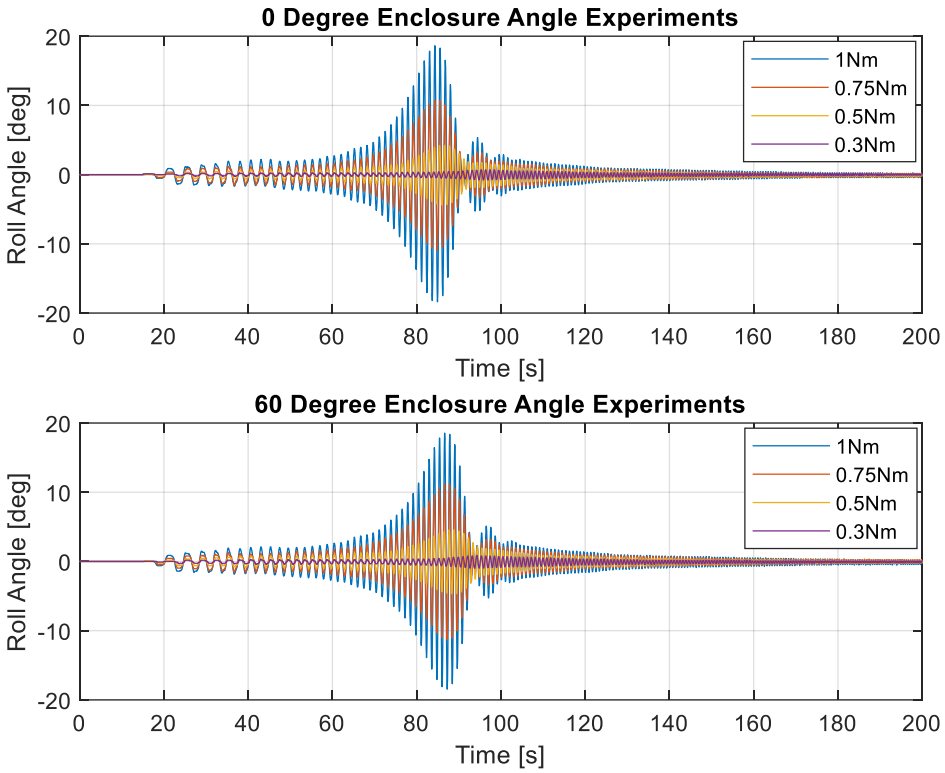

Figure 5.6. Results of the applied chirp signals

When examining the results, it is clear that low torque amplitudes have a low percentage fit to the data. This may be due to the dead zone of the DC motor dynamics or the looseness of the capstan cable. The best data fits are obtained from the two 1 [N·m] chirp signals. The transfer functions are also close each other for the cases with 0 and 60˚.

After completing the system identification studies for simple pendulum model, a linear model is generated using the transfer functions in Table 5.1. The characteristic equation of the linear model is accepted as $G(s) = 1.82s^2 + 1.41s + 48.85$ by taking the weighted average of the available data. A disturbance signal is then generated to force the ship to roll. The signal is fed into the test setup, simulation and linear model transfer function. The simulation file has already been created as described in Section 3. In addition, a linear system model is created using the transfer function block in Simulink. The ship's roll motions are then recorded as shown in Figure 5.7. When Figure 5.7 is examined, it is seen that the experimental results and the linear system model are close to each other. However, the signal obtained from the simulation has overshoots at the peak points. This result shows the effect of the non-designed parts on the 3D model of the system.

Table 5.1. Simple pendulum model system identification results

Enclosure Angle	Torque Amplitude	Transfer Function	Natural Frequency	Fit to Data
0°	0.3 Nm	$\frac{1}{2.09s^2 + 5.22s + 78.67}$	6.13 rad/s	60.18%
	0.5 Nm	$\frac{1}{2.13s^2 + 1.52s + 55.75}$	5.10 rad/s	65.34%
	0.75 Nm	$\frac{1}{1.90s^2 + 0.74s + 46.7}$	4.95 rad/s	77.89%
	1.00 Nm	$\frac{1}{1.74s^2 + 0.53s + 42.10}$	4.90 rad/s	82.81%
60°	0.3 Nm	$\frac{1}{1.84s^2 + 4.34s + 66.34}$	6 rad/s	54.50%
	0.5 Nm	$\frac{1}{1.75s^2 + 1.33s + 48.30}$	5.24 rad/s	79.10%
	0.75 Nm	$\frac{1}{1.71s^2 + 0.70s + 44.73}$	5.10 rad/s	78.46%
	1.00 Nm	$\frac{1}{1.61s^2 + 0.52s + 41.41}$	5.06 rad/s	83.03%
Theoretic		$\frac{1}{1.78s^2 + 34.01}$	4.36 rad/s	#

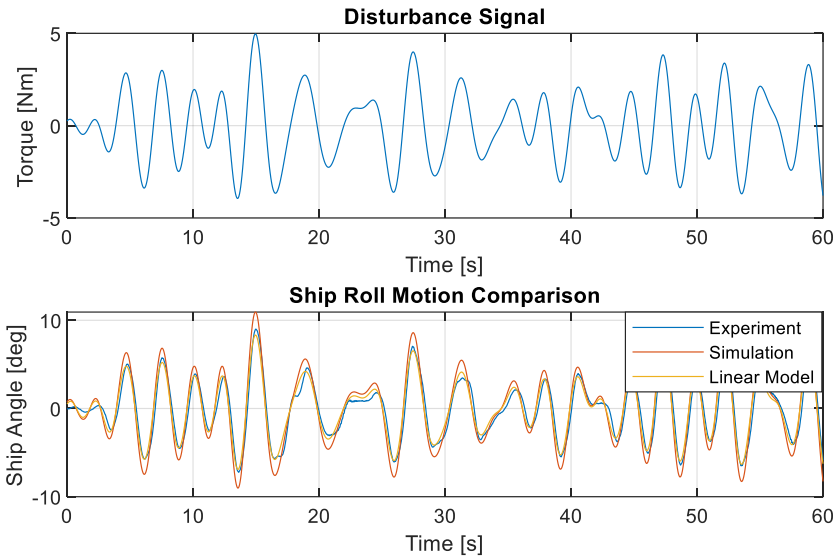

Figure 5.7. Experimental, simulation and linear model comparison of the ship dynamics

5.2.2. Determination of the Transfer Function of the Actuation System

The drive system consists of the DC motor and the enclosure system. The reduction ratio of the DC motor and the output shaft is 159:1. Therefore, the effect of the mass moment of inertia of both the enclosure and the flywheel on the motor reduces by the square of the reduction ratio. Therefore, this effect is foreseen to be negligible. The DC motor is modelled as a first order system using the time constant value. In the motor catalogue the time constant of the RE30 is given as 3.4 milliseconds.

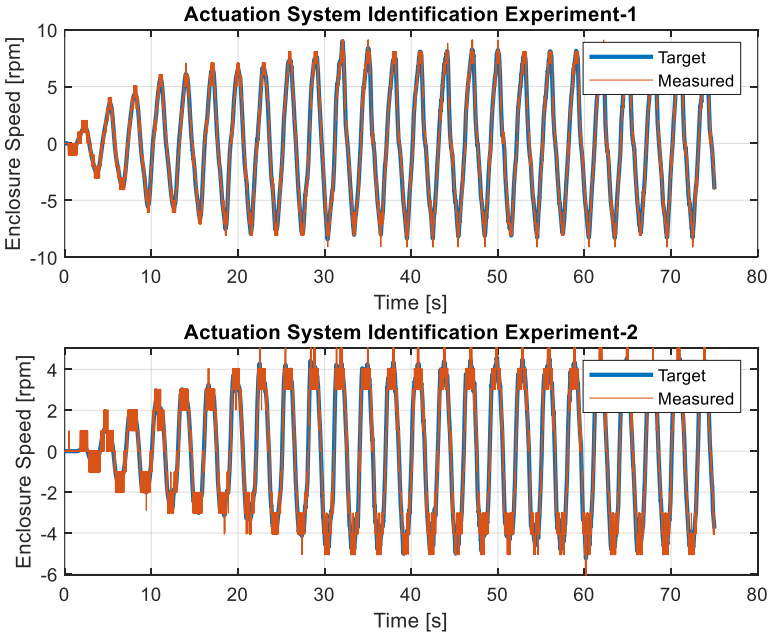

Figure 5.8. Actuation system identification experiments

Figure 5.8 shows the results of the actuator system experiment. Two recorded signals are used to determine the first order transfer function of the system. Each of the plots has two values, the target and the measured. The target is the control system applied to the cabinet motor. The measured signal is the responsive rotation of the enclosure system. Using the MATLAB System Identification Toolbox, the first order transfer function of the system is obtained as in Table 5.2.

Table 5.2. Transfer functions for actuation system

	Transfer Function	Fit to Data
Experiment – 1	$\frac{1}{0.013s + 1.005}$	91.47%
Experiment - 2	$\frac{1}{0.014s + 1.005}$	86.4%
Theoretical	$\frac{1}{0.0034s + 1}$	#

The transfer functions obtained are listed in Table 5.2. The experimental results are close to each other with an accuracy of 91.47% and 86.4%. However, when comparing the experimental and theoretical transfer functions, there is a difference of 4.1 times. The reason for this difference may be due to the neglected gear inertia and/or its friction. Although the inertia of the case and the flywheel are too small, in these tests the flywheel has a speed of 1000 [rpm]. The reaction torque of the gyrostabilizer can therefore cause a difference between theoretical and experimental results. Overall, it can still be ignored when designing the control system.

5.2.3. Determination of the Transfer Function of the Feedback System

A similar methodology to that used for the simple pendulum model and actuator system is used for the feedback system. The recorded experiment value is shown in Figure 5.9. Here the input is defined as the encoder data (encoder connected to the metacentric axis) while the output is the IMU data. There is no theoretically calculated transfer function for the feedback system. If the transfer function obtained indicates that the sensory feedback system has a high response time, i.e. a low input/output delay, then its dynamics are neglected as well as the dynamics of the drive system.

Table 5.3. Transfer function for the feedback system

Transfer Function	Fit to Data
$\frac{1}{0.0001s + 0.91}$	91.16%

5.3. Theoretical and Experimental PV-PI Control System Comparison

After completing the system identification procedure, the obtained results were implemented in the transfer function of the designed PV-PI control system. As a reminder, the proposed PV-PI control system consists of seven parameters, including the flywheel precession speed. Therefore, defining the control parameters is a challenging task. When defining the control parameters, the Simulink file created is used first. Then the parameters are fine-tuned as described in Section 6. Finally, the best PV-PI parameters are set as shown in Table 5.4. The Bode and root locus diagrams for the theoretical and experimental test system are then presented using these control system parameters. By utilizing the aforementioned control parameters, it is possible to generate a root locus and bode diagram for the system at a flywheel speed of 1000 [rpm]. In order to facilitate a comparison between the design and experimental parameters, two root locus diagrams are drawn

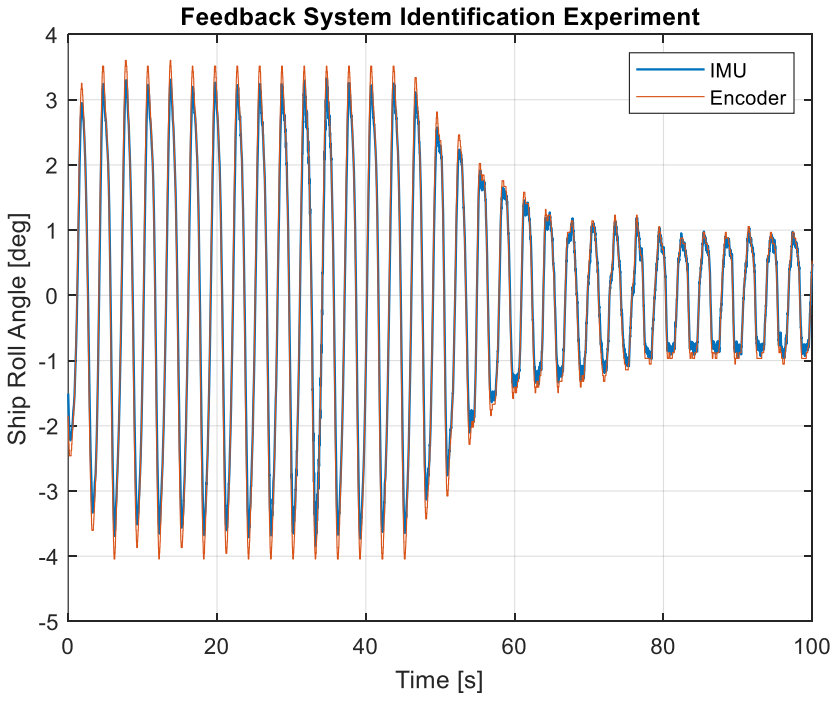

Figure 5.9. System identification experiment for feedback system

Table 5.4. PV-PI control system parameters

K_P	9
K_V	1
K_T	7
K_I	15
K_E	0.01
K_{EI}	1

.

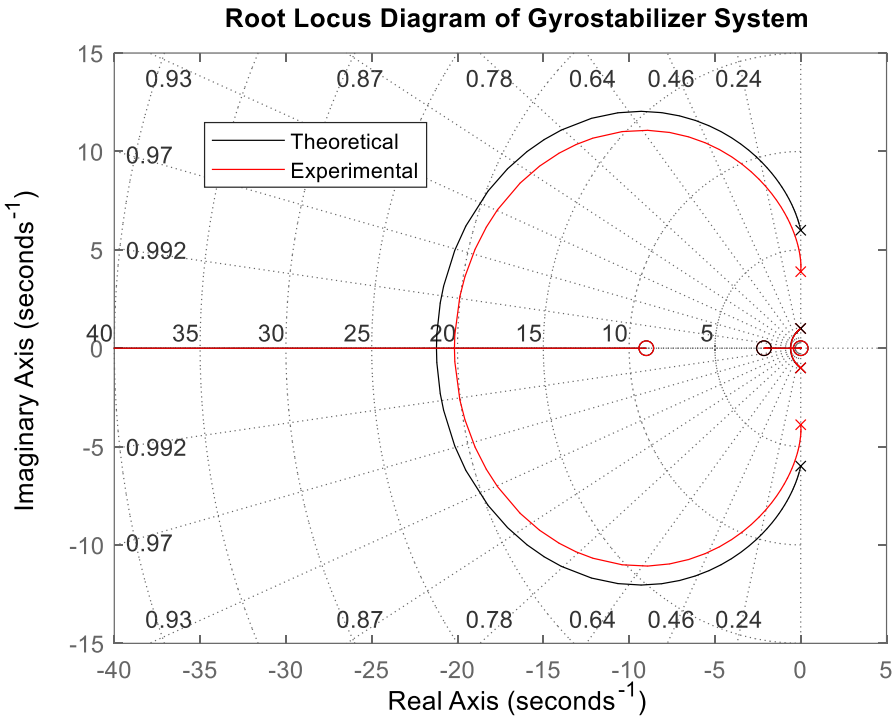

Figure 5.10. Theoretical and experimental root locus diagram of the gyrostabilizer system

Table 5.5. Theoretical and experimental ship parameters

	Theoretical	Experimental
I_{44}	0.8615	1.82
B_{44}	0	1.41
C_{44}	30.94	48.85

A root locus diagram is constructed using the values from Tables 5.4 and 5.5, representing both theoretical and experimentally obtained system constants. The results show that the designed PV-PI control system, with the gains specified in Table 4.4, is stable for all flywheel speeds, as shown in Figure 5.10.

Figure 5.11 shows the Bode diagram of the open and closed loop transfer function of the gyrostabilizer system. The open-loop signal represents the rolling motion of the vessel in the absence of a gyrostabilizer. Conversely, the closed-loop signals represent the vessel system with the gyrostabilizer fitted. The magnitude plot shows that there is a significant reduction in motion around 1 [rad/s]. The desired reduction in roll motion is therefore achieved. As mentioned earlier, it is important to prevent the roll motion between 0.2-0.5 [Hz], which corresponds to the 1.25-3.12 [rad/s] range. The bode diagram in Figure 5.10 shows that with the PV-PI control system and the gyrostabilizer, the ship's roll motion has been reduced as desired.

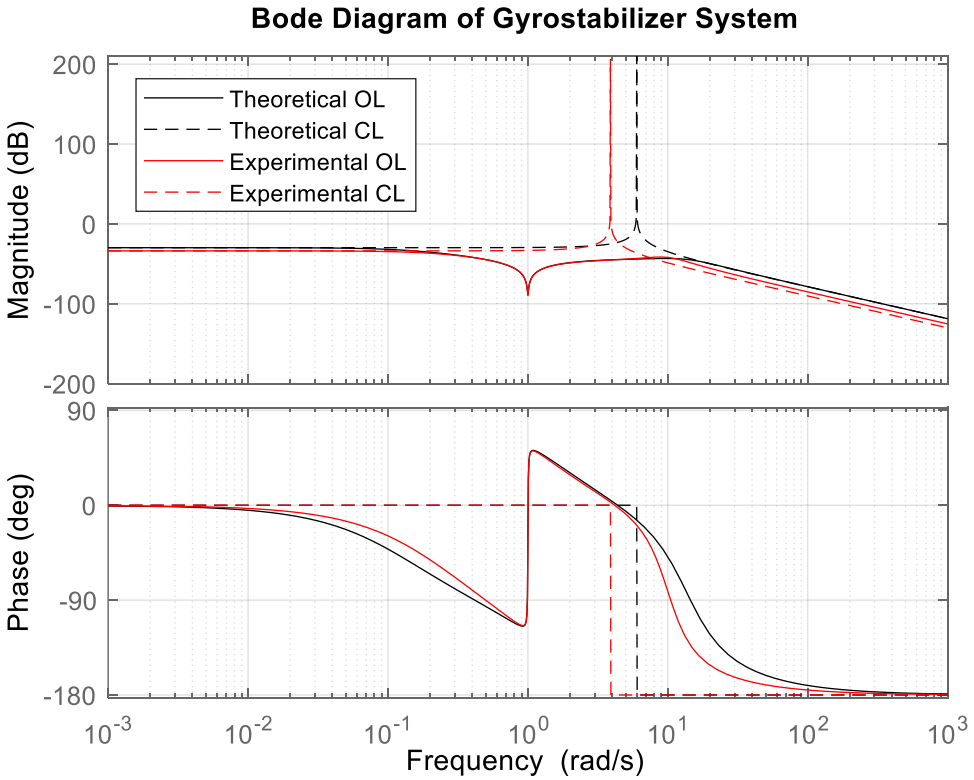

Figure 5.11. Theoretical and experimental open loop (OL) / closed loop (CL) transfer function

5.4. Conclusion of the Prototyping the Scaled-Down Gyrostabilizer

In this section the components of the test system used in the scaled down gyrostabilizer have been presented. There are 3 different electric motors used for different tasks such as imitating the wave disturbances, rotating the flywheel and finally controlling the precession motion during operation. Each of the motors placed the corresponding axis to perform its tasks.

After the introduction of the test system components, the system identification experiments are carried out. These experiments are carried out to investigate the differences between the designed and manufactured system. The identification experiments show that, the effect of sensory feedback and enclosure system actuator is minimized. On the other hand, they can perform their missions in the best possible way. However, the theoretical ship transfer function is not similar to the experimental value. This may be caused by the manufacturing errors or other undesigned things such as cables, sensors, etc.

In conclusion, using the results obtained from the system identification test, the bode and root locus diagrams of the PV-PI control system are examined. The results show that, although they have differences, they can manage the damping of the roll motion.

CHAPTER 6

PERFORMANCE TEST OF THE GYROSTABILIZER

This section presents the performance test of the designed PV-PI and LQR control systems. The results of the control system tests are investigated in three different sections as 6.1. PV-PI control system performance, 6.2. LQR control system performance and 6.3. Comparison of PV-PI and LQR control system performance. In sections 6.1. and 6.2. the experimental results are compared with the simulation results and experiments with different flywheel speeds are carried out. Finally, the performance of the PV-PI and LQR control systems is compared in section 6.3.

A disturbance signal is used to obtain comparable results. In order to see the effect on the variation of the noise signal, a multiplier called the Disturbance Gain Multiplier (TM) is used. First, the wave disturbance signal is recorded using the Pierson-Moskowitz approach. The values are taken as follows; The mean sea level is assumed to be $H = 0.5\ [m]$, the average wave period is $T = 4\ [s]$, the ship mass is $H = 17\ [kg]$ and the metacentric height is $GM_T = 0.15\ [m]$.

6.1. PV-PI Control System Performance

The PV-PI control system consists of seven parameters related to the flywheel speed. Consequently, the tuning process of this control system is challenging and not straightforward. First, the parameters are intuitively defined. Then, using the generated Simulink folder, simulations are carried out, resulting in parameter changes. Finally, the system is fine-tuned on a test rig. The results of the test rig tuning are listed in Table 6.1.

After fine-tuning on the test bench, several tests are carried out. Figure 6.1 compares the PV-PI control system with the results obtained in Simulink. As seen in the figure, operation starts after 40 seconds. After that, the control system reaches its full capacity in 30 seconds.

The first plot shows the roll angle (θ_1) of the ship, while the second plot shows the precession angle (θ_2). The results show that there is very little difference between experiment and simulation in the roll angle. On the other hand, the precession angle is

drifted at 80 and 160 seconds. After that, however, the difference between experimental and simulation results closes.

Table 6.1. Fine tuning process of the PV-PI control system

Exp. Num.	K_P	K_V	K_T	K_I	K_E	K_{EI}	Comment
1	10	1	5	5	0.01	1	Enclosure angle drift
2	10	1	5	10	0.01	1	Enclosure angle drift
3	10	1	5	25	0.01	1	Enclosure angle reach limits
4	15	1	5	15	0.01	1	Good performance, increased vibrations
5	20	1	5	15	0.01	1	Better performance than #4, more increase vibrations
6	15	1	7	15	0.01	1	Unstable
7	9	1	5	15	0.01	1	Stable system, less vibration than #5
8	9	1	5	15	0.1	1	Worse performance than #7

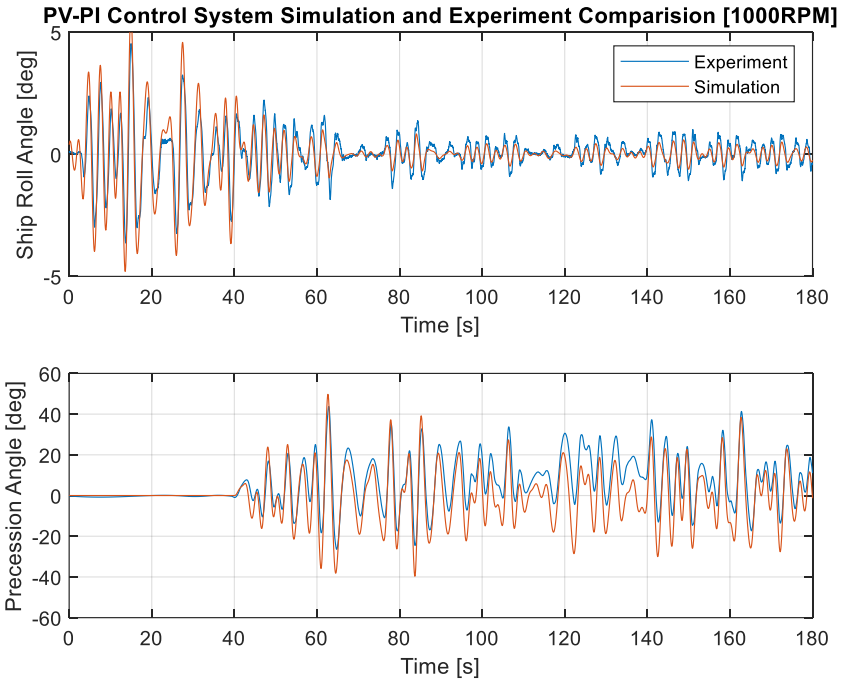

Figure 6.1. PV-PI control system simulation and experimental comparison at 1000 rpm flywheel speed ($T_M = 1, \dot{\theta}_3 = 1000\ [rpm], K_P = 9, K_V = 1, K_T = 5, K_I = 15, K_E = 0.1, K_{EI} = 1$)

In this test, the disturbance signal gain is $T_M = 1$, the flywheel speed is $\dot{\theta}_3 = 1000$ [rpm] and control parameters are $K_P = 9$, $K_V = 1$, $K_T = 5$, $K_I = 15$, $K_E = 0.1$, $K_{EI} = 1$.

Figure 6.2 below shows the results of the PV-PI control system for 2000 [rpm] flywheel speed. The same control parameters are used in this system. However, the disturbance system is 1.5 times larger than in Figure 6.1. In this test the control system starts to operate at about 70 seconds. There is a difference between the experimental and simulation results at about 80 seconds for the ship's roll angle. However, after reaching the full operating state, the results are close.

In this test, the disturbance signal gain is $T_M = 1.5$, the flywheel speed is $\dot{\theta}_3 = 1000$ [rpm] and control parameters are $K_P = 9$, $K_V = 1$, $K_T = 5$, $K_I = 15$, $K_E = 0.1$, $K_{EI} = 1$.

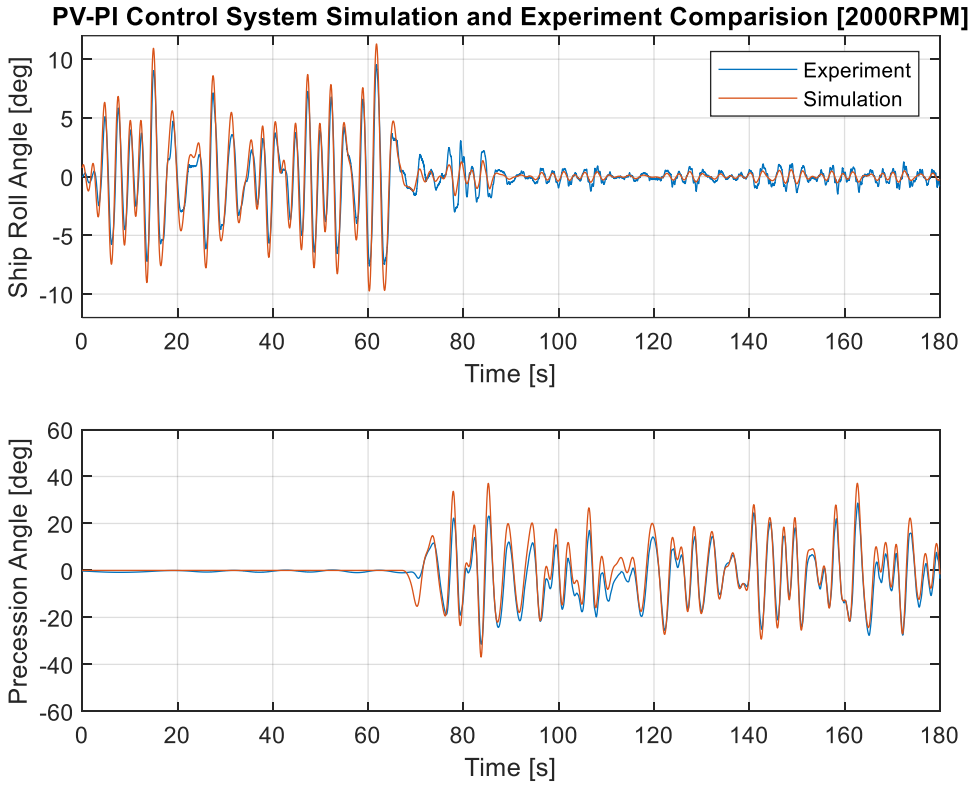

Figure 6.2. PV-PI control system simulation and experimental comparison at 2000 rpm flywheel speed ($T_M = 1.5, \dot{\theta}_3 = 2000\ [rpm],\ K_P = 8.9,\ K_V = 1,\ K_T = 5,\ K_I = 15, K_E = 0.1, K_{EI} = 1$)

Table 6.2 shows the Root Mean Square (RMS) and maximum values (MAX) for ship roll angle (θ_1) and precession angle (θ_2) for both experimental and simulation results.

The data for 1000RPM flywheel speed is taken for 70 and 180 second because the system is in full operation state. On the other hand, the data is taken for 100 and 180 seconds for 2000RPM flywheel speed. Results shows that, Experimental and simulation results are 2 times different than each other for ship roll angle RMS and maximum values. However, the results are close to each other for precession angle values.

Table 6.2. PV-PI control system simulation and experimental results comparison for Root Mean Square of ship roll angle ($\theta_1\ RMS$), precession angle ($\theta_2\ RMS$) and maximum value for ship ($\theta_1\ MAX$) and precession angle ($\theta_2\ MAX$)

	$\dot{\theta}_3$	θ_1 RMS [˚]	$\lvert\theta_1\rvert$ MAX [˚]	θ_2 RMS [˚]	$\lvert\theta_2\rvert$ MAX [˚]
Operation State (70-180)	Simulation 1000 RPM	0.2385	0.8349	14.0084	39.6990
Operation State (70-180)	Experimental 1000 RPM	0.4436	1.4050	15.1451	41.3289
Operation State (100-180)	Simulation 2000 RPM	0.2430	0.6071	13.3477	37.1177
Operation State (100-180)	Experimental 2000 RPM	0.4895	1.4921	11.5565	28.6972

Figure 6.3 shows the PV-PI control system performance results for different flywheel speeds. The disturbance signal gain is taken as 1.25 and control parameters are set to $K_P = 8.9$, $K_V = 1$, $K_T = 5$, $K_I = 15$, $K_E = 0.1$, $K_{EI} = 1$. Due to the operating speed, their operating start time is different from each other. Table 5.6 shows the RMS and maximum values of the results for ship roll angle and precession angle. The RMS value of the ship roll angle shows that increasing the flywheel speed reduces the RMS ship roll angle as expected. However, the precession angle results are not different from the expected values. The main reason for this is the drift of the precession angle. It is possible to minimize the precession angle drift by increasing the relevant gain in the control system.

Table 6.3 shows the comparison of maximum and RMS values between 1000, 1500 and 2000 [rpm]. As expected, the highest roll angle dampening is produced by the 2000 [rpm] test. Also, the results shows that the maximum enclosure angle is created by

2000 [rpm]. The unexpected result is caused by the 1500 [rpm] because of the rms and maximum precession angle occurred in it.

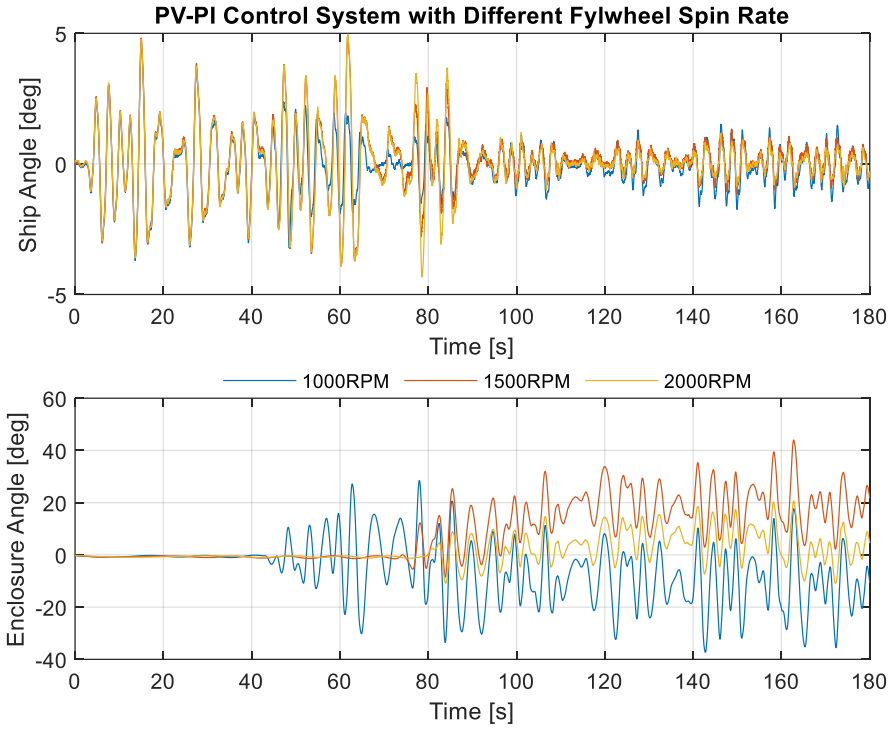

Figure 6.3. PV-PI control system performance results at different flywheel speeds ($T_M = 1.25, K_P = 9, K_V = 1, K_T = 5, K_I = 15, K_E = 0.1, K_{EI} = 1$)

Table 6.3. PV-PI control system 1000 [rpm], 1500 [rpm] and 2000 [rpm] test results RMS and maximum values for ship roll angle and precession angle

	$\dot{\theta}_3$	θ_1 RMS [˚]	$\lvert\theta_1\rvert$ MAX [˚]	θ_2 RMS [˚]	$\lvert\theta_2\rvert$ MAX [˚]
Operation State (70-180)	1000 RPM	0.6106	1.7819	14.9473	37.3024
Operation State (100-180)	1500 RPM	0.4468	1.3090	20.6194	43.9544
Operation State (130-180)	2000 RPM	0.3798	1.1650	8.5356	20.6651

6.2. LQR Control System Performance Comparison

The LQR control system requires a control matrix "K". There are several ways to define the control matrix, such as pole placement, etc. In this thesis, the control

parameters are defined using the Riccati equation as mentioned in section 4. To solve the algebraic Riccati equation it is necessary to determine the matrices "Q" and "R". In our system there is one controlled actuator, so 'R' is a constant. However, in our model there are three states, so 'Q' is a 3x3 diagonal matrix. Each element of the "Q" matrix represents the corresponding state.

It is important to define an optimal "Q" and "R" matrix for the best control results. For this reason, a series of tests are carried out on the test bench to determine the best "Q" matrices for optimum control. The tests are carried out at 1000 [rpm] flywheel speed and the resulting performance data are given in Table 6.4.

Table 6.4. Experimental fine-tuning process results of LQR control system for 1000 [rpm]

Experiment Number	Q Matrix	R Matrix	K Matrix	Comment
1	$\begin{bmatrix}30 & 0 & 0\\ 0 & 10 & 0\\ 0 & 0 & 1\end{bmatrix}$	0.001	$[251.7 \quad 92.2 \quad 31.62]$	Unstable System
2	$\begin{bmatrix}15 & 0 & 0\\ 0 & 5 & 0\\ 0 & 0 & 1\end{bmatrix}$	0.001	$[193.0 \quad 63.15 \quad 31.62]$	Unstable System
3	$\begin{bmatrix}5 & 0 & 0\\ 0 & 1 & 0\\ 0 & 0 & 0.1\end{bmatrix}$	0.001	$[86.63 \quad 29.54 \quad 10]$	Stable, Bad Performance
4	$\begin{bmatrix}5 & 0 & 0\\ 0 & 1 & 0\\ 0 & 0 & 0.0001\end{bmatrix}$	0.001	$[66.93 \quad 31.69 \quad 1]$	Stable, High Precession Slippage
5	$\begin{bmatrix}5 & 0 & 0\\ 0 & 0.05 & 0\\ 0 & 0 & 0.0017\end{bmatrix}$	0.001	$[64.38 \quad 8.89 \quad 0.4082]$	Stable, Good Performance

After fine-tuning the LQR control system, several experiments are carried out to compare the results between experiment and simulation. Figure 6.4 compares the simulation and experiment for 1000 [rpm] flywheel speed. In this experiment, the control matrix is taken as $K = [64.38 \quad 8.89 \quad 0.4082]$. The disturbance gain is taken as $T_M = 1$. When Figure 6.4 is examined, it is seen that after the start of operation, the experimental and simulation results for the ship's roll angle are close to each other. However, the precession angle on the experiment is drifted than the simulation results.

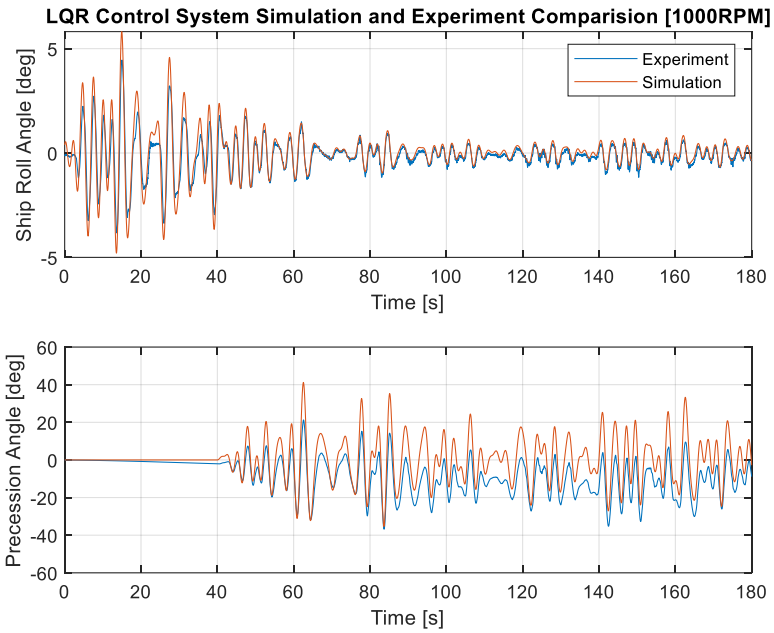

Figure 6.4. LQR control system simulation and experimental comparison at 1000 [rpm] flywheel speed ($T_M = 1$, $\dot{\theta}_3 = 1000\ [rpm]$, $K = [64.38 \quad 8.89 \quad 0.4082]$)

The Figure 6.5 shows the LQR system experiment for flywheel speed 2000 [rpm]. The control matrix is calculated as $K = [67.69 \quad 8.1 \quad 0.41]$. The disturbance gain is set to $T_M = 1.5$. The results show that the drift on the 2000 [rpm] test is not high as 1000 [rpm] test.

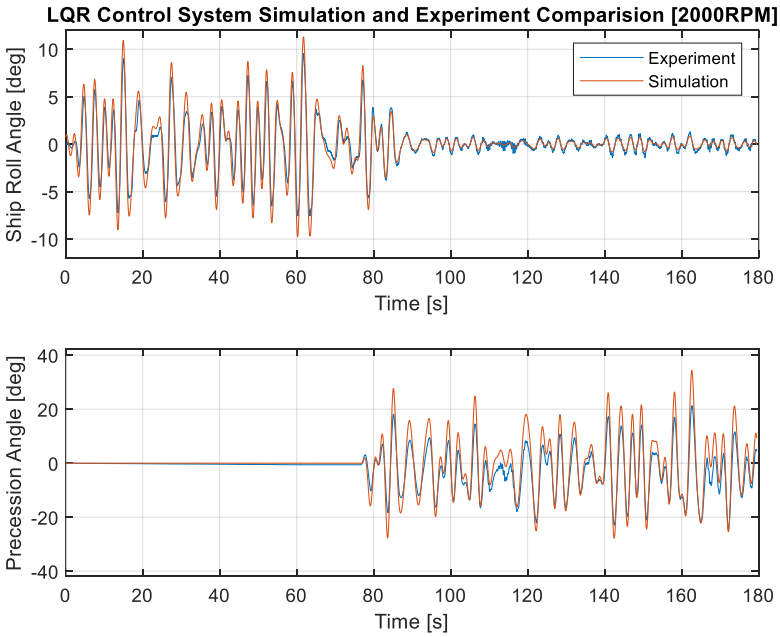

Figure 6.5. LQR control system simulation and experimental comparison at 2000 [rpm] flywheel speed ($T_M = 1.5$, $\dot{\theta}_3 = 2000\ [rpm]$, $K = [67.69 \quad 8.41 \quad 0.41]$)

Table 6.5 LQR control system experimental and simulation results comparison table for 1000 [rpm]and 2000 [rpm] tests

	$\dot{\theta}_3$	θ_1 RMS [˚]	$\lvert\theta_1\rvert$ MAX [˚]	θ_2 RMS [˚]	$\lvert\theta_2\rvert$ MAX [˚]
Operation State (70-180)	Simulation 1000 RPM	0.3497	1.0741	12.3714	35.780
Operation State (70-180)	Experimental 1000 RPM	0.3647	1.1652	14.4956	36.8374
Operation State (110-180)	Simulation 2000 RPM	0.3606	0.8656	12.5249	34.4875
Operation State (110-180)	Experimental 2000 RPM	0.5307	1.4321	10.1384	24.5009

Table 6.5 shows the root mean square (RMS) and maximum values for ship roll angle and enclosure precession angle. The simulation and experimental RMS values for ship roll angle in 1000 [rpm] are close to each other. However, the RMS results for 2000 [rpm] are very different.

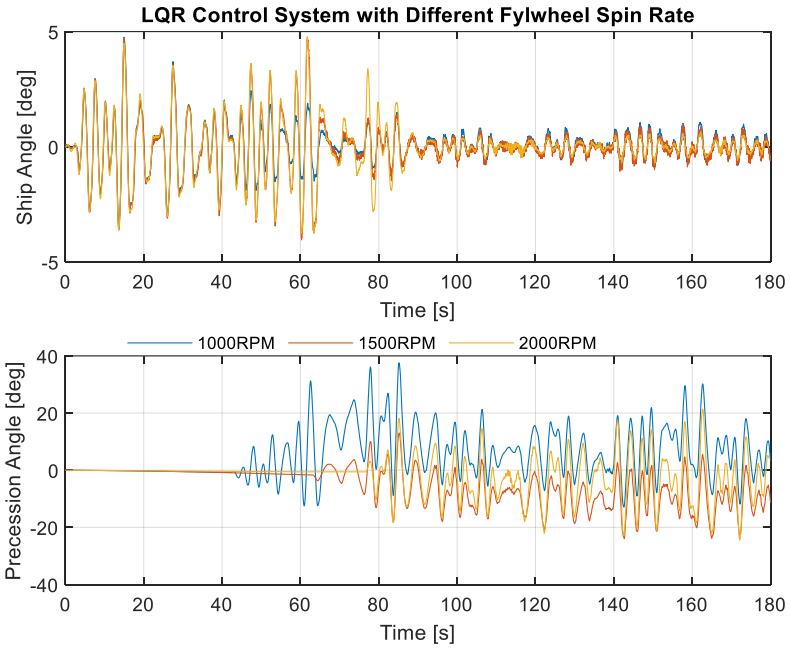

Figure 6.6. LQR control system performance results at different flywheel speeds ($T_M = 1.25$,$K_1 = [64.38 \quad 8.89 \quad 0.4082]$,$K_2 = [66.40 \quad 8.38 \quad 0.4182]$, $K_3 = [67.69 \quad 8.41 \quad 0.41]$)

Figure 6.6 shows the 1000, 1500 and 2000 [rpm] test results. Using the available data in given Figure 6.6, the Table 6.6 is created that shows the RMS and maximum values for the LQR control system at different flywheel speeds. The RMS and maximum values of the ship's roll angle show that the values are reduced by increasing the flywheel speed. Similarly for the PV-PI control system there is some drift at the 1500 [rpm] flywheel speed hence the RMS and maximum precession angle values.

Table 6.6. LQR control system performance comparison table for different flywheel speeds

	$\dot{\theta}_3$	θ_1 RMS	$\lvert\theta_1\rvert$ MAX	θ_2 RMS	$\lvert\theta_2\rvert$ MAX
Operation State (70-180)	1000 RPM	0.4474	1.4904	11.8236	37.5828
Operation State (100-180)	1500 RPM	0.3438	1.0663	11.4944	23.92
Operation State (130-180)	2000 RPM	0.2689	0.7161	11.2340	15.2504

6.3 PV-PI and LQR Control System Performance Comparison

Having compared the PV-PI and LQR control systems individually, this section is formed to compares their performance. As shown in Figure 6.7, two test results for 1000 [rpm] flywheel speed are compared. For the tests, the disturbance gain is taken as T_M, control matrix for LQR control system is $K = [64.38 \quad 8.89 \quad 0.4082]$ and control parameters for PV-PI system are $K_P = 9$, $K_V = 1$, $K_T = 5$, $K_I = 15$, $K_E = 0.1$, $K_{EI} = 1$. The figure shows that the LQR control system has a better performance than the PV-PI control system in terms of reducing the ship's roll angle. Also, when comparing the results for the precession angle, it is seen that the LQR control system is better at adjusting the working range of the precession angle.

For a fair comparison it is a good idea to examine the frequency domain signals of the undamped motion, the damped motion with PV-PI control and the LQR control. Figure 6.8 shows the FFT results of the signals. From the figure it is seen that the natural frequency of the system is around 0.4 [Hz]. The FFT signal of the LQR control system signal has a slightly lower value than that of the PV-PI control system. The area under

the curve (power) for the undamped signal is 0.3890, whereas it is 0.0427 for the PV-PI control system and 0.0389 for the LQR control system.

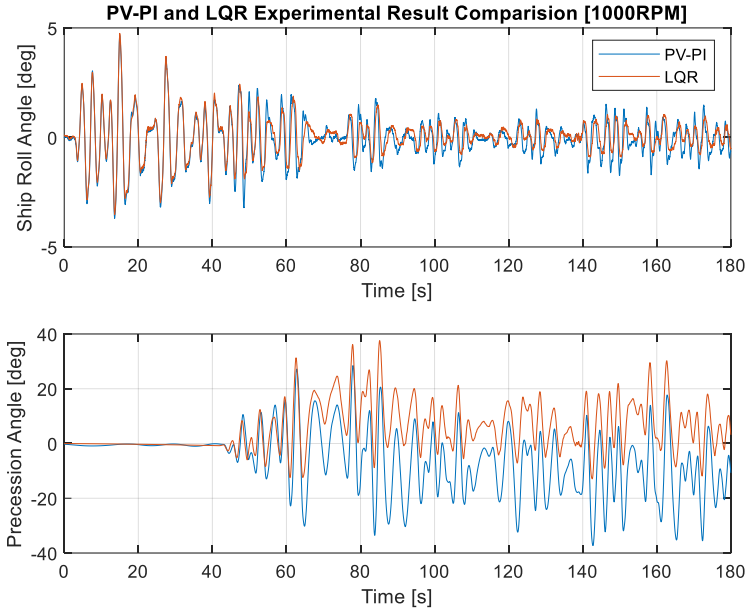

Figure 6.7. PV-PI and LQR control system performances at 1000 [rpm] flywheel speed ($T_M = 1$, $K = [64.38 \quad 8.89 \quad 0.4082]$, $K_P = 9$, $K_V = 1$, $K_T = 5$, $K_I = 15$, $K_E = 0.1$, $K_{EI} = 1$)

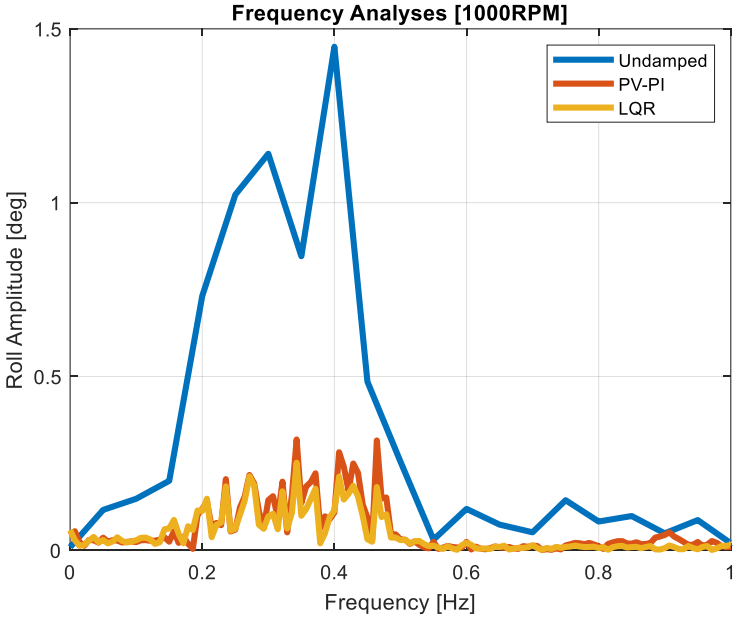

Figure 6.8. PV-PI and LQR control system frequency domain performance comparison at 1000 [rpm] flywheel speed ($T_M = 1$, $K = [64.38 \quad 8.89 \quad 0.4082]$, $K_P = 9$, $K_V = 1$, $K_T = 5$, $K_I = 15$, $K_E = 0.1$, $K_{EI} = 1$)

An additional comparison between PV-PI and LQR control systems is made for 2000 [rpm]. In these experiments the disturbance gain is taken as ($T_M = 1.5$). Examining Figure 6.9, it is seen that both PV-PI and LQR are fully operational after 110 seconds.

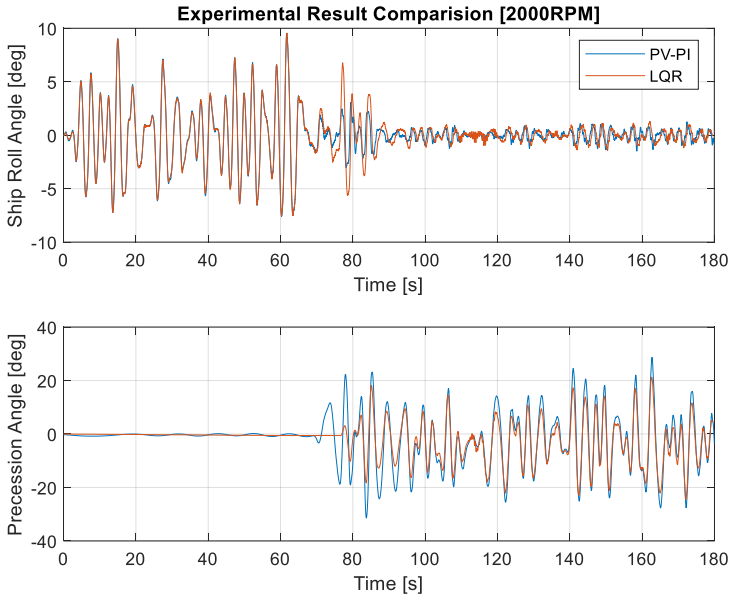

Figure 6.9. PV-PI and LQR control system performances at 2000RPM flywheel speed ($T_M = 1.5,\ K = [67.69 \quad 8.41 \quad 0.41], K_P = 9,\ K_V = 1,\ K_T = 5,\ K_I = 15,\ K_E = 0.1, K_{EI} = 1$)

The Figure 6.9 that the damped ship roll motion is close to each other both control strategies. But the Figure 6.10 investigated it is seen that PV-PI control system shows better performance than LQR control system. When the area under the frequency domain signal is examined, this difference becomes more visible. The area for the undamped roll motion is 0.4335 while the damped PV-PI control system is 0.0411 and the damped LQR control system is 0.0540.

In short, this section gives the performance results by comparing the simulation and experimental results. Experiments show that higher flywheel spin rates increase the roll damping of the ship. Also, it helps to minimize the precession motion, thus preventing the hull drift problem. When the frequency domain results are investigated, it is seen that PV-PI and LQR control system have good performance.

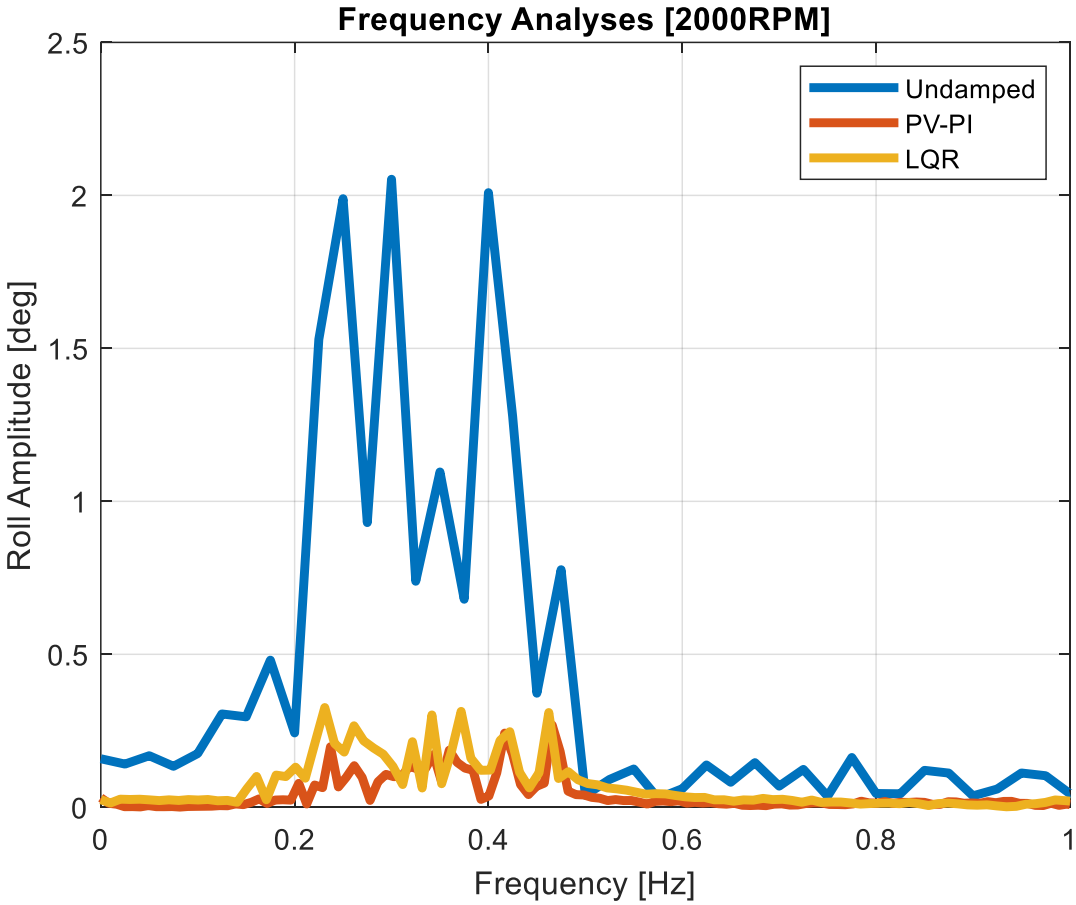

Figure 6.10. PV-PI and LQR control system frequency domain performance comparison at 2000 rpm flywheel speed ($T_M = 1.5$, $K = [67.69 \quad 8.41 \quad 0.41]$, $K_P = 9$, $K_V = 1$, $K_T = 5$, $K_I = 15$, $K_E = 0.1$, $K_{EI} = 1$)

CHAPTER 7

CONCLUSION

In this thesis, a scaled-down gyrostabilizer system is designed to investigate performance of the different gyrostabilizer control algorithms. The scaled down ship system is designed with a 1-DoF rolling motion around the metacentric axis and the other motions are constrained. A BLDC motor is attached to the metacentric axis to mimic sea disturbances around the ship's rolling direction. The kinematics and dynamics of the ship and the gyrostabilizer are studied using the Newton-Euler method. The joint reactions and dynamic equations are then compared using the Simulink simulation environment. The results show that there is only a small numerical error between the calculated and simulated joint reactions.

The main study of this thesis focuses on the control system design of the gyrostabilizer system. Two control systems are designed for this purpose. The first is the PV-PI control system from classical control theory. The PV-PI control system has upper and lower controllers that minimize both enclosure (precession) and ship motion. It has 7 control parameters including the flywheel rotation rate. This makes the tuning process of the control parameters relatively complicated. The other control system is a full state controller which uses a linear quadratic regulator (LQR) to find the optimum control parameters. It is easier to tune because there are 4 different parameters for penalty and effort matrices. Once the optimum parameters are found, it can be applied to other types of ships and gyrostabilizer systems. Before the performance tests, the system identification operations are performed. The effect neglected components of the test assembly during the formation of the theoretical model are identified by examining the input/output relationships of the axis. In this way, several transfer functions are generated for the ship's roll motion, the feedback and the actuator system. The system identification test results show that design and manufactured test rig system has differences when their transfer functions are investigated.

Following the system identification tests, the performance of the control system is investigated in three sections. Firstly, the experimental test results of the PV-PI control system are studied and compared with the simulation results. The performance variation

due to different flywheel speeds is also investigated. Secondly, the experimental test results of the LQR control system are compared with its simulation results and, similar to the PV-PI control system, several experiments are carried out for different flywheel speeds. Finally, the experimental test results obtained with the PV-PI and LQR control systems are compared for 1000 [rpm] and 2000 [rpm] flywheel speeds.

Looking at the results, the LQR system has a better performance at 1000 [rpm]. However, the PV-PI control system has a better performance at 2000 [rpm]. Therefore, it can be concluded that their damping performances are similar. However, the results show that the LQR control system has better results in adjusting the precession range than the PV-PI control system. Also, the complexity of the PV-PI control system is another disadvantage in its implementation.

Future studies should focus on the design of an adaptive control system for changing the control parameters for changing sea states. The designed control system gives good performance for the given disturbance signal and lower sea states. However, as the disturbance signal increases due to the sea state, it violates the boundary conditions related to the enclosure motion and the system starts to oscillate. An adaptive controller can be implemented to solve this problem.

REFERENCES

Bergdahl, Lars. *Wave-induced loads and ship motions*. Göteborg: Chalmers University of Technology, 2009.

"Boat Gyro Stabilization System." Allied Motion. Last modified October 4, 2021. https://www.alliedmotion.com/applications/commercial-consumer/boat-gyro-stabilization-system/.

Burger, W., and A. G. Corbet. "Anti-Rolling Devices in General." In *Ship Stabilizers*, 31–37. 1966. https://doi.org/10.1016/b978-0-08-011504-7.50009-5.

Cha, Yoon-Hee, John F. Golding, Behrang Keshavarz, Joseph Furman, Ji-Soo Kim, Jose A. Lopez-Escamez, Måns Magnusson, Bill J. Yates, and Ben D. Lawson. "Motion Sickness Diagnostic Criteria: Consensus Document of the Classification Committee of the Bárány Society." *Journal of Vestibular Research* 31, no. 5 (October 4, 2021): 327–44. https://doi.org/10.3233/ves-200005.

Chakraborty, Soumya. "Ship Stability - Understanding Curves of Static Stability." *Marine Insight*. Last modified February 14, 2022. https://www.marineinsight.com/naval-architecture/ship-stability-understanding-curves-static-stability/.

DiFrangia, Michelle. "Electrohydraulic Controls Improve Ship Stability." *Fluid Power World*. Last modified May 11, 2016. https://www.fluidpowerworld.com/electrohydraulic-controls-improve-ship-stability/.

Dorf, Richard C., and Robert H. Bishop. *Modern Control Systems*. 13th ed. PEARSON, 2018. Chapter 11, "The Design of State Variable Feedback Systems."

Euston, Matthew, Paul Coote, Robert Mahony, Jonghyuk Kim, and Tarek Hamel. "A Complementary Filter for Attitude Estimation of a Fixed-Wing UAV." In *2008 IEEE/RSJ International Conference on Intelligent Robots and Systems*, September 2008. https://doi.org/10.1109/iros.2008.4650766.

Fan, Wang, Jin Hongzhang, and Qi Zhigang. "Modeling for Active Fin Stabilizers at Zero Speed." *Ocean Engineering* 36, no. 17–18 (December 2009): 1425–37. https://doi.org/10.1016/j.oceaneng.2009.07.013.

"Final Report and Recommendations to the 23rd ITTC." In *Proceedings of the 23rd ITTC*, 554–59, 2002. https://doi.org/10.1007/978-981-10-6946-8_300396.

Giallanza, Antonio, and Tony Elms. "Interactive Roll Stabilization Comparative Analysis for Large Yacht: Gyroscope Versus Active Fins." International Journal on Interactive Design and Manufacturing (IJIDeM) 14, no. 1 (November 12, 2019): 143–51. https://doi.org/10.1007/s12008-019-00618-y.

"How Gyrostabilizers Work." Accessed March 18, 2024. https://veemmarine.com/wp-content/uploads/2021/08/Whitepaper-1402-How_Gyrostabilizers_Work-comments.pdf.

Ibrahim, R. A., and I. M. Grace. "Modeling of Ship Roll Dynamics and Its Coupling with Heave and Pitch." Mathematical Problems in Engineering 2010 (2010): 1–32. https://doi.org/10.1155/2010/934714.

Kornev, N. Ship Dynamics in Waves: Ship Theory 2, 2nd ed. Rostock, 2012. [Online]. Available: https://www.scribd.com/document/129610211/Ship-Dynamics-in-Waves.

Kula, K.S. "An Overview of Roll Stabilizers and Systems for Their Control." TransNav, the International Journal on Marine Navigation and Safety of Sea Transportation 9, no. 3 (2015): 405–14. https://doi.org/10.12716/1001.09.03.14.

Liu, Jinsong, Edwin Thomas, Lance Manuel, D. Griffith, Kelley Ruehl, and Matthew Barone. "Integrated System Design for a Large Wind Turbine Supported on a Moored Semi-Submersible Platform." Journal of Marine Science and Engineering 6, no. 1 (January 12, 2018): 9. https://doi.org/10.3390/jmse6010009.

Molland, Anthony F. The Maritime Engineering Reference Book: A Guide to Ship Design, Construction and Operation. Amsterdam and others: Elsevier/Butterworth-Heinemann, 2011.

O'Hanlon, James F., and Michael E. McCauley. "Motion Sickness Incidence as a Function of the Frequency and Acceleration of Vertical Sinusoidal Motion." September 1, 1973. https://doi.org/10.21236/ad0768215.

Olmez, Alper, and Ferdi Cakici. "Theoretical Manual of 'Ytu Deep' Ship Motion Program." Ocean Engineering 266 (December 2022): 112451. https://doi.org/10.1016/j.oceaneng.2022.112451.

Perez, Tristan, and Mogens Blanke. "Ship Roll Damping Control." Annual Reviews in Control 36, no. 1 (April 2012): 129–47. https://doi.org/10.1016/j.arcontrol.2012.03.010.

Perez, Tristan, and Paul D. Steinmann. "Analysis of Ship Roll Gyrostabiliser Control." IFAC Proceedings Volumes 42, no. 18 (2009): 310–15. https://doi.org/10.3182/20090916-3-br-3001.0007.

Ryabkova, M., V. Karaev, J. Guo, and Yu. Titchenko. "A Review of Wave Spectrum Models as Applied to the Problem of Radar Probing of the Sea Surface." Journal of Geophysical Research: Oceans 124, no. 10 (October 2019): 7104–34. https://doi.org/10.1029/2018jc014804.

Sinha, Tanumoy. "Different Types of Roll Stabilization Systems Used for Ships." Marine Insight. Last modified April 17, 2022. https://www.marineinsight.com/naval-architecture/roll-stabilization-systems/.

Taylan, Metin. "The Effect of Nonlinear Damping and Restoring in Ship Rolling." Ocean Engineering 27, no. 9 (April 2000): 921–32. https://doi.org/10.1016/s0029-8018(99)00026-8.

Toffoli, Alessandro, and Elzbieta M. Bitner-Gregersen. "Types of Ocean Surface Waves, Wave Classification." In Encyclopedia of Maritime and Offshore Engineering, March 6, 2017, 1–8. https://doi.org/10.1002/9781118476406.emoe077.

Townsend, Nicholas C., and R. Ajit Shenoi. "Control Strategies for Marine Gyrostabilizers." IEEE Journal of Oceanic Engineering 39, no. 2 (April 2014): 243–55. https://doi.org/10.1109/joe.2013.2254591.

Townsend, Nicholas C., and Ramanand A. Shenoi. "Gyrostabilizer Vehicular Technology." Applied Mechanics Reviews 64, no. 1 (January 1, 2011). https://doi.org/10.1115/1.4004837.

Williams, John Page. "Engineering Boats for Seakeepers: Boating Mag." Boating Magazine. Last modified May 6, 2023. https://www.boatingmag.com/boats/engineering-for-seakeepers/.

APPENDIX A

TEST SYSTEM SPECIFICATIONS

Table A.1. Motor specification parameters

	Enclosure	**Flywheel**	**Wave**	
Motor Parameter	**RE30**	**EC45**	**EC90**	**Unit**
Terminal Resistance	0.196	0.7	0.514	Ohm
Terminal Inductance	0.0000344	0.000463	0.000544	H
Rotor Inertia	33.9 (10^{-7})	240 (10^{-7})	317 (10^{-6})	kgm^2
Back-emf constant	0.0135	0.037	0.11	V/[rad/s]
Torque Constant	0.0103	0.0369	0.11	Nm/A
Mechanical Time Constant	3.64	12.3	13.5	ms
Gearbox Inertia	0.7 (10^{-7})			kgm^2
Gearbox Ratio	159:1		8:1	#

Table A.2. Data log computer specifications

HP Pavilion Notebook	
Processor	Intel(R) Core(TM) i7-7500U CPU
Memory	8 GB
Graphics Card	4 GB

Table A.3. Data acquisition card specifications

V-DAQ Real Time Control & Data Acquisition Card	
Encoder Inputs	
Number of Channel	2
Counter Size	32 bits
Maximum Counter Frequency	1 MHz
Digital Inputs	
Number of Channel	8
Leakage Current	±2μA
Analog Inputs	
Number of Channel	4 Single Ended | 2 Differential
Resolution	16 bits
Distortion	91 dB
Offset Error	±2mV
Analog Outputs	
Number of Channel	4
Resolution	16 bits
Offset Error	±6mV
DC Output Impedance	0.5Ω
Capacitive Load Stability	4000pF
Maximum Load	2kΩ
Output Noise	80μV RMS (@100kHz)

APPENDIX B

EQUATIONS

Table B.3. Kinematic equations

Transformation Matrices
$$\hat{C}^{(0,1)} = \begin{bmatrix} \cos(\theta_1) & -\sin(\theta_1) & 0 \\ \sin(\theta_1) & \cos(\theta_1) & 0 \\ 0 & 0 & 1 \end{bmatrix}$$
$$\hat{C}^{(1,2)} = \begin{bmatrix} 1 & 0 & 0 \\ 0 & \cos\left(-\frac{\pi}{2}\right) & -\sin\left(-\frac{\pi}{2}\right) \\ 0 & \sin\left(-\frac{\pi}{2}\right) & \cos\left(-\frac{\pi}{2}\right) \end{bmatrix} \begin{bmatrix} \cos(\theta_2) & -\sin(\theta_2) & 0 \\ \sin(\theta_2) & \cos(\theta_2) & 0 \\ 0 & 0 & 1 \end{bmatrix}$$
$$\hat{C}^{(2,3)} = \begin{bmatrix} \cos\left(-\frac{\pi}{2}\right) & 0 & \sin\left(-\frac{\pi}{2}\right) \\ 0 & 1 & 0 \\ -\sin\left(-\frac{\pi}{2}\right) & 0 & \cos\left(-\frac{\pi}{2}\right) \end{bmatrix} \begin{bmatrix} \cos(\theta_2) & -\sin(\theta_2) & 0 \\ \sin(\theta_2) & \cos(\theta_2) & 0 \\ 0 & 0 & 1 \end{bmatrix}$$
Position Level Kinematic Analyses
$$\bar{r}_{O_0G_1}^{(0)} = g_{11}\hat{C}^{(0,1)}\bar{u}_1 + g_{12}\hat{C}^{(0,1)}\bar{u}_2 + g_{13}\hat{C}^{(0,1)}\bar{u}_3$$
$$\bar{r}_{O_0O_2}^{(0)} = r_{11}\hat{C}^{(0,1)}\bar{u}_1 + r_{12}\hat{C}^{(0,1)}\bar{u}_2 + r_{13}\hat{C}^{(0,1)}\bar{u}_3$$
$$\vec{r}_{O_0G_2} = \vec{r}_{O_0O_2} + \vec{r}_{O_2G_2}$$
$$\bar{r}_{O_2G_2}^{(0)} = g_{21}\hat{C}^{(0,2)}\bar{u}_1 + g_{22}\hat{C}^{(0,2)}\bar{u}_2 + g_{23}\hat{C}^{(0,2)}\bar{u}_3$$
$$\vec{r}_{O_0O_3} = \vec{r}_{O_0O_2} + \vec{r}_{O_2O_3}$$
$$\bar{r}_{O_2G_2}^{(0)} = r_{21}\hat{C}^{(0,2)}\bar{u}_1 + r_{22}\hat{C}^{(0,2)}\bar{u}_2 + r_{23}\hat{C}^{(0,2)}\bar{u}_3$$
$$\vec{r}_{O_0G_3} = \vec{r}_{O_0O_3} + \vec{r}_{O_3G_3}$$
$$\bar{r}_{O_3G_3}^{(0)} = g_{31}\hat{C}^{(0,3)}\bar{u}_1 + g_{32}\hat{C}^{(0,3)}\bar{u}_2 + g_{33}\hat{C}^{(0,3)}\bar{u}_3$$
Velocity Level Kinematic Analyses
$$\vec{\omega}_{1/0} = \dot{\theta}_1\vec{u}_3^{(0)}$$
$$\vec{\omega}_{2/0} = \vec{\omega}_{1/0} + \vec{\omega}_{2/1} = \dot{\theta}_1\vec{u}_3^{(0)} + \dot{\theta}_2\vec{u}_2^{(1)}$$
$$\vec{\omega}_{2/0}^{(0)} = \dot{\theta}_1\vec{u}_3^{\left(\frac{0}{0}\right)} + \dot{\theta}_2\hat{C}^{(0,1)}\vec{u}_2^{\left(\frac{1}{1}\right)}$$

(cont. on next page)

Table B.1. (cont)

$\bar{\omega}_{2/1}^{(0)} = -\dot{\theta}_2 \sin(\theta_1)\, \bar{u}_1 + \dot{\theta}_2 \cos(\theta_1)\, \bar{u}_2$
$\vec{\omega}_{3/0} = \vec{\omega}_{3/2} + \vec{\omega}_{2/0} = \dot{\theta}_1 \vec{u}_3^{(0)} + \dot{\theta}_2 \vec{u}_2^{(1)} - \dot{\theta}_3 \vec{u}_1^{(2)}$ $\vec{\omega}_{3/0} = \vec{\omega}_{3/2} + \vec{\omega}_{2/0} = \dot{\theta}_1 \vec{u}_3^{\binom{0}{0}} + \dot{\theta}_2 \hat{C}^{(0,1)} \vec{u}_2^{\binom{1}{1}} - \dot{\theta}_3 \hat{C}^{(0,2)} \vec{u}_1^{\binom{2}{2}}$ $\vec{\omega}_{3/2} = -\dot{\theta}_3 \cos(\theta_1) \cos(\theta_2)\, \bar{u}_1 - \dot{\theta}_3 \cos(\theta_2) \sin(\theta_1)\, \bar{u}_2 + \dot{\theta}_3 \sin(\theta_2)\, \bar{u}_3$
$\vec{V}_{G_1/O_0}^{(d0)} = \vec{\omega}_{1/0} \times \vec{r}_{O_0 G_1}$
$\vec{V}_{O_2/O_0}^{(d0)} = \vec{\omega}_{1/0} \times \vec{r}_{O_0 O_2}$
$\vec{V}_{G_2/O_0}^{(d0)} = \vec{\omega}_{2/0} \times \vec{r}_{O_0 G_2} + \vec{V}_{O_2/O_0}^{(d0)}$
$\vec{V}_{O_3/O_0}^{(d0)} = \vec{\omega}_{2/0} \times \vec{r}_{O_2 O_3} + \vec{V}_{O_2/O_0}^{(d0)}$
$\vec{V}_{G_3/O_0}^{(d0)} = \vec{\omega}_{3/0} \times \vec{r}_{O_3 G_3} + \vec{V}_{O_3/O_0}^{(d0)}$
Acceleration Level Kinematic Analyses
$\vec{\alpha}_{1/0} = \ddot{\theta}_1 \vec{u}_3^{(0)}$
$\vec{\alpha}_{2/0} = \vec{\alpha}_{1/0} + \vec{\alpha}_{2/1} + \vec{\omega}_{1/0} \times \vec{\omega}_{2/1} = \ddot{\theta}_1 \vec{u}_3^{(0)} + \ddot{\theta}_2 \vec{u}_2^{(1)} + \dot{\theta}_1 \vec{u}_3^{(0)} \times \dot{\theta}_2 \vec{u}_2^{(1)}$
$\vec{\alpha}_{3/0} = \vec{\alpha}_{1/0} + \vec{\alpha}_{2/1} + \vec{\alpha}_{3/2} + \vec{\omega}_{1/0} \times \vec{\omega}_{2/1} + \vec{\omega}_{2/0} \times \vec{\omega}_{3/2}$ $= \vec{\alpha}_{2/0}^{(0)} - \ddot{\theta}_3 \vec{u}_1^{(2)} + \vec{\omega}_{2/0} \times \vec{\omega}_{3/2}$
$\vec{a}_{G_1/O_0}^{(do)} = \vec{\alpha}_{1/0} \times \vec{r}_{O_0 G_1} + \vec{\omega}_{1/0} \times \left(\vec{\omega}_{1/0} \times \vec{r}_{O_0 G_1}\right) + \vec{a}_{O_1/O_0}^{(do)}$
$\vec{a}_{O_2/O_0}^{(do)} = \vec{\alpha}_{1/0} \times \vec{r}_{O_0 O_2} + \vec{\omega}_{1/0} \times \left(\vec{\omega}_{1/0} \times \vec{r}_{O_0 O_2}\right) + \vec{a}_{O_1/O_0}^{(do)}$
$\vec{a}_{G_2/O_0}^{(do)} = \vec{\alpha}_{2/0} \times \vec{r}_{O_2 G_2} + \vec{\omega}_{2/0} \times \left(\vec{\omega}_{2/0} \times \vec{r}_{O_2 G_2}\right) + \vec{a}_{O_2/O_0}^{(do)}$
$\vec{a}_{O_3/O_0}^{(do)} = \vec{\alpha}_{2/0} \times \vec{r}_{O_2 O_3} + \vec{\omega}_{2/0} \times \left(\vec{\omega}_{2/0} \times \vec{r}_{O_2 O_3}\right) + \vec{a}_{O_2/O_0}^{(do)}$
$\vec{a}_{G_3/O_0}^{(do)} = \vec{\alpha}_{3/0} \times \vec{r}_{O_3 G_2} + \vec{\omega}_{3/0} \times \left(\vec{\omega}_{3/0} \times \vec{r}_{O_3 G_3}\right) + \vec{a}_{O_3/O_0}^{(do)}$

Table B.4. Dynamic Equations

Force Analyses
$$m_3\vec{a}_3 = \vec{F}_{23} + m_3\vec{g}$$ $$\bar{F}_{23}^{(2)} = m_3\hat{C}^{(2,0)}\left(\bar{a}_3^{(0)} - \bar{g}^{(0)}\right)$$
$$m_2\vec{a}_2 = \vec{F}_{32} + \vec{F}_{12} + m_2\vec{g}$$ $$\bar{F}_{12}^{(1)} = \hat{C}^{(1,2)}\bar{F}_{23}^{(2)} - m_2\hat{C}^{(1,0)}\left(\bar{a}_2^{(0)} - \bar{g}^{(0)}\right)$$
$$m_1\vec{a}_1 = \vec{F}_{01} + \vec{F}_{21} + m_1\vec{g}$$ $$\bar{F}_{01}^{(0)} = \hat{C}^{(0,1)}\bar{F}_{12}^{(1)} - m_1\left(\bar{a}_1^{(0)} - \bar{g}^{(0)}\right)$$
Moment Analyses
$$\vec{M}_{23} = \check{J}_3 \cdot \vec{\alpha}_3 + \vec{\omega}_3 \times \check{J}_3 \cdot \vec{\omega}_3 + \vec{r}_{O_3G_3} \times \vec{F}_{23}$$
$$\vec{M}_{12} = \vec{M}_{23} + \check{J}_2 \cdot \vec{\alpha}_2 + \vec{\omega}_2 \times \check{J}_2 \cdot \vec{\omega}_2 + \vec{r}_{O_2G_2} \times \vec{F}_{12} + \left(\vec{r}_{O_2O_3} - \vec{r}_{O_3G_2}\right) \times \vec{F}_{23}$$
$$\vec{M}_{01} = \vec{M}_{12} + \check{J}_1 \cdot \vec{\alpha}_1 + \vec{\omega}_1 \times \check{J}_1 \cdot \vec{\omega}_1 + \vec{r}_{O_0G_1} \times \vec{F}_{01} + \left(\vec{r}_{O_0O_2} - \vec{r}_{O_3G_3}\right) \times \vec{F}_{12}$$

APPENDIX C

TEST RIG DIMENSIONS

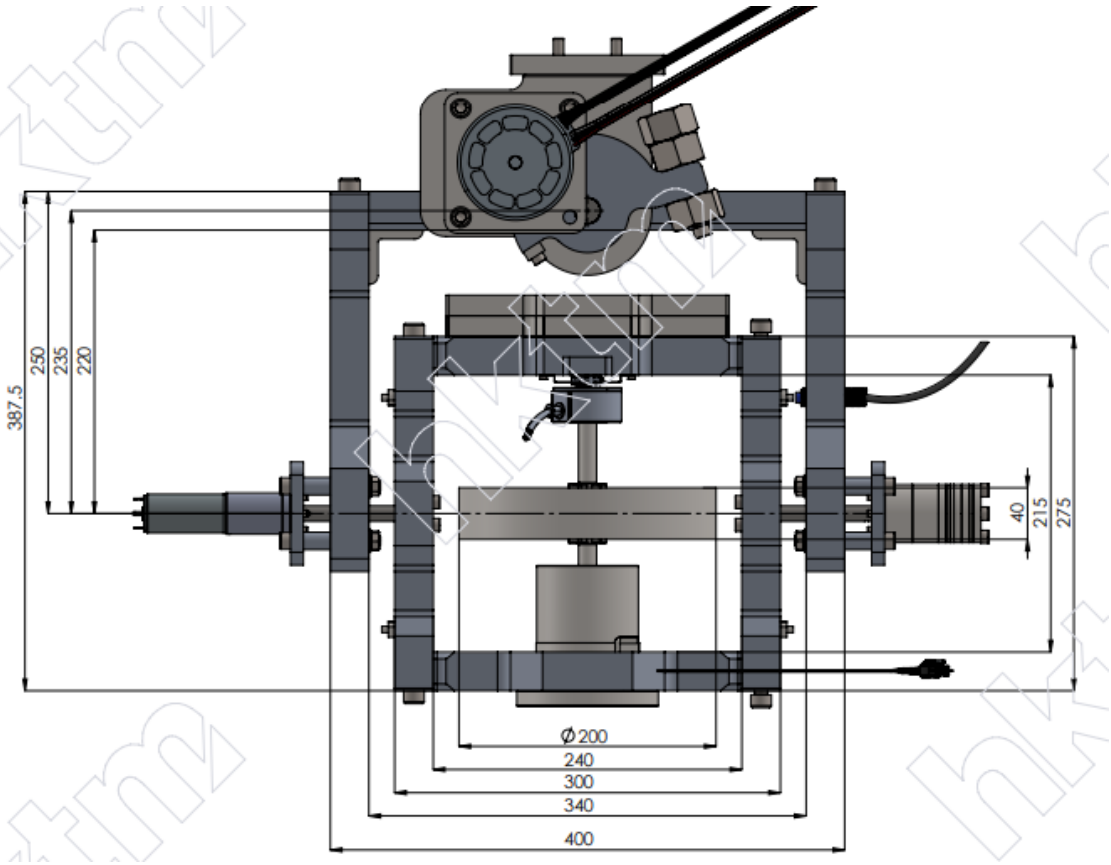

Figure C.1 Dimensions of the test rig